Tuning apico-basal polarity and junctional recycling in the hemogenic endothelium orchestrates pre-hematopoietic stem cell emergence complexity

Léa Torcq, Sara Majello, Catherine Vivier, Anne Schmidt

Tuning apico-basal polarity and junctional recycling in the hemogenic endothelium orchestrates pre-hematopoietic stem cell emergence complexity

Léa Torcq,[1,2] Sara Majello,[1] Catherine Vivier,[1] and Anne A. Schmidt [1,6,*]

[1] Institut Pasteur, Université Paris Cité, CNRS UMR3738, Department of Developmental and Stem Cell Biology, F-75015 Paris, France

[2] Sorbonne Université, Collège doctoral, F-75005 Paris, France

[6] Lead contact

* Correspondence: anne.schmidt@pasteur.fr

Abstract

Hematopoietic stem cells emerge in the embryo from an aortic-derived tissue called the hemogenic endothelium (HE). The HE appears to give birth to cells of different nature and fate but the molecular principles underlying this complexity are largely unknown. Here we show, in the zebrafish embryo, that two cell types emerge from the aortic floor with radically different morphodynamics. With the support of live imaging, we bring evidence suggesting that the mechanics underlying the two emergence types rely, or not, on apicobasal polarity establishment. While the first type is characterized by reinforcement of apicobasal polarity and maintenance of the apical/luminal membrane until release, the second type emerges via a dynamic process reminiscent of trans-endothelial migration. Interfering with Runx1 function suggests that the balance between the two emergence types depends on tuning apicobasal polarity at the level of the HE. In addition, using new transgenic fish lines that express Junctional Adhesion Molecules and functional interference, we bring evidence for the essential role of ArhGEF11/PDZ-RhoGEF in controlling the HE-endothelial cell dynamic interface, including cell-cell intercalation, which is ultimately required for emergence completion. Overall, we highlight critical cellular and dynamic events of the endothelial-to-hematopoietic transition that support emergence complexity, with a potential impact on cell fate.

Major subject areas: Developmental Biology and Stem cells, Cell Biology.

Keywords: hematopoiesis, stem cell, cell extrusion, endothelial-to-hematopoietic transition, apico-basal polarity, hemogenic endothelium, tight junctions, JAMs, zebrafish.

Introduction

Hematopoietic stem cells (HSCs) endowed with full regenerative potential in adult vertebrates are generated during a narrow-time window of few days during embryonic development. These cells, at the root of all blood and immune cells in the body, emerge from intra-embryonic aortic vessels and, more specifically, from a specialized type of vascular tissue called the hemogenic endothelium (HE, (Wu and Hirschi 2021)). A series of seminal studies have evidenced the autonomous production of repopulating HSCs within an intraembryonic region called the Aorta-Gonad-Mesonephros (AGM), before their appearance in other hematopoietic organs (A. L. Medvinsky et al. 1993; Müller et al. 1994; Garcia-Porrero, Godin, and Dieterlen-Lièvre 1995; A. Medvinsky and Dzierzak 1996; Cumano, Dieterlen-Lievre, and Godin 1996). Thereafter, the endothelial origin of HSCs was evidenced (Jaffredo et al. 1998; de Bruijn et al. 2002; T. E. North et al. 2002). The direct visualization, in real-time, of the emergence of precursors of hematopoietic stem and progenitor cells (HSPCs) from the dorsal aorta, termed the Endothelial-to-Hematopoietic Transition (EHT), was finally achieved *in vitro* (Eilken, Nishikawa, and Schroeder 2009), *ex-vivo* from mouse sections (Boisset et al. 2010), and *in vivo* in the zebrafish embryo (Bertrand et al. 2010; Kissa and Herbomel 2010), using live microscopy. This opened the way to a more detailed analysis of the characteristics of the HE at the transcriptional level, revealing its transient nature and its early hematopoietic commitment (Swiers et al. 2013).

The HE is characterized by inherent heterogeneity and is not only contributing to the formation of precursors to long-term HSCs (pre-HSCs) but also to more restricted progenitors (Hadland and Yoshimoto 2018). These progenitors can be born from HE sub-types that are found in extra-embryonic source such as the yolk-sac – in which case it gives rise to erythro-myeloid progenitors that will sustain erythro-myelopoiesis until birth (Frame et al. 2016) -, or both from extra and intra-embryonic sources (the yolk sac and the dorsal aorta) in which cases

progenitors are biased, such as for example in the mouse, toward T- and B- innate-type lymphoid progenitors (Yoshimoto et al. 2011; 2012) or toward less restricted, multipotent progenitors (Hadland and Yoshimoto 2018; Dignum et al. 2021). Importantly, while some of the non-HSC derived progenitors born during embryonic life only support the functions of the immune system during embryonic/ fetal life, others can persist in the adult to exert tissue-resident functions, as has been mainly described in the mouse (Ghosn et al. 2019). However, studies in human embryos support the idea that developmental hematopoiesis is highly similar in mice and humans (Ivanovs et al. 2011; 2017).

A key question regarding the issue of the capacity of the HE to give birth to cells endowed with different hematopoietic potential is whether this comes from HE cells of distinct origin (in which case the HE would be a mosaic of precursors with distinct potential) or if this results from extrinsic environmental cues that impose variability in the constantly evolving developmental context (for a discussion, see (Barone et al. 2022)).

To address this type of question, high-resolution experimental settings need to be developed, if possible at the single-cell resolution. Along this line, recent developments of transcriptomics, including single cell RNAseq, spatially resolved in situ transcriptomic approaches, and in situ barcoding, have been invaluable (Weijts, Yvernogeau, and Robin 2021). Among those high-resolution approaches, cell fate mapping and lineage tracing approaches that include imaging technologies have been very instrumental, particularly when performed with the zebrafish model that reproduces many aspects of developmental hematopoiesis in higher vertebrates (Orkin and Zon 2008). Recently, work performed in the zebrafish embryo has brought evidence for heterogeneity of hematopoietic stem cell precursors being born from the HE, in the ventral floor of the dorsal aorta and independently from HSCs, including a wave of transient T-lymphocytes (using temporally-spatially resolved fate-mapping, (Tian et al. 2017)) and lympho-myeloid biased progenitors born from a myeloid-lymphoid biased Spi2+ HE that appears to co-exist with an erythroid-biased HE (using single-cell RNA-sequencing, (Xia et al. 2023)).

While light starts to be shed on the molecular and signaling cues that appear to regulate HE sub-specification and a continuum from arterial endothelium, HE maturation, and subsequent heterogeneity in HSPCs (Zhu et al. 2020), the essential molecular and cell biological properties that support HE functional plasticity remain to be determined.

Here, using the zebrafish embryo as a model, we complement our previous work describing essential molecular and mechanistic features of EHT cell emergence (Lancino et al. 2018). With the support of high-resolution live imaging and image analysis, the generation of new transgenic fish lines that express functional markers of cell polarity (podocalyxin) and of inter-cellular adhesion (Junctional Adhesion Molecules - JAMs), as well as functional and genetic interference, we bring insight into additional key features of the EHT process that take their root in the differentiation and maturation of the HE.

Results

Apicobasal polarity determines emergence types

Our previous work describing the morphodynamic evolution of cells emerging from the aortic floor through the EHT (hereafter designated as “EHT cells”), in the zebrafish embryo, revealed the unusual feature of a cell extruding from the plane of a tissue while maintaining its luminal/apical membrane until the very end of the release process, thus contributing to its peculiar crescent-shaped morphology (Kissa and Herbomel 2010; Lancino et al. 2018, and see the cartoons in ***Figure 1A***). However, to our knowledge, the polarity status of EHT cells has not been investigated so far and the maintenance of a *bona fide* apical domain has never been proven (with the luminal membrane enriched in apically targeted proteins and physically delimited by apical polarity factors and tight junction complexes (Rodriguez-Boulan, Müsch, and Le Bivic 2004; Buckley and St Johnston 2022)). Importantly, the fate of this apical-luminal membrane, after the release, may lead to cells potentially endowed with specific functional features. For example, this membrane surface may be directly and fully exposed to the extracellular space or released in the cytoplasm of EHT cells for recycling and/or degradation, after emergence completion (for examples of different scenarios, see ***Figure 1A***). Overall, this could lead to precursors of hematopoietic stem cells that, ultimately, may be differentially fated.

To address the polarity status of EHT cells, we raised transgenic fish lines that express endogenous Podocalyxin (Podxl2, (Herwig et al. 2011)), a sialomucin of the CD34 family (Nielsen and McNagny 2008). Podocalyxin was shown to take part in the formation of the preapical domain during polarization and in the regulation of its oriented organization, in tissue culture (Meder et al. 2005; Bryant et al. 2014). Its contribution to lumenization *in vivo*, in the mouse aorta, has been described and it involves negative charge repulsion induced by their glycosyl residues (Strilić et al. 2009; 2010).

We first attempted to express transiently, in the vascular system, the full-length Podxl2 zebrafish protein fused to eGFP at its extreme N-terminus. We failed to detect the fusion protein at any time point relevant for observing easily the EHT process (a time window ranging from 48 to 60 hpf (hours post-fertilization)); therefore we designed a N-ter truncated form deleted of the mucin domain and that retains amino-acids 341-587 fused to eGFP at its N-terminus (***Figure 1B*** *and see* ***Materials and Methods***). Transient transgenesis revealed that this truncated version is detected and is targeted to the luminal membranes of EHT cells. We then raised 2 transgenic (*Tg*) fish lines that express the N-ter truncated form of Podxl2 fused to either eGFP (thereafter abbreviated eGFP-Podxl2) and under the control of the Kdrl:Gal4 driver (*Tg(Kdrl:Gal4;UAS:RFP; 4xNR:eGFP-Podxl2)*), or to mKate2 and under the control of the Kdrl promoter (*Tg(Kdrl:mKate2-Podxl2))*. We observed that eGFP-Podxl2 is enriched at the luminal side of crescent-shaped EHT undergoing cells (see ***Figure 1C, Figure 1 - figure supplement 1A*** and ***Figure 1 – video 1*** (z-stack at t=0) and their legends for the details of the luminal/apical membrane evolution through time). Thereafter, these cells will be referred to as EHT pol+ cells.

We also followed the cell after emergence and observed the evolution of the luminal/apical membrane appearing as internal pseudo-vacuoles. We illustrate the reduction of their volume via membrane retrieval and, ultimately, their remanence as an intracellular membrane compartment which we define as a post-EHT signature (***Figure 1- figure supplement 1A*** and ***Figure 1- video 2*** (z-stack at t=80 min)); we propose a model for the intracellular evolution of the luminal/apical membrane which, unfortunately, cannot be traced after 2-3 hrs post-emergence because of the apparent short half-life of eGFP-Podxl2 and of the drop in activity of the Kdrl promoter (***Figure 1- figure supplement 1B***). Of notice, the pseudo-vacuoles are reminiscent of the cystic formations observed in EHT cells in the mouse and visualized by electron-microscopy (T. North et al. 1999; Marshall and Thrasher 2001) and also of the vacuolar structures recently described in EHT cells in avian embryos (Sato et al. 2023); in both cases, these vacuoles appear to emanate from the abluminal membrane (facing the sub-aortic

space) and not from the lumen. In the latter case, they disappear before EHT completion, suggesting that they contribute to exert mechanical force to initiate the detachment of the cell from the endothelial layer. In addition, their dynamics appears to depend on the activity of aquaporins and it is very possible that aquaporins are active in zebrafish too, although rather in EHT cells late in their emergence and/or in post-EHT cells, for water chase and vacuolar regression as proposed in our model (***Figure 1 – figure supplement 1B***).

While imaging the EHT using the Podxl2 expressing lines that clearly delimitate the luminal membrane, we unambiguously identified a second type of emergence. This second cell type is primarily characterized by a round-to-ovoid morphology (cells never bend as crescent-shaped EHT pol+ cells, see ***Figure 1D*** and ***Figure 1 – video 3*** for a time-lapse sequence). Importantly, these cells do not show any enrichment of eGFP-Podxl2 at the luminal membrane and will be referred to as EHT pol- cells. EHT pol- cells were observed in all other *Tg* fish lines that we are routinely imaging, including the *Tg(Kdrl:Gal4;UAS:RFP)* parental line that was used for transgenesis, thus excluding the possibility that these cells result from an artefact due to the expression of a deleted form of Podxl2 and/or to its overexpression.

Finally, we have estimated that the ratio between EHT pol+ and EHT pol- cells is of approximately 2/1, irrespective of the imaging time window and of the localization of emergence along the aortic antero-posterior axis (starting from the most anterior part of the AGM (at the limit between the balled and the elongated yolk) down to the caudal part of the aorta facing the CHT). We observed that both EHT pol+ and EHT pol- cells divide during the emergence and remain with their respective morphological characteristics after completing abscission (hence appearing as pairs of cells that exit the aortic wall sequentially, as shown ***Figure 1C, D***). We also observed that both EHT pol+ and EHT pol- cells express reporters driven by the hematopoietic marker CD41 (data not shown), which indicates that they are both endowed with hematopoietic potential.

Altogether, our results show that hemogenic cells emerging from the aortic floor do so with heterogeneity in their morphodynamic characteristics. This suggests that this may be one of the sources underlying the complexity of pre-hematopoietic stem cell identity and of their downstream cell fate.

The immature HE is not polarized

EHT pol+ and EHT pol- cells appear to emerge from the hemogenic endothelium (HE), the latter constituting the virtually exclusive cell population of the aortic floor just prior to the initiation of the EHT time-window (around 28 hpf, see (Zhao et al. 2022)). In this context, we addressed the polarity status of HE cells. Surprisingly, confocal microscopy using the *eGFP-Podxl2* expressing fish line revealed that HE cells do not appear to be polarized, based on the absence of eGFP-Podxl2 enrichment at luminal membranes, at the initiation of the EHT time-window (at approximately 28 - 30 hpf, ***Figure 2 – figure supplement 1***). Interestingly, the cytoplasm of characteristic elongated HE cells located on the aortic floor is filled with more-or-less large membrane vesicles that carry eGFP-Podxl2 (the largest vesicles reaching approximately 30μm in diameter). This suggests that HE cells contain a reservoir of eGFP-Podxl2 membranes that may be subjected to exocytose; as such, HE cells may be comparable to endothelial cells organizing a vascular lumen and that have been proposed to exocytose large intracellular macropinocytic-like vacuoles when cultured in 3D extracellular matrices (Bayless and Davis 2002; Davis, Bayless, and Mavila 2002) or, *in vivo*, in the zebrafish model (Kamei et al. 2006; Lagendijk, Yap, and Hogan 2014). This finding is unexpected since HE cells are assumed to possess aortic cell characteristics (i.e exhibit an apicobasal polarity) as they are supposedly integrated in the aortic wall contemporarily to aortic precursors (Jin et al. 2005) and may have been taking part in the lumenization of the ancestral vascular cord, a process that takes place around 18-20 hpf. Consequently, loss of apicobasal polarity features of HE cells at 28-30 hpf may be part of the programme that initiates the EHT process.

Although technically difficult for long hours (because of important variations in the volume of the balled yolk that trigger drifting of embryos), we have been able to follow through time non-polarized HE cells and to visualize the evolution of their vesicular content, starting at the initiation of the EHT time-window (around 35 hpf, see ***Figure 2*** and ***Figure 2 – figure supplement 2***). Interestingly, we could follow a dividing HE cell for which the vesicular content labelled with the polarity marker Podxl2 (eGFP-Podxl2) appeared to partition unequally between daughter cells (***Figure 2A,*** EHT cell 1' inherits the largest macropinocytic-like vacuole and emerges unambiguously as an EHT pol+ cell). This suggests that asymmetric inheritance of cytosolic vesicles containing apical proteins may contribute, presumably after delivery to the luminal membrane, to the acquisition of apicobasal polarity by EHT pol+ cells.

Altogether, these results support the idea that the HE, at the initiation of the EHT time-window, is not polarized. Subsequently, HE cells establish – or not – apicobasal polarity, thus leading to the emergence of either EHT pol+ or EHT pol- cell types (see our model ***Figure 2B***). In the case of EHT pol+ cells and while emergence is proceeding, apicobasal polarity is maintained (if not reinforced) until the release.

Tuning of apicobasal polarity is sensitive to interfering with the Runx1 transcription factor and with blood flow

To substantiate our findings on the significance of controlling apicobasal polarity establishment on EHT sub-types, we explored the potential involvement of proteins of the Pard3 family; these proteins, recruited by transmembrane receptors via their PSD-95/Dlg/ZO-1 (PDZ) domains (Buckley and St Johnston 2022), are at the root of apicobasal polarity initiation and are essential for the maintenance of apical membrane functional properties (Román-Fernández and Bryant 2016). We anticipated that interfering directly with Pard3 proteins would hamper the development of the aorta (in addition to other functions of polarized tissues that are essential for embryonic development) and rather searched for correlative evidence for the

differential expression of Pard3 isoforms - including natural loss or gain of function variants -, at critical time windows of the EHT process (i.e between 30-32 hpf (the timing at which the HE, as we show, does not appear to be polarized) and 48-50 hpf (the timing at which, as we show, part of HE cells have become competent to undergo emergence)). In addition, to provide functional support to this analysis and ensure that differences relate to what is taking place in hemogenic cells, our experimental conditions also included interfering with the gradual maturation of the HE (we have estimated that HE cells represent approximately 30% of total aortic cells at 48 hpf and others have estimated that they reach up to approximately 50% of total aortic cells at 28 hpf (Zhao et al. 2022)). We altered the maturation of the HE by abrogating blood flow and, more restricted to the EHT biological process *per se*, by interfering with the function of the Runx1 transcription factor whose expression is sensitive to fluid sheer stress (Adamo et al. 2009) and whose function is essential for EHT completion (Kissa and Herbomel 2010) and for regulating HSC number (Adamo et al. 2009; T. E. North et al. 2009).

Firstly, to reach these objectives, we sought to identify Pard3 isoforms that may be functionally relevant during EHT progression, using whole-mount *in situ* hybridization (WISH), RT-PCR and cloning. WISH performed at approximately 35 hpf allowed us to detect, in the aorta, mRNAs encoding for all Pard3 members, including Pard3ab, b, ba and bb, with prominent detection of Pard3ab and bb isoforms (see ***Figure 3A*** and ***Materials and Methods***). Messenger RNAs, in the trunk region and encoding for all four isoforms, were also detected by qRT-PCR during the 30-32 and 48-50 hpf time windows (data not shown). We also obtained and cloned partial or complete cDNAs encoding for all four members after reverse transcription of mRNAs expressed in the trunk region of 48 hpf embryos. Sequencing unveiled yet unreferenced variants and, of relevance regarding our objectives, potential loss of function proteins for Pard3ab and Pard3bb (see ***Figure 3B*** and ***Materials and Methods***); these include, for Pard3ab, a deletion of most of the sequence but that retains the amino-terminus containing the conserved region 1 (CR1) as well as the PDZ1 domain and, for Pard3bb, a

carboxy-terminal truncation of the PDZ3 domain that nonetheless maintains the carboxy-terminal sequence of the protein (see ***Figure 3B*** and its legend for more details).

Secondly, to interfere with Runx1 function, we generated a *Tg* fish line that expresses a truncated form of Runx1 (dt-runx1; fish line *Tg(Kdrl:Gal4;UAS:RFP;4xNR:dt-runx1-eGFP)* thereafter abbreviated *Tg(dt-runx1)*) deleted from its transactivation domain and carboxy-terminus but retaining its DNA-binding domain (the Runt domain (aa 55-183 (Kataoka et al. 2000; Burns et al. 2002; Kalev-Zylinska et al. 2002), see ***Figure 3C)***. Importantly, in this *Tg* fish line, dt-runx1 expression is restricted to the vascular system, hence excluding expression in the brain region that express Runx1 endogenously (see the aforementioned articles) and preventing biases owing to potential interference with neuronal functions. In addition, owing to the expression of eGFP concomitantly to dt-runx1 (eGFP is cleaved from dt-runx1 via a T2a site for endopeptidase), this fish line allows for the easy selection of embryos for imaging and for phenotypic analysis. In preliminary experiments aimed at addressing the localization of dt-runx1 as well as its stability, we expressed it transiently and measured its proper targeting to the nucleus, see ***Figure 3C)***.

To characterize further the *Tg(dt-runx1)* fish line, we performed time-lapse experiments using spinning disk confocal microscopy (with some of the experiments addressing apicobasal polarity performed with embryos obtained from outcrossing the *Tg(dt-runx1) and Tg(Kdrl:mKate2-Podxl2)* fish lines). Overall, we made the following observations: (i) hematopoiesis is affected, as attested by the significant increase in the number of hematopoietic cells in the thymus, at 5 dpf (days post-fertilization), in comparison to control siblings (***Figure 3- figure supplement 1***); (ii) at 30-32 hpf and contrarily to what we observed with our fish lines expressing either eGFP-Podxl2 or mKate2-Podxl2, HE cells appear to be polarized, based on enrichment of the polarity marker at luminal membranes. In addition, HE cells do not appear to contain any visible intra-cytosolic Podxl2-containing vesicles (***Figure 3-figure supplement 2,*** compare with ***Figure 2 and Figure 2- figure supplement 1***); (iii) at 48-

55 hpf, we observe an accumulation of EHT pol+ cells both in the aortic floor and in the lateral sides of the aortic wall as well as of cells of uncharacterized nature (the latter may, hypothetically, represent EHT cells at an early phase of their emergence, including cells that should have evolved as EHT pol- cells (see ***Figure 3*** - ***figure supplement 3A***)); (iv) occasionally, we observe - for EHT cells exhibiting invagination of the luminal membrane -, scattered cytosolic and sub-plasmalemmal pools of Podxl2-containing membranes and, consistently, the apparent decrease of Podxl2 enrichment at the apical/luminal membrane (see ***Figure 3*** - ***figure supplement 3B*** and compare with ***Figure 1C***). In addition and occasionally as well, we observe the reversion of apparent EHT pol+ cells into apparent EHT pol- cells (data not shown). These two last observations suggest that perturbing the tuning of apicobasal polarity in the HE alters the morphodynamic characteristics of emergence types, particularly in the case of EHT pol- cells whose biomechanical features appear to require turning down apicobasal polarity establishment.

Altogether, the results obtained upon expression of dt-runx1 show impairment of hematopoiesis and suggest that, for both EHT cell types, the progression throughout EHT is perturbed, and so until the release. The accumulation of morphologically characterized EHT pol+ like cells that we observe may result from the sustained apicobasal polarity of the HE at early time points (around 30 hpf). Consistently, this appears to be detrimental to the emergence of EHT pol- cells that we could not identify unambiguously and that may be part of the cells that are of uncharacterized morphologically. In addition, our results suggest that precursors of HE cells are polarized, as is expected to be the case for non-hemogenic aortic cells, and that Runx1 is involved in controlling the molecular events that are tuning apico-basal polarity, starting at the initiation of the EHT time-window.

We then pursued our aim to correlate, using qRT-PCR, the expression levels of Pard3 isoforms with the apicobasal polarity status of the hemogenic tissue during the EHT critical time windows (30-32 versus 48-50 hpf). To complement interference with Runx1 function upon expression

of dt-Runx1, we also prevented blood flow initiation using the well characterized *silent heart (sih)* morpholino which inhibits the expression of cardiac troponin T (Sehnert et al. 2002).

In a first series of 3 independent experiments performed with cDNAs obtained from dissected trunk regions of embryos at 30-32 and 48-50 hpf (***Figure 4A***), we measured the expression levels of the four Pard3 isoforms using heterozygous *Tg(dt-runx1)* fishes that were incrossed so as to obtain embryos expressing the highest possible amounts of dt-runx1, based on eGFP fluorescence resulting from proteolytic cleavage of the dt-runx1-eGFP fusion. To validate the efficiency of our interference conditions, we also measured expression levels of cmyb (an early marker of hematopoiesis) and of Scrib (a polarity protein involved in the functional delimitation of the cellular basal domain (Buckley and St Johnston 2022)). The qRT-PCR results show, for all Pard3 isoforms, a reproducible tendency for opposite effects of dt-runx1 expression between the 30-32 and 48-50 hpf time-windows, with the significant decrease of values for Pard3ab and bb at 48-50 hpf in comparison to controls. This suggests that the expression levels of Pard3 polarity proteins are differentially controlled between the two time-windows, indicating that the expression level of Pard3 polarity proteins is positively controlled in the wild type situation when emergence is proceeding at 48-50 hpf, but that it is rather negatively controlled, and thus decreased, at early time points (during HE maturation, at 30-32 hpf). These data and conclusions are also supported by results obtained with Scrib, with a comparable outcome. Importantly, cmyb expression was significantly decreased for both time-windows, consistently with the impairment in Runx1-dependent control of hematopoiesis.

In a second set of 3 independent experiments, we interfered with blood flow using the *Tg(Kdrl:Gal4;UAS:RFP)* fish line after injection of the *sih* morpholino (MO) in 1 cell stage embryos. We focused on Pard3ab and Pard3bb isoforms (***Figure 4B***). We reproduced the results obtained for Pard3ab and Pard3bb upon dt-runx1 expression, with less variability and consistently with the function of blood flow in controlling Runx1 expression (Adamo et al. 2009).

Finally, we also investigated expression levels of the +/- PDZ2 and +/- PDZ3 variants of Pard3ab and Pard3bb, respectively (using, as for experiments reported in ***Figure 4B***, incrosses of heterozygous *Tg(dt-runx1)* fishes, see ***Figure 4C -*** *left*). We found that, at 48-50 hpf and for both proteins, isoforms including the full-length PDZ domains are the most decreased, hence being positively controlled in the wild type Runx1 context. This reinforces the consistency of our findings as well as the importance of controlling expression levels of fully active polarity proteins when emergence is proceeding. We also confirmed our results using *sih* MO injections, at least for the Pard3ab +/-PDZ2 variants (***Figure 4C –*** *right).* Interestingly, the ratios between the Pard3ab +/-PDZ2 variants are opposite between the 30-32 hpf and 48-50 hpf time windows, reinforcing the idea of a fine tuning of apicobasal polarity functions mediated by aortic environmental constraints imposed by blood flow.

Junctional recycling is differentially controlled between EHT cell types

To investigate the functional links between apicobasal polarity and the peculiarities of EHT pol+ and EHT pol- emergence processes, we sought to follow the dynamics of Junctional Adhesion Molecules (JAMs) that belong to tight junction complexes (Garrido-Urbani, Bradfield, and Imhof 2014). During apicobasal polarity establishment in epithelial and endothelial tissues, these molecules recruit the Pard3/aPKC complex, via a PDZ-binding peptide located at their extreme carboxy-terminus (***Figure 5A*** and (Itoh et al. 2001; Ebnet et al. 2001; 2018)). In addition, JAMs are expressed in the vascular system and, in relation to this work, JAM3b is expressed in the aorta of the zebrafish embryo and promotes endothelial specification and hematopoietic development (Kobayashi et al. 2020).

We envisaged a scenario whereby EHT pol+ cells, whose longitudinal interface with endothelial neighbours shrinks along the X axis of the X, Y 2D-plane, may have less mobile junctional pools than EHT pol- cells whose entire junctional interface moves along the X, Y, Z 3D-axes (***Figure 5 - figure supplement 1)***. In the case of EHT pol- cells, the consumption of

the junctional interface with adjoining endothelial cells appears to result from the converging migration of endothelial neighbours crawling over the luminal membrane, based on interpretation of our time-lapse sequences (***Figure 1- video 3***). In this context, we favoured the analysis of junctional pools localized at antero-posterior sites of emerging cells as we have shown that they are enriched with tight junction components (Lancino et al., 2018). In addition and in the case of EHT pol+ cells, it is conceivable that these adhesion pools – spatially restricted owing to apicobasal polarity –, contribute to anchoring the emerging cell in the 2D-plane (***Figure 5 - figure supplement 1****).*

To achieve our goal, we designed 2 constructs in which eGFP is introduced in the extracellular domains of the two JAM2a and JAM3b molecules (***Figure 5A***). To investigate their localization and proper targeting at junctional interfaces, these constructs were expressed transiently and ubiquitously, using the *Hsp70* heat shock promoter. We observed that the 2 fusion proteins are efficiently targeted at cellular contacts and, more specifically, at the apical side of polarized epithelia such as for example cells of the ependymal canal (***Figure 5 - figure supplement 2***). We then established Tg fish lines expressing eGFP-Jam2a and eGFP-Jam3b under the control of the vascular kdrl promoter (*Tg(kdrl:eGFP-Jam2a)* and *Tg(kdrl:eGFP-Jam3b)*). Using these fish lines and spinning disk confocal microscopy, we observe a remarkable efficiency of targeting to intercellular junctions, for both proteins (data not shown for eGFP-Jam2a; for eGFP-Jam3b, see ***Figure 5B, C***). Deployment of the aortic wall into 2D cartographies allows to point precisely at junctional pools established at the interface between endothelial and EHT cells and emphasizes on the enrichment of eGFP-Jam3b at antero-posterior poles of EHT pol+ and EHT pol- cells (***Figure 5B, C*** *bottom*).

Using double transgenic *Tg(kdrl:eGFP-Jam3b; kdrl:nls-mKate2)* embryos at 48-55 hpf, we addressed the recycling capacity of junctional pools using Fluorescence Recovery After Photobleaching (FRAP). The labelling of nuclei with nls-mKate2 allowed to point at EHT pol+ and EHT pol- cells unambiguously because eGFP-Jam3b is essentially targeted to junctional

383 contours and not labelling peripheral membranes, except in few cases (and nuclei of EHT pol+
384 cells have a crescent shape, see ***Figure 6A***).
385 First and to set up our protocol, we spotted bi- and tri-junctional contacts between endothelial
386 cells (***Figure 6 – figure supplement 1***). Recycling parameters (fluorescence intensity
387 recovery with time and maximum recovery amplitude (that addresses the mobile pool), ***Figure***
388 ***6C***) showed that bi-junctional contacts are less mobile than tri-junctions, with a higher
389 dispersion of maximum recovery amplitude values for the latter (***Figure 6E***); this introduced a
390 clear limitation for statistical significance of the results, although clear tendencies were
391 observed for mean fluorescence intensity recovery ***(Figure 6C)*** and median values for
392 maximum recovery amplitude ***(Figure 6E)***. We then focused at antero-posterior sites of EHT
393 pol+ and EHT pol- cells and more specifically in the region of tricellular junctions (shared by 1
394 EHT cell and 2 endothelial neighbours, see ***Figure 6 – figure supplement 1***) that are clearly
395 the most enriched with eGFP-Jam3b. In each experiment, eGFP-Jam3b pools at tricellular
396 junctions between endothelial cells were also spotted for a comparative analysis.
397 Measurements of fluorescence recovery intensities revealed a significant increase in the
398 mobile fraction of eGFP-Jam3b at EHT pol+ – EC versus EHT pol- – EC junctional interfaces
399 (median values of 50% and 39% maximum recovery amplitudes after 10 min, respectively;
400 ***Figure 6E***)). Differences in recovery were also measured between EHT pol+ – EC and EHT
401 pol- – EC junctional interfaces when focusing on the earliest time points (the first 30 seconds,
402 ***Figure 6F***), although with smaller significance, with the median value of early recovery slopes
403 for the EHT pol+ - EC versus EHT pol- – EC junctional interfaces increased by 128% (***Figure***
404 ***6G***).
405 Altogether and unexpectedly regarding our initial scenario, these results indicate that tri-
406 junctional pools localized at antero-posterior poles of EHT cells and enriched with eGFP-
407 Jam3b molecules are significantly more dynamic for EHT pol+ cells in comparison to EHT pol-
408 cells. Since EHT pol+ cells - by virtue of apicobasal polarity establishment possibly assemble

an apical endosome -, this should favour the rapid recycling of eGFP-Jam molecules (Ebnet et al. 2003). This recycling may entertain a certain rate of delivery of Pard3 proteins at apical junctional regions and contribute to the maintenance/reinforcement of polarity throughout the entire emergence process. In addition, this turnover may be adapted to the mechanical tensions EHT pol+ cells are exposed to, in comparison to EHT pol- cells, owing to their specific morphodynamic features (ex: cellular bending); these tensions may be sensed by tri-cellular junctions which would be preferential sites for the renewal of junctional components whose half-life is reduced owing to submission to mechanical forces.

ArhGEF11/PDZ-Rho GEF plays essential functions during EHT progression

Junctional maintenance and recycling are dependent on intracellular membrane trafficking, supported by sub-cortical actin remodelling and actomyosin contractility, which are controlled mainly by GTPases of the Rho family (Ridley 2006; Olayioye, Noll, and Hausser 2019). Owing to the significance of apicobasal polarity control on EHT features, as suggested by our work, we investigated which proteins may be essential for actin/actomyosin regulation and focused on regulators of Rho GTPases, in particular Rho GEFs that catalyse exchange of GDP for GTP to positively regulate their activity (Rossman, Der, and Sondek 2005). As for Pard3 proteins, several of these Rho GEFs contain one or several PDZ domain(s) that target most proteins to complexes acting at the apical side therefore interlinking actin/actomyosin regulation with cell polarity (Mack and Georgiou 2014; Ebnet and Gerke 2022). We focused on 9 PDZ-domain containing Rho GEFs, all encoded by different genes in the zebrafish (***Figure 7- figure supplement 1***): ArhGEF11/PDZ-RhoGEF (thereafter shortened as ArhGEF11), ArhGEF12a, ArhGEF12b, PRex1, PRex2, Tiam1a, Tiam1b, Tima2a, Tiam2b. We first investigated their expression by Whole mount In Situ Hybridization (WISH) and found that all 9 mRNAs are detected in the aorta, and for the vast majority at 30-32 and 48-50 hpf (***Figure 7- figure supplement 2*).** Then, using qRT-PCR (***Figure 7- figure supplement 1B***), we measured and

compared their expression levels in the trunk region (at 35 and 48 hpf), for dt-runx1 expressing embryos and controls. We found that, in comparison to controls, ArhGEF11, ArhGEF12b, Tiam1b and Tiam2a are significantly reduced upon dt-runx1 expression at 48 hpf (hence being positively controlled in the wild type condition) and that their expression appears to be oppositely controlled at 35 hpf; this mirrors the variations measured for polarity proteins (***Figure 4***). This is consistent with a functional link between these Rho-GEFs and apicobasal polarity control during EHT progression. We finally decided to focus on ArhGEF11 for the following reasons: (i) in comparison to Tiams that act on Rac1, ArhGEF11 and ArhGEF12 (which are close relatives and can form heterodimers (Chikumi et al. 2004)), are mostly acting on RhoA which is controlling apical constriction via the RhoA-Myosin II signalling axis; as we have shown previously (Lancino et al. 2018), EHT progression requires the constriction of circumferential actomyosin; (ii) ArhGEF11 was shown to regulate the integrity of epithelial junctions by interacting directly with the scaffolding protein ZO-1, hence connecting inter-cellular adhesion with RhoA-Myosin II (Itoh et al. 2012); (iii) ArhGEF11 mediated apical constriction is essential during tissue morphogenesis such as, for example, the neural tube formation in which epithelial cells, submitted to mediolateral contractile forces, constrict at their apical side thus triggering inward bending of the neural plate which leads to the formation of the neural tube (Nishimura, Honda, and Takeichi 2012). The EHT may share features with this process, i.e the anisotropic distribution of contractile forces controlling the plane of emergence; (iv) mammalian ArhGEF11 exhibits alternative splicing in its C-terminal region that controls tight junction stability via the regulation of RhoA activity (Lee et al. 2018) as well as cell migration and invasion (Itoh et al. 2017).

To confirm the potential function of ArhGEF11 at the junctional interface between HE/EHT and endothelial cells, we first investigated its intracellular localization. We attempted to detect the full-length form upon expression of a GFP fusion protein, in the vascular system, and failed to do so. We then generated a truncated form that retains the N-terminal fragment encompassing the PDZ and RGS domains (see ***Figure 7 – figure supplement 3A***) fused with eGFP in its C-

462 terminus. Upon transient expression in the vascular system, we visualized its localization at
463 the interface between endothelial and hemogenic cells progressing throughout the EHT, with
464 an apparent increase in density at antero-posterior regions between adjoining EHT cells
465 (***Figure 7 - figure supplement 3B***).

466 In line with the formerly described function of a splicing variant of ArhGEF11 in controlling tight
467 junction integrity, particularly during egression of cells from the skin epithelium in the mouse
468 (Lee et al. 2018), we questioned the potential role of such variant in EHT. This variant, referred
469 to as the mesenchymal form, results from the inclusion of a peptide encoded by exon 37 or
470 exon 38 in mouse and human, respectively (Shapiro et al. 2011; Itoh et al. 2017; Lee et al.
471 2018). This insertion locates in the degenerated C-terminal region of the protein, which is
472 predicted to be relatively poorly organized in its 3D structure. Upon amplifying the full-length
473 sequence of zebrafish ArhGEF11 for investigating its localization, we cloned fragments
474 encoding – or not – for the insertion of a peptide of 25 amino-acid residues (75 base pairs
475 corresponding to exon 38). Although variable when compared with other species (see ***Figure***
476 ***7 – figure supplement 4C,*** *bottom panel*), this peptide is inserted in the same region as it is
477 for mammals and may correspond to an ArhGEF11 variant functionally equivalent and involved
478 in the regulating of junctional stability (see ***Discussion***).

479 To investigate the function of ArhGEF11 on the junctional interface between HE/EHT and
480 endothelial cells, and more specifically of the isoform containing the exon 38 encoded peptide,
481 we used both morpholino (MO) and CRISPR-based strategies. We designed a splicing MO at
482 the 3-prime exon/intron boundary of exon 38 that interferes with its inclusion in the encoding
483 mRNA (***Figure 7 - figure supplement 4A***). This MO did not trigger any deleterious effect on
484 the gross morphology of zebrafish embryos (***Figure 7 – figure supplement 4B***) and blood
485 circulation was normal in comparison to control embryos. We attempted to generate CRISPR-
486 based genomic deletion mutants of exon 38, both using Cpf1 and Cas9 enzymes and failed
487 (see ***Materials and Methods***). However, using CRISPR/Cas9, we obtained a deletion mutant

triggering a frame shift downstream of exon 38 and introducing a premature stop codon few amino-acid residues downstream thus leading to a sequence encoding for an ArhGEF11 C-terminal deleted form (see ***Materials and Methods*** and ***Figure 7- figure supplement 4C***)). Unlike the variant skipping exon 38 induced by the splicing MO, expression of the CRISPR/Cas9 C-ter deletion mutant triggered, around 24 hpf, a severe retardation of blood circulation initiation in approximately 80% of the embryos obtained from incrossing ArhGEF11$^{CRISPR\text{-}Cterdel\text{-}/+}$ heterozygous mutant fishes. From 24 to 48 hpf, approximately 50% of these embryos recovered a normal blood circulation (suggesting that these embryos are probably heterozygous for the mutation), approximately 35% remained with a severe phenotype (characterized by a large pericardiac oedema) and approximately 15% died, see ***Figure 7 – figure supplement 4D*** and ***Materials and Methods***). This indicates essential functions of the C-ter region of ArhGEF11, in agreement with previously published data on the mammalian protein (Chikumi et al. 2004).

We then characterized more in depth the MO and CRISPR phenotypes and performed a quantitative analysis of the number and morphology of HE, EHT and adjoining endothelial cells, based on confocal images and subsequent segmentation of cell contours (using 2D deployment of the aortic cylinder).

For the morphants, we found approximately a double amount of hemogenic cells in the aortic floor (altogether localized on the floor and on the lateral sides of the aorta, see ***Figure 7A*** and ***Figure 7 - figure supplement 5***); increase in the number of hemogenic cells also concerned cells oriented more perpendicularly to the blood flow axis (toward the Y-axis, ***Figure 7Aa''***), consistently with variation in emergence angle, as we have shown previously (Lancino et al. 2018). This is accompanied by a significant reduction in the number of morphologically characterized EHT cells (***Figure 7A*** and ***Figure 7 – figure supplement 5***). Similar results were obtained for the CRISPR homozygous deletion mutants, particularly regarding the accumulation of hemogenic cells, although with a smaller amplitude (***Figure 7B*** and ***Figure 7***

514 ***- figure supplement 6***). Consistently, a significant increase in the aortic perimeter was found,
515 at least for the morphants (***Figure 7C***). Of notice also, hemogenic cells in morphants are on
516 average less elongated in comparison to control and to the CRISPR homozygous mutants (as
517 well as less dispersed according to this parameter), with the accumulation of a cell population
518 standing below the median value (***Figure 7Aa''';*** to some extent, this is reproduced as well
519 when measuring hemogenic cell area). Finally, the population of small cells in the morphants
520 are of uncharacterized morphology, which means that they appear neither as EHT pol+ nor as
521 EHT pol- cells and may represent abortive emergences (***Figure 7A*** and ***Figure 7 – figure***
522 ***supplement 5*** in which cellular morphology can be assessed from z-stacks).
523 Altogether, the morphants and CRISPR mutant phenotypes show that the progression
524 throughout EHT is significantly impaired supporting the idea that ArhGEF11 exerts important
525 functions in the process. Increase in the frequency of elongated cells for the CRISPR mutants
526 in comparison to morphants suggests that interference triggered by the C-ter deletion of
527 ArhGEF11 is more effective at early time points. Interference with inclusion of exon 38 in
528 morphants triggers an increase in the number of hemogenic cells of smaller area and reduced
529 elongation indicating a more efficient progression throughout emergence in comparison to the
530 CRISPR mutants, albeit with impairment at later stages. This may be due to alteration in the
531 dynamics of endothelial cell intercalation which is required for emergence completion (which
532 is also compatible with the accumulation of pairs of cells that may be post-mitotic and that do
533 not spread apart because this also requires aortic cell intercalation).
534

535 **ArhGEF11/PDZ-RhoGEF and its variant containing the exon 38 encoded sequence**
536 **control junctional dynamics to support reduction of the hemogenic/endothelial**
537 **interface and cell-cell intercalation**

538 To investigate how ArhGEF11 controls the dynamic interplay between HE/EHT and endothelial
539 cells, we characterized further the MO and CRISPR phenotypes, at the junctional level. To do

so, we performed FRAP experiments using the *Tg(Kdrl:eGFP-Jam3b)* fish line that was injected at the one cell stage with the exon 38 splicing MO, or incrossing *(Kdrl:eGFP-Jam3b x* ArhGEF11$^{CRISPR\text{-}Cterdel\text{-}/+}$) heterozygous fishes to obtaining homozygous mutants and wild type alleles for control siblings.

FRAP experiments were focused on the hemogenic (HE)/endothelial (EC) membrane interface, with the support of images obtained after 2D deployments of aortic segments (***Figure 8A***). Pools of *eGFP-Jam3b* molecules localized at bi-junctional (HE-EC) and at tri-junctional (HE-EC-EC and HE-HE-EC) interfaces were bleached and subsequently imaged for FRAP analysis. In the case of the MO treatment (in which case HE cells accumulate on the aortic floor (see ***Figure 7A*** and the 2D cartography of the aortic floor ***Figure 8A***)) we measured, in comparison to control, an increase in FRAP recovery parameters for *eGFP-Jam3b* pools at the tri-junctional HE-HE-EC interface (***Figure 8B***), which is the most significant for the recovery speed at early time points (***Figure 8B, b''')***. Results are different for the ArhGEF11$^{CRISPR\text{-}Cterdel+/+}$ homozygous mutants for which we did not observe any obvious effect at HE-HE-EC tri-junctions (***Figure 8C***) but, rather, a small tendency for an increase in the mobile pool at HE-EC-EC tri-junctions (that has the particularity to concern 2 endothelial cells that contact the longitudinal membrane of one HE cell, see ***Figure 8A, D***).

Altogether and including our results presented ***Figure 7***, these results reinforce the idea that ArhGEF11 and its variant encoded by exon 38 are involved in critical steps of EHT progression, partly by controlling the dynamics of junctional pools at the level of tri-junctions established between adjoining hemogenic and endothelial cells (see the model ***Figure 8D*** and its legend for a detailed analysis of mechanistic issues). The results also suggest that the +exon 38 peptide encoding variant is prominently involved in controlling the HE-HE-EC interface and more specifically during intercalation, consistently with the accumulation, upon MO interference, of EHT cells having progressed throughout the emergence but appearing to be slowed down when reaching completion (cells of smaller area and less elongated, see ***Figure***

566 ***7***). Finally, ArhGEF11 is controlling RhoA and, most probably, its function in EHT progression
567 also involves actin and acto-myosin activities that are involved in the contraction of HE and
568 EHT cells (see Lancino et al. 2018; this is coupled with the consumption of longitudinal and
569 transversal membrane interfaces, see also the model ***Figure 8D*** and its legend).
570

571 # Discussion

572 **Characteristics of the HE and complexity of pre-hematopoietic stem cell emergence**
573 Heterogeneity in the identity and hematopoietic potential of cells emerging from the HE in the
574 AGM has been recently shown in co-culture systems and *in vivo* in the mouse (Ganuza et al.
575 2017; Dignum et al. 2021) and in the zebrafish model (Tian et al. 2017; Xia et al. 2023);
576 however, knowledge on the fundamental cell biological and molecular events leading to this
577 complexity is still lacking. Here, we highlight functional aspects that may significantly contribute
578 to this complexity and that take root in the cellular plasticity of the HE. We bring evidence
579 suggesting that HE cells that become competent to initiate the EHT time-window (around 28-
580 30 hpf) tune their apicobasal polarity status which endows them with the ability to support two
581 emergence processes with radically different morphodynamic characteristics; eventually, this
582 would lead to differentially fated cells, which remains to be determined.
583 While the ability of the HE to regulate its polarity features may be inherited from molecular
584 cues involved in its upstream intra-aortic specification (such as for example NOTCH (Robert-
585 Moreno et al. 2008; Gama-Norton et al. 2015; Bonkhofer et al. 2019), TGFβ (Monteiro et al.
586 2016), Gata2 (Butko et al. 2015; Daniel et al. 2019)), or any other of the more upstream factors
587 involved in hemogenic specification (Zhao et al. 2022)), our results suggest that Runx1 is
588 taking part in this regulation, consistently with its hematopoietic and EHT-inducing activity
589 (North et al. 1999; Kalev-Zylinska et al. 2002; Kissa and Herbomel 2010; Lancrin et al. 2012).
590 Our experiments using an interfering form of Runx1 (dt-Runx1) that produces a relatively weak
591 an subtle phenotype in comparison to morpholino treatment that prevents aortic cells to convert

592 into HE cells (Bonkhofer et al. 2019) or genetic mutation and gene knockout abrogating
593 hematopoiesis (T. E. North et al. 2009; Sood et al. 2010; Gao et al. 2018), provided the
594 opportunity to observe that, at 30 hpf, elongated HE cells on the aortic floor appear to be
595 maintained and to exhibit apicobasal polarity, with the absence of apparent cytosolic vacuolar
596 structures (as has been described in the mouse in Runx1 interfering condition (T. North et al.
597 1999)), which correlated with the subsequent accumulation of EHT pol+ cells that appeared to
598 be at the expense of EHT pol- cells. This is in favour of the idea that the two cell types arise
599 from a common precursor capable of evolving toward the one or the other, and that has lost
600 apicobasal polarity (see the model ***Figure 2B***). Recent work that has identified Runx1 targets
601 in the zebrafish embryo at 29 hpf does not point at any of the conventional apicobasal polarity
602 organizers as being direct targets although Pard3 and Pard6 mRNAs are clearly
603 downregulated in the HE in comparison to aortic roof cells (Bonkhofer et al. 2019) which is
604 consistent with our results at early time points of the EHT time-window.

605 A key question arising from our observations is what would control the balance orienting toward
606 an EHT pol+ or an EHT pol- type of emergence. Cell division may be orienting toward EHT
607 pol- emergence type (which would also be the reason why these cells have a round-shape
608 morphology in comparison to EHT pol + cells). The frequency of EHT pol+ versus EHT pol-
609 cells that we have estimated and that is of approximately 2/1 is not incompatible with this
610 possibility since divisions take place in the HE at a relatively high frequency. Indeed, it has
611 been estimated that 50% of HE cells that constitute the aortic floor at 28 hpf will divide and will
612 undergo emergence thereafter during the 28-72 hpf time window (Zhao et al. 2022). However,
613 we observe that both EHT pol+ and EHT pol- cells can divide during the emergence process
614 (see also our former work Lancino et al. 2018 for EHT pol+ cells), which is followed by the full-
615 recovery of their respective morphodynamic characteristics (not shown). Hence, this excludes
616 the possibility of a short term and purely mechanical effect of cell division on emergence
617 morphodynamics. In link with cell division however, there exist the possibility that the pool of

large vesicular structures potentially awaiting for exocytosis in HE cells having lost their apicobasal polarity may become asymmetrically inherited after division. This would endow the cell remaining with the largest pool to undergo EHT pol+ emergence after exocytosis and expansion of the apical/luminal membrane. Our results ***Figure 2*** would support this possibility but what controls this asymmetry would remain to be established.

Still, regarding the control of the balance orienting toward an EHT pol+ or an EHT pol- type of emergence, the intrinsic nature of the HE, i.e. its acquaintance with the aortic differentiation programme (Bonkhofer et al. 2019), raises the possibility of a partial recovery of an aortic cell phenotype in the case of EHT pol+ emergence, thus supporting its very unique mechanobiology. Therefore, the regulation of local signalling between aortic and HE cells may tune the balance toward the one or the other fate; this could be the case, for example, for adjoining HE cells in comparison to isolated ones that would then receive unequal signalling cues owing to the difference in homotypic versus heterotypic contacting surfaces. In this scenario, NOTCH signalling which is determinant for aortic and HE specification (Gama-Norton et al. 2015) may play a significant role, particularly via the ratio of the Jag1/Dll4 ligands that is fundamentally involved in HE versus aortic specification (Robert-Moreno et al. 2008; Bonkhofer et al. 2019).

Finally, we cannot totally exclude that EHT pol+ and EHT pol- cells would originate from different precursors. On this line, it has been shown that the aortic wall can home a transient veinous-fated progenitor cell population that will lead to the underlying vein via selective sprouting from 21 to 23 hpf (Herbert et al. 2009). This option would require a massive expansion of a minor fraction of the cell population remaining in the aortic floor since it is expected that most of it has been moving out toward the sub-aortic region, which is not in favour of this possibility. In addition, recent scRNAseq analysis of floor and roof aortic cells at 21 and 28 hpf has led, for both timing points, to two well defined clusters defined only by aortic and hematopoietic signatures (Zhao et al. 2022).

644

645 **The complexity of pre-HSC emergence and heterogeneity of hematopoietic stem cell**
646 **and progenitor populations**

647 Currently, we do not know what would be the features that would endow the two cell types to
648 behave differently after their release. Since post-EHT cells have to migrate in transient
649 developmental niches (i.e the CHT, the thymus, the pronephric region), these features may
650 provide them with more or less ability to migrate in the sub-aortic space and pass throughout
651 the wall of the underlying vein to conquest more distant niches (Murayama et al. 2006), or to
652 remain in a local AGM niche and be exposed to specific signalling there, in the proximity to the
653 aorta as it is the case for hematopoietic clusters in mammals and avians (Ciau-Uitz et al. 2014;
654 Jaffredo and Yvernogeau 2014). Beside their potential differences in colonizing different niches
655 which would impact on their subsequent fate, these cells may also contribute to more or less
656 transient waves of hematopoietic stem cells and progenitors that would be specific to the
657 developmental period such as, for example, a restricted sub-set of T-lymphocytes that was
658 described before (Tian et al. 2017). In the specific case of the Tian et al. work, the AGM was
659 shown to produces transient T-lymphocytes proposed to be independent of long-lived HSCs
660 according to a gradient that increases from the anterior to the posterior part of the trunk region,
661 as well as from the aorta in the tail (the posterior blood island in the tail region that was
662 proposed to give rise to hematopoietic precursors related to mammalian erythro-myeloid
663 progenitors, (Bertrand et al. 2007)). Since the EHT pol+ and EHT pol- cells that we describe in
664 our work are equally produced from the aorta in the trunk and in the tail regions (thus
665 irrespective of the antero-posterior axis of the aorta), the one or the other of the two EHT types
666 most probably does not directly relate to the first wave of T-lymphopoiesis arising from the
667 aortic endothelium described in Tian et al 2017.

668

669 **The cell biology behind emergence control and mechanics**

The intrinsic capacity of the HE, that we show here to be able to support two highly distinct emergence processes, in the zebrafish embryo, is very unique. Indeed, not only are they taking place contemporarily, but also can the two cell types proceed throughout emergence at a distance shorter than 50 μm, which accommodates the intercalation of a single adjoining endothelial cell. This may reflect the remarkable properties of the vascular system that needs to allow cellular extrusion and transmigration. The latter is particularly relevant in the context of developmental hematopoiesis since hematopoietic precursors that travel via blood circulation need to pass throughout the aortic wall to conquest their distant niches.

In the present work, we provide some of the mechanistic insights into the specificities of the two emergence types and that rely on two fundamental aspects of cellular biology, i.e apicobasal polarity establishment and junctional mobility. The establishment and maintenance of apicobasal polarity in a cell extruding from its environment, as is the case for EHT pol+ cells, is at odds with the fundamental mechanisms of cell extrusion irrespective of the context into which the process is taking place (Nieto et al. 2016; Gudipaty and Rosenblatt 2017; Pei et al. 2019; Staneva and Levayer 2023); this places the emergence of EHT pol+ cells as an extreme case of extrusion and it is somehow unexpected to observe this type of emergence when the aortic wall can extrude EHT pol- cells that appear to emerge contemporarily, apparently according to a more conventional mode. During the EHT time-window, Runx1 is directly controlling the emergence programme by regulating Rho-dependent cytoskeletal functions in HE cells derived from mouse ES lines (Lie-A-Ling et al. 2014) and inducing the expression of Gfi1ab in the zebrafish (Bonkhofer et al. 2019) that belongs to the family of transcriptional repressors of the arterial programme expressed in the HE (Gfi1 and Gfi1b in the mouse, (Lancrin et al. 2012)). This programme downregulates key molecules involved in the maintenance of the aortic endothelium among which Cdh5 (VE-Cadh) and the downregulation of cadherins is a hallmark of extrusion. Thus, for EHT cells, and particularly EHT pol+ cells, downregulation of VE-Cadh should be compensated by other mechanisms that allow for the

maintenance of aortic integrity. In this context of adhesion downregulation, the JAMs (that are expressed endogenously in the vascular system and that were used in this study) appear to be a well-suited substitute. As part of tight junction complexes, they can strengthen adhesion and, in addition, since they are also involved in cell migration (in particular leukocyte trans-endothelial migration, see (Ebnet 2017)), they could in theory support the extrusion of EHT pol- cells that do so according to a seemingly migration-type emergence mode (inferred from our time-lapse sequences) more or less related to trans-endothelial migration. In the case of EHT pol+ cells, we propose that JAMs may significantly contribute to the re-establishment of apicobasal polarity and to the strengthening of adhesion while EHT pol+ cells should undergo strong mechanical tension (owing to cellular bending). Interestingly, Jam3b appears to be a direct and positively regulated target of Runx1 (Bonkhofer et al. 2019), which is supporting its aforementioned potential functions during EHT.

Finally, regarding inter-cellular junctions and the control of their dynamics all along the EHT process, we also addressed the dynamic interface between aortic and HE cells. As for EHT cells, we focused more specifically on tri-junctional interfaces that have been proposed to sense tension and transmit the information to other types of junctional complexes (Bosveld, Wang, and Bellaïche 2018); in the EHT context, the contracting hemogenic endothelium is additionally exposed to high mechanical tension owing to wall sheer stress imposed by the blood flow and that was proposed to regulate emergence efficiency (Lundin et al. 2020; Campinho et al. 2020; Chalin et al. 2021). In our work, we highlight one essential aspect of controlling junctional recycling which is during cell-cell intercalation which concerns either contacting HE cells lying on the aortic floor or HE/EHT cells after cytokinesis (as mentioned before, cell division is rather frequent during the EHT time window (Zhao et al. 2022)). In this context, we addressed the function of ArhGEF11/PDZ-RhoGEF which provides a functional link between cell polarity (with its PDZ-binding motif and its RGS domain that couples to G-protein coupled receptor signalling to regulate planar cell polarity (Nishimura, Honda, and Takeichi 2012)), cell adhesion (it binds to the tight junction associated regulatory protein ZO-

1, (Itoh et al. 2012)), and cytoskeletal regulation/contraction (Itoh et al. 2012; Itoh 2013), all three essential mechanistic components of morphogenetic movements and tissue remodelling. Since morphodynamic events leading to cell extrusion and to the control of cell migration do not only rely on the regulation of mRNAs levels but also on alternative splicing (Pradella et al. 2017) our interest for investigating the function of ArhGEF11 in EHT was raised by the fact that the protein undergoes changes in its biological properties via the alternative splicing of a small exon which leads to a modification of its C-terminus. We identified a splicing event in this region (concerning exon 38) for a potential zebrafish isoform ortholog. However, the precise function of this variant for the zebrafish protein, that was shown in the case of the mammalian isoform to induce cell migration and motility (Itoh et al. 2017) and to bind to the Pak4 kinase thus leading to the subsequent destabilization of tight junction complexes via loss of RhoA activation (Lee et al. 2018), remains to be established. On this line, our results consistently indicate that preventing exon 38 insertion interferes with EHT progression (as well as deleting the C-terminus of the protein as shown with our CRISPR mutant) and appears to impair intercalation of aortic cells between adjoining HE cells. Hence, the +exon 38 isoform, by regulating the dynamic interplay between HE and endothelial cells, would favour one of the essential steps of the EHT process leading to its completion and requiring the complete isolation of EHT cells to ensure the ultimate sealing of the aortic floor (see our former work (Lancino et al. 2018)). It remains to be established, as our measurements indicate, why the ArhGEF11 +exon 38 isoform appears to slow down junctional recycling which is counterintuitive with increasing the HE/endothelial dynamic interface. However, upon interference, we have been following Jam3b recycling which is only a sub-population of tight junction components that should be at play in the system. Finally, the EHT process on its whole may be submitted to a complex regime of alternating contraction and stabilization phases as we have shown previously in the context of EHT pol+ emergence and that may reflect the necessity to adapt to mechanical constraints imposed by the environment as well as the rearrangements of the HE/EHT/aortic cellular interface (Lancino et al. 2018). In this context, back and forth regulatory mechanisms,

750 particularly involved in the control of the RhoA-Myosin II signalling axis partially regulated by
751 ArhGEF11, may locally and at specific timing points change the turnover of junctional
752 molecules, thus blurring the correlation between gross phenotype (here the organization of the
753 HE/aortic interface) and very local and dynamic molecular events (for a complement to the
754 discussion, see also the legend of the model presented ***Figure 8C***).

755 Overall, our work highlights the complexity of pre-hematopoietic stem cell emergence as well
756 as some of the essential molecular and mechanistic aspects involved. We show that the aorta,
757 in the zebrafish embryo, produces two fundamentally different types of EHT cells and propose
758 that this results from specific functional features of the HE regulated by the transcription factor
759 Runx1. This would support the production of cell types potentially endowed with different cell
760 fate potential, subsequently reinforced by the type of niche into which these cells will establish
761 homing. It now remains to be established if the different cell types that we describe are indeed
762 leading to cells that will eventually hold specific hematopoietic fate and properties.

Materials and Methods

Key Resources Table

For the exhaustive list of all primers, see Materials and Methods - Supplementary Table.

Reagent type (species) or resource	Designation	Source or reference	Identifiers	Additional information
strain, strain background (zebrafish *Danio rerio*)	AB	Zebrafish International Resource Center (ZIRC)	ZFIN: ZDB-GENO-960809–7	
strain, strain background (zebrafish *Danio rerio*)	Tg(kdrl:HsHRAS -mCherry): s916Tg	(Chi et al. 2008)	ZFIN ID: ZDB-ALT-090506–2	referred to as Tg(kdrl:Ras-mCherry)
strain, strain background (zebrafish *Danio rerio*)	Tg(kdrl:nls-mKate2)	N/A	N/A	
strain, strain background (zebrafish *Danio rerio*)	Tg(kdrl:Gal4;UAS:RFP)	N/A	N/A	
strain, strain background (zebrafish *Danio rerio*)	Tg(kdrl:Gal4;UAS:RFP;4xNR:eGFP-Podxl2)	This paper	N/A	
strain, strain background (zebrafish *Danio rerio*)	Tg(kdrl:mKate2-Podxl2)	This paper	N/A	
strain, strain background (zebrafish *Danio rerio*)	Tg(kdrl:eGFP-Jam2a)	This paper	N/A	
strain, strain background (zebrafish *Danio rerio*)	Tg(kdrl:eGFP-Jam3b)	This paper	N/A	
strain, strain background (zebrafish *Danio rerio*)	Tg(kdrl:Gal4;UAS:RFP;4xNR:dt-runx1-eGFP)	This paper	N/A	
strain, strain background (zebrafish *Danio rerio*)	Tg(ArhGEF11$^{CRISPR\text{-}Cterdel\text{-}/+}$)	This paper	N/A	
recombinant DNA reagent	pG1-flk1-MCS-tol2	(Jin et al. 2005)	N/A	
recombinant DNA reagent	pEGFP-C1	Clontech	N/A	
recombinant DNA reagent	Transposase pCS-zT2TP	(Suster et al. 2011)	N/A	

Reagent type (species) or resource	Designation	Source or reference	Identifiers	Additional information
recombinant DNA reagent	pmKate2-f-mem	Evrogen	Cat# FP186	
antibody	goat anti-rabbit Alexa Fluor 488	Invitrogen	Cat# A11070	1/400
antibody	rabbit anti-GFP	MBL	Cat# 598	1/300
antibody	mouse anti-HA	Sigma	Cat# 12ca5	1/50
antibody	goat anti-mouse HRP-conjugated	Thermo Fisher Scientific	Cat# G-21040	1/300
sequence-based reagent	Morpholino sih	Sehnert et al., 2002	ZDB-MRPHLNO-060317-4	CATGTTTGCTCTGATCTGACACGCA
sequence-based reagent	Morpholino ArhGEF11 exon 38	This paper	N/A	GAAATAAATGAAGCCCCACCTCCGT
sequence-based reagent	Oligo for CRISPR: Alt-R® CRISPR-Cas12a (Cpf1) crRNAs -1	This paper	N/A	TATCACACACACATCACCTTCTA
sequence-based reagent	Oligo for CRISPR: Alt-R® CRISPR-Cas12a (Cpf1) crRNAs -2	This paper	N/A	TTTCTCAGCGCTCCTGACAGATG
sequence-based reagent	Oligo for CRISPR: Alt-R® CRISPR-Cas9 crRNAs	This paper	N/A	AGCCAATCGTCTGAGGACGG
sequence-based reagent	Oligo for CRISPR: Alt-R® tracrRNA	IDT	Cat# 1072532	
software, algorithm	CRISPRscan	(Moreno-Mateos et al. 2015)		N/A
software, algorithm	Zen Pro2 software	Zeiss	https://www.zeiss.com/microscopy/en/products/software/zeiss-zen.html	N/A
software, algorithm	QUANTSTUDIO™ DESIGN & ANALYSIS 2	Thermofisher	https://apps.thermofisher.com/apps/da2/	N/A
software, algorithm	MetaMorph software	Molecular Devices	https://www.moleculardevices.com/products/cellular-imaging-systems/acquisition-and-analysis-software/metamorph-microscopy	N/A
software, algorithm	Acquisition-Imaging analysis-LAS X	Leica	http://www.leica-microsystems.com	N/A
software, algorithm	Image Analysis-Fiji	NIH	https://imagej.net/Fiji	N/A

Reagent type (species) or resource	Designation	Source or reference	Identifiers	Additional information
software, algorithm	Image Analysis Icy	(de Chaumont et al., 2012)	http://icy.bioimageanalysis.org/	N/A
software, algorithm	Image Analysis TubeSkinner plugin for Icy	(Lancino et al. 2018)	https://icy.bioimageanalysis.org/plugin/tubeskinner/	N/A
software, algorithm	Figures-Illustrator CC 2017.1.1	Adobe	http://www.adobe.com/cn/	N/A
software, algorithm	Active contour plugin	(Dufour et al. 2010)	https://icy.bioimageanalysis.org/plugin/active-contours/	N/A
software, algorithm	NIS software	Nikon	https://www.microscope.healthcare.nikon.com/en_EU/products/software/nis-elements	N/A
software, algorithm	Rstudio	RStudio Team (2020)	http://www.rstudio.com/}	N/A
software, algorithm	ggplot2	(Wickham 2016)	https://ggplot2.tidyverse.org.	N/A
software, algorithm	readr	(Wickham, Hester, and Bryan 2022)	https://github.com/tidyverse/readr	N/A
software, algorithm	cowplot	(Wilke 2020)	https://wilkelab.org/cowplot/	N/A
software, algorithm	dplyr	(Wickham et al. 2023)	https://github.com/tidyverse/dplyr	N/A
software, algorithm	wesanderson	(Ram and Wickham 2018)	https://github.com/karthik/wesanderson	N/A
software, algorithm	matrixStats	(Ram and Wickham 2018)	https://github.com/HenrikBengtsson/matrixStats	N/A
software, algorithm	stringr	(Wickham 2022)	https://github.com/tidyverse/stringr	N/A
software, algorithm	ggsci	(Xiao N et al. 2023)	https://github.com/nanxstats/ggsci.	N/A
software, algorithm	ggpubr	(Kassambara et al. 2020)	https://rpkgs.datanovia.com/ggpubr/	N/A
software, algorithm	ggstatsplot	(Patil 2022)	https://indrajeetpatil.github.io/ggstatsplot/index.html	N/A
software, algorithm	ggbeeswarm	(Clarke and Sherrill-Mix 2017)	https://github.com/eclarke/ggbeeswarm	N/A
software, algorithm	DT	(Xie, Cheng, and Tan 2022)	https://github.com/rstudio/DT	N/A

Reagent type (species) or resource	Designation	Source or reference	Identifiers	Additional information
software, algorithm	SciViews	(Grosjean 2019)	https://www.sciviews.org/SciViews/	N/A
software, algorithm	nls.multstart	(Padfield and Matheson 2020)	https://github.com/padpadpadpad/nls.multstart	N/A

766
767

768 **Contact for reagent and resource sharing**

769 Further information and requests for resources and reagents should be directed to and will be
770 fulfilled by the corresponding Author, Anne A. Schmidt (anne.schmidt@pasteur.fr).

771 **Zebrafish husbandry**

772 Zebrafish (Danio rerio) of the AB background and transgenic fish carrying the following
773 transgenes *Tg(kdrl:ras-mCherry)* (Chi et al. 2008); *Tg(kdrl:nls-mKate2)*;
774 *Tg(kdrl:Gal4;UAS:RFP); and the fish lines generated in this study:*
775 *Tg(kdrl:Gal4;UAS:RFP;4xNR:eGFP-Podxl2); Tg(kdrl:mKate2-Podxl2); Tg(kdrl:eGFP-Jam2a);*
776 *Tg(kdrl:eGFP-Jam3b)*; *Tg(kdrl:Gal4;UAS:RFP;4xNR:dt-runx1-eGFP); Tg(ArhGEF11*$^{CRISPR\text{-}Cterdel\text{-}/+}$*)* were raised and staged as previously described (Kimmel et al. 1995). Adult fish lines
778 were maintained on a 14 hr light/10-hr dark cycle. Embryos were collected and raised at either
779 28.5 or 24°C in N-Phenylthiourea (PTU, Sigma Aldrich, Cat# P7629)/Volvic source water
780 (0.003% final) to prevent pigmentation complemented with 280 µg/L methylene blue (Sigma
781 Aldrich, Cat# M4159). Embryos used for imaging, extracting mRNA, or for WISH ranged from
782 developmental stages 28-to-60 hpf and larvae used for imaging were of 3-5 dpf, precluding
783 sex determination of the animals. The fish maintenance at the Pasteur Institute follows the
784 regulations of the 2010/63 UE European directives and is supervised by the veterinarian office
785 of Myriam Mattei.

786 **mRNA extraction and cDNA synthesis**

Total RNA was extracted from whole 48 hpf embryos for cDNA cloning or from pooled trunks at the desired developmental stages (30-32 hpf, 48-50 hpf time windows for qRT-PCR experiments) (~30 individuals per tube). Briefly, embryos were anesthetized using balneation in embryo medium supplemented with tricaine methanesulfonate (MS-222, Sigma-Aldrich Cat# A5040), at a final concentration of 160 μg/ml. RNA was extracted via organic extraction using TRIzol reagent (Invitrogen Cat# 15596026) according to the manufacturer's guideline. gDNA contaminant was removed using TURBO™ DNase (Invitrogen Cat# AM2238) treatment according to the manufacturer's guideline. Total RNA was stored at -80°C. Reverse transcription of mRNA was performed using SuperScriptIV (Invitrogen Cat# 18090010) with OligodT primer. cDNA samples were stored at -20°C until further processing (for quantitative real-time PCR, PCR, cloning and sequencing).

Transient and stable transgenesis

The *kdrl* promoter (*flk*) (Jin et al. 2005) was used to drive endothelial expression of mKate2-Podxl2, eGFP-Jam2a and eGFP-Jam3b, with eGFP (Clontech) and mKate2 (Evrogen) cDNAs amplified using overlapping primers for Gibson cloning. eGFP-Podxl2, ArhGEF11(PDZ-PRD-RGS-eGFP) and dt-runx1-eGFP were amplified for cloning into a pG1-4XNR vector (built from the 4XNR (non-repetitive) 4X UAS sequence less susceptible to methylation than the 14X UAS described in (Akitake et al. 2011)). For the sequence of all the designed cloning primers, see the Key Resources Table.

Podocalyxin-like 2 (Podxl2), ArhGEF11/PDZ-RhoGEF, JAM2a and JAM3b full length sequences were amplified from pools of 48 hpf whole embryo cDNA (see before for mRNA extraction and cDNA synthesis methodologies). All constructs generated in this study were obtained using the Gibson assembly assay (NEB, Cat # E2611S).

For eGFP-Jam2a and eGFP-Jam3b cloning, we used the JAM2a signaling peptide sequence (included in the 5-prime amplification primers and encoding for the signal peptide: mlvcvsllilihsvpvspvtvssr) and, for both constructs, the eGFP sequence was inserted in frame

upstream of the sequence encoding for the transmembrane domain; for the eGFP-Jam2a construct, the eGFP was inserted upstream of amino-acid D221 (DLNVAA) of the NCBI Reference Sequence: NP_001091734.1; for the eGFP-Jam3b construct, the eGFP was inserted upstream of amino-acid D243 (DINIAG) of the NCBI Reference Sequence: NP_001076332.2. For transient ubiquitous and inducible expression, the eGFP-Jam2a and eGFP-Jam3b fusion constructs were inserted into a KpnI pre-digested pG1 plasmid containing tol2 sites and the HSP70-4 promoter. For stable transgenesis using the *kdrl* (*flk1*) promoter, constructs cloned into the pG1-HSP70 plasmids were extracted using XhoI/NotI restriction enzymes and inserted into the XhoI/NotI pre-digested pG1-flk1 vector using DNA T4 ligation (NEB, Cat # M0202S).

For the Podxl2 N-ter deletion mutant that has been used for establishing stable *Tg* fish lines, the cDNA encoding for the peptide sequence starting with amino-acid G341 (GGTEYL; fragment 341-587) of the NCBI Reference Sequence: XP_692207.6 was fused with either eGFP or mKate2 cDNAs. The sequence encoding for the signal peptide of the human CD8 (malpvtalllplalllhaarpsqfrvs) was introduced upstream (5-prime) of the eGFP or mKate2 sequences (included in the 5-prime primers designed for the Gibson cloning strategy). For the construct designed to obtain the *Tg(kdrl:Gal4;UAS:RFP;4xNR:eGFP-Podxl2)* fish line, 2 overlapping fragments were amplified for cloning into a pG1-tol2_4xNR vector after digestion with NcoI, with the following couples of primers: 4XNR_CD8-eGFP_fw and delPodxl2_eGFP_rev; delPodxl2_fw and Podxl2_pG1-4XNR_rev. For the construct designed to obtain the *Tg(kdrl:mKate2-Podxl2)* fish line 2 overlapping fragments were amplified for cloning into a pG1-flk1 vector after digestion with EcoR1, with the following couples of primers: pG1-flk1_CD8_mKate2_fw and delPodxL2-mKate2_rev; mKate2-delPodxL2_fw and Podxl2_PG1-flk1_rev.

For the ArhGEF11(PDZ-PRD-RGS-eGFP) construct, the cDNA encoding for the peptide ending upstream of the DH domain at Valine 709 of the amino-acid sequence (GenBank: AY295347.1; PALDEDV; fragment 1-709) was fused upstream of the sequence encoding for

840 eGFP, for expression using the pG1-4xNR vector. The cDNA was amplified using the
841 GB_4xUAS-gef11_fw; GB_eGFP-RGS_rev couple of primers.
842 For the construct designed to obtain the *Tg(kdrl:Gal4;UAS:RFP;4xNR:dt-runx1-eGFP)* fish
843 line, the Runx1 sequence amplified omits the ATG (replaced by an nls) and ends downstream
844 of the Runt domain (ending at amino-acid sequence PAHSQIP). The construct allows for the
845 expression of the dt-runx1 protein under the control of the 4xNR driver using the same strategy
846 as for the above PodxL2 constructs. The dt-runx1 cDNA construct was amplified from the
847 zebrafish Runx1 cDNA sequence (Kalev-Zylinska et al. 2002) using the couple of primers GB-
848 4xnr-nlsRunx1_fw; GB-eGFP-T2A-2xHA-delRunx1_rev. The sequence of these primers each
849 allowed for the introduction, in the protein sequence, of a nls (encoded by the fw primer) and
850 of a 2xHA-T2A peptide (encoded by the rev primer that overlaps with the 5-prime sequence of
851 eGFP).
852 For all constructs, cloning reactions were used to transform NEB 5-alpha Competent E. coli
853 (NEB, Cat # C2987) and resistant clones then used for miniprep plasmid preparations
854 (Nucleospin plasmid, Macherey-Nagel, Cat # 740588.50), followed by sequencing. Plasmid
855 DNA from clones containing correct insertions where then used to transform E. coli TOP10
856 competent cells (Invitrogen, Cat # C404010) and purified using the endotoxin free NucleoBond
857 Xtra Midi kit (Macherey Nagel, Cat# 740420.10). Transgenesis was then performed by co-
858 injecting 1 nl of plasmid (at 25 ng/μl) mixed with tol2 transposase mRNA (at 25 ng/μl)
859 transcribed from linearized pCS-zT2TP plasmid using the mMESSAGE mMACHINE SP6 kit
860 (Ambion, Cat# AM1340). For stable transgenesis, embryos were screened for fluorescence
861 between 24 hpf and 48 hpf and raised to adulthood. Founders with germline integration were
862 then isolated by screening for fluorescence after outcrossing with AB adults and for
863 establishment of the F1 generation.
864
865 **CRISPR methodology and GEF11 mutant transgenic line screening**
866 *CRISPR/Cas9 mutagenesis and isolation of founders*

A sgRNA was designed against the splice donor site at the end of exon 38 with the aim to interfere with the production of the splicing variant including its encoding sequence, using the CRISPRscan web tool (Moreno-Mateos et al. 2015). The sgRNA was obtained by annealing for 5 min at 95°C equal volumes of 100μM specific Alt-R® crRNAs (IDT, Cat# sequence: AGCCAATCGTCTGAGGACGG) with 100μM Alt-R® generic tracrRNA (IDT, Cat# 1072532). Cas9 Nuclease Reaction Buffer (NEB Cat# B0386A) was added to obtain a final 45μM sgRNA stock solution. For the generation of the sgRNAs–Cas9 complex, a mix containing 18μM sgRNA and 12μM Cas9 protein (EnGen™ Spy Cas9-NLS S. pyogenes, NEB Cat# M0646T) was incubated for 10 min at room temperature. For mutagenesis, 1 nl of the sgRNA-Cas9 complex was injected into one-cell stage embryos, that were subsequently raised until 48 hpf. Bulk genomic DNA (gDNA) was extracted from 60 injected and 60 non-injected control embryos. gDNA extraction proceeded as follows: pooled samples were incubated for 3 hrs at 55°C in lysis buffer (100mM NaCl, 20mM Tris-HCl pH 8, 25mM EDTA, 0.5% SDS and 2 µg/µl proteinase K), purified using phenol:chloroform. Precipitation was done in 0.1 volume of 3M NaAc and 2.5 volume of 100% ethanol for 20 min at -20°C. Samples were centrifuged for 30 min at 4°C before washing with 70% ethanol and resuspension in water. gDNA was used for PCR, using DNA polymerase Platinum™ SuperFi™ (Invitrogen Cat# 12351010) and the SM31-SM32bis couple of primers (TTTCACTTTCTCTCTGCCTCTTACA; AACTCTGTCCAGATGATTGAGGAGC) flanking the targeted region. PCR products were run on gel electrophoresis before gel extraction of bands of interest (with sizes corresponding to either a wild-type allele or a deleted allele) (Nucleospin gel and PCR clean-up, Macherey-Nagel Cat# 740609.50). Fragments were cloned into blunt-end TOPO vector (Invitrogen Cat# 45024), transformed into E. coli TOP10 competent cells and grown on selective medium. 12 colonies for each PCR product were sent for sequencing. Mutant sequences contained either a 7 nucleotides deletion, or a mix of 1,4 or 7 nucleotides deletions located at the same site (at the end of exon 38, see ***Figure 7 - figure supplement 4A*** for the 7 nucleotides deletion), attesting of the proper functioning of our guide.

894 A stable homogeneous mutant line was generated by injecting the sgRNA:Cas9 complex into
895 one-cell stage *Tg(kdrl:Gal4;UAS:RFP)* embryos similarly to what was described above. 100
896 embryos were raised until adulthood. Adult founders were identified by crossing adult F0 with
897 AB fishes, and single embryo genotyping was performed on their progeny (10 embryos per
898 adult fish). Briefly, single embryos were incubated in 40*µ*l 25mM NaOH 0.2mM EDTA and
899 heated for 10 min at 95°C, before cooling for 10 min at 4°C and addition of 40*µ*l 40mM Tris-
900 HCl pH5 to stop the reaction. PCR was performed using 5*µ*l of template and specific primers
901 (couple SM31-SM34 –TTTCACTTTCTCTCTGCCTCTTACA;
902 ATAAATGAAGCCCCACCTCCGTCC – for wild-type (WT) allele and couple SM31-SM40 –
903 TTTCACTTTCTCTCTGCCTCTTACA; ATGAAGCCCCACCTCAGACGATTGGC– for mutant
904 allele). Presence of WT or mutant allele for each single embryo was assessed by the
905 presence/absence of amplification band on gel electrophoresis. Four F0 founders were
906 isolated, that had a transmission rate in the germline ranging from 20% to 80%. Progeny of the
907 F0 founders and subsequent generations were raised separately until adulthood, and
908 genotyped. After complete anesthesia (in fish water supplemented with 160*µ*g/ml tricaine
909 methanesulfonate), a small tissue sample was collected from the caudal fin, placed into DNA
910 extraction buffer (10mM Tris pH8.2, 10mM EDTA, 200mMNaCl, 0.5% SDS, 200*µ*g/ml
911 proteinase K) and incubated 3 hrs at 50°C. DNA precipitation and resuspension was performed
912 as described above. 7*µ*L gDNA was used as template for PCR amplification using the primer
913 couple SM31-SM32bis. Sequenced PCR products showed that all founders harbored the same
914 7 nucleotides deletion (see ***Figure 7 - figure supplement 4A***). All experiments relative to
915 ***Figure 7*** *and* ***Figure 8*** were performed using the progenies of one heterozygous mutant F3
916 couple. For these experiments, genotyping on single embryos was performed on gDNA as
917 mentioned above. Only WT homozygous and mutant homozygous embryos were kept for
918 analysis.

919 *Alternative Cpf1 approach*

As an alternative approach to the CRISPR/Cas9 deletion, we attempted to generate a second mutant line, using to CRISPR/Cpf1(Cas12a) system to delete a 315 nucleotides region encompassing exon 38 (with specific guides located in the introns before and after exon 38). The sequence of guides that have been tested are: TATCACACACACATCACCTTCTA and TTTCTCAGCGCTCCTGACAGATG. However, due to the structure of the intronic regions (repeat rich) and the necessary presence of specific PAM sequence, we only generated off-target deletions of intronic regions, without deletions of exon 38, leading us to focus on the CRISPR/Cas9 approach.

Morpholinos and injections

Morpholinos were obtained from GeneTools (see Key Resources Table for sequences). The *sih* Tnnt2 translation start codon and flanking 5-prime sequence MO (Sehnert et al. 2002) as well as the ArhGEF11 exon 38 splice blocking MO (overlapping the exon 38/intron 38-39 boundary) were resuspended in ddH2O to obtain stock solutions at 2mM and 1mM, respectively. The *sih* MO (1.5ng) and ArhGEF11 exon 38 MO (3ng) were injected into 1-cell stage zebrafish embryos, after dilution in ddH2O. For *sih* morphants, embryos that were used in the experiments were checked for absence of heart beating 24 hrs after injection as well as before being used for dissection and RNA extractions at the 30-32 and 48-50 hpf time-windows. For measuring the efficiency of the ArhGEF11 exon 38 MO, total RNA was extracted from pools of injected and control embryos followed by mRNA reverse transcription. PCR on cDNA flanking the exon 38 was performed using DNA polymerase Platinum™ SuperFi™ (Invitrogen Cat# 12351010) and analyzed on gel electrophoresis before extraction, cloning and sequencing to verify the absence of the DNA sequence encoded by exon 38 (see ***Figure 7 - figure supplement 4A***).

Whole mount in situ hybridization

For the sequence of all the primers used to amplify probes, see the Key Resources Table. The probes for WISH concern Pard3ab, Pard3bb (***Figure 3***) and PDZ-RhoGEFs (***Figure 7 – figure supplement 2***).

Whole-mount chromogenic in situ hybridization was performed as described in Lancino et al 2018. Probes were synthetized using the manufacturer recommendation (T7 RNA polymerase, Promega, Cat# P2075, DIG-nucleotides, Jena Bioscence, Cat# NU-803-DIGX).

For Pard3ab (GenBank: AY524776.2), a probe of 717bp (nucleotides 1258-1974) encompassing the nucleotide sequence starting in the 3-prime of the sequence encoding for PDZ1 and ending between PDZ2 and PDZ3 was amplified with the couple of primers pard3ab_WISH_Nter_fw and pard3ab_WISH_Nter_T7_rev. For Pard3bb (NCBI Reference sequence: XM_021478865.1), a probe of 747bp (nucleotides 468-1214) encompassing the nucleotide sequence starting in the 5-prime of the sequence encoding for the N-ter of the protein and ending at the 3-prime of PDZ1 was amplified with the couple of primers pard3bb_WISH_Nter_fw and pard3bb_WISH_Nter_T7_rev (for the position of the primers respectively to the 2 pard3 proteins sequences and domains, see Figure 3B).

Images were captured with the Zeiss Axio ZOOM V16 microscope with the Zen Pro2 software, with a brightfield transmitted light optics. Post-processing steps were performed using the Extended-Depth Focus method to combine in focus regions from multiple z-planes and convert into in a transmitted light z-stack to generate a unique in-focus image.

Immunofluorescence detection of the HA-tagged dt-runx1 deletion mutant

Whole mount immunostaining was performed on hand-dechorionated 48 hpf *Tg(dt-runx1)* embryos to assess the localization of the 2XHA-tagged dt-runx1 protein in aortic cells. Briefly, embryos were fixed in 4% methanol free PFA (Polysciences Cat# 040181) for 3 hrs at room temperature (RT) and washed in PBS/0.1% tween20 (PBT). Embryos were treated in successive baths of milliQ water supplemented with 0.1% tween20, then in cold acetone for 10 min at -20°C and again in milliQ water plus 0.1% tween20. They were then washed in 1X

HBSS (Invitrogen Cat# 14025), and permeabilized for 45 min at RT in 1X HBSS, 0.1% tween20, 5mM CaCl2 and 0.1mg/ml collagenase (Sigma-Aldrich Cat# C9891). Embryos were then rinsed in PBSDT and incubated in blocking solution 1× sheep serum (SS, Sigma Cat# S2263) for at least 4 hrs at RT. They were then incubated overnight at 4°C with primary antibodies in blocking solution: rabbit anti-GFP (MBL Cat# 598; 1/300) and mouse anti-HA (Sigma, Cat# 12ca5; 1/50). On the next day, embryos were washed several times in PBSDT and endogenous peroxidase activity was inactivated by treatment with 6%H2O2 (Sigma-Aldrich, Cat# H1009) for 1 hr at 4°C. Embryos were then incubated in the NGS for at least 4 hrs and incubated overnight at 4°C with secondary antibodies: goat anti-rabbit Alexa Fluor 488 (Invitrogen Cat# A11070; 1/400) and goat anti-mouse HRP-conjugated (Thermo Fisher Scientific Cat# G-21040; 1/300). Finally, embryos were rinsed several times first in PBSDT and after in PBT before HRP fluorescent revelation. Embryos were incubated for 45 min at RT in the dark in imidazole buffer (0.1 M imidazole (Sigma-Aldrich, Cat# I5513) in PBT supplemented with 1% H2O2) with Cy3 Tyramide Reagent (Cy3 NHS sigma Cat# PA13101, tyramide sigma Cat# T-2879, dimethyl formamide sigma Cat# T-8654 and triethylamine sigma Cat# T-0886). Final washes in PBT and in 6% H2O2 for POD inactivation were performed before embryos were mounted in low-melting agarose in 1X PBT for fluorescence confocal imaging.

Quantitative real-time PCR

Preparation of samples

To determine the impact of runx1 interference and blood flow on pard3 family genes and splice variants expression, total RNA from dissected trunk regions was extracted (as described previously) from 30-32 hpf and 48-50 hpf embryos from either incross of the Tg(kdrl:dt-runx1(eGFP)) fish line, outcross of the Tg(kdrl:dt-runx1(eGFP)) and Tg(kdrl:gal4;UAS:RFP) fish lines - with eGFP positive embryos as the interfering condition and eGFP negative embryos as sibling controls -, or Tg(kdrl:gal4;UAS:RFP) embryos injected at the single cell stage with sih morpholino. Analysis was carried on 3 biological replicates.

Technical procedure

For the sequence of all the designed qRT-PCR primers, see the Key Resources Table.

qRT-PCR was performed using Takyon Rox SYBR 2x Master mix blue dTTP kit (Eurogentec Cat# UF-RSMT-B0701), with starting concentrations of template of around 10ng/µl and primer concentrations of 0.5µM, on a QuantStudio3 system (Applied Biosystems). Each reaction was performed in technical triplicates and in at least 3 biological replicates. Ct was determined automatically by the QUANTSTUDIO™ DESIGN & ANALYSIS 2 software on the Thermofisher cloud and exported to be analyzed manually. Standard deviation was calculated within the technical triplicates, and when superior to 0.3, obvious outliers were removed (Dixon's Q test). The delta-delta-Ct method (double normalization to endogenous control — zebrafish elongation factor ef1α — and to control sample) was used to compare gene expression in control and altered conditions.

In vivo confocal imaging

Embryos, dechorionated manually, were anesthetized using tricaine (Sigma Aldrich, Cat# A5040). They were then embedded on the side position in 1% low melting agarose (Promega, Cat# V2111) in a glass bottom 60µ-Dish (35mm high; Ibidi, Cat# 81156). To avoid movements and pigmentation during image acquisitions, 1x tricaine /1x PTU Volvic water was incorporated to the low melting agarose and, after solidification, 1ml of 1x tricaine /1x PTU Volvic water was added before sealing the dish.

Embryos were imaged with 2 confocal microscope systems. For the results presented Figure 1, z-stacks and time-lapse sequences were obtained using a Leica TCS SP8 inverted confocal microscope as described in Lancino et al 2018.

For all the other confocal microscopy results, embryos were imaged using an Andor (Oxford Instruments) spinning disk confocal system (CSU-W1 Dual camera with 50µm Disk pattern and single laser input (445/488/561/642nm), LD Quad 405/488/561/640 and Tripl 445/561/640 dichroic mirrors), equipped with a Leica DMi8 fluorescence inverted microscope and CMOS

cameras (Orca Flash 4.0 V2+ (Hamamatsu)). Imaging was performed using a 40x water immersion objective (HC PL APO 40x/1.10 Water CORR CS2), a LEDs light source (CoolLED pE-4000 16 wavelength LED fluorescence system), and the acquisitions were piloted with the support of the MetaMorph software.

Morphological and morphometric analysis of aortic and hemogenic cells

For the morphometric analysis of the aorta and aortic cells, large z-stack of 48-55 hpf Tg(kdrl:eGFP-JAM3b; kdrl:nls-mKate2) or Tg(kdrl:eGFP-JAM2a; kdrl:nls-mKate2) encompassing the whole aortic depth were acquired with optimal z-resolution (0.3μm z-step). For each embryo, 3 contiguous z-stacks of 330μm width were acquired, allowing us to image the entirety of the AGM region, from the anterior to the posterior end of the elongated yolk.

Samples

For ArhGEF11 splicing morpholino experiment, 3 splicing morpholino injected embryos and 2 control non injected siblings were kept for the analysis.

For ArhGEF11 CRISPR Cter deletion and when performing the experiments, imaging was done, for putative mutants, on embryos that had shown a delay in initiation of circulation at 24 hpf, regained circulation at 48 hpf albeit with a clearly visible oedema in the cardiac region (non-altered embryos were kept as sibling controls). All imaged embryos whose signal allowed us to generate segmentable 2D-cartography from the whole length of the aorta were kept and processed further for genotyping. Genotyping confirmed that the circulation problems at 24 hpf and the remaining oedema at 48 hpf corresponded to embryos bearing the mutation.

For CRISPR mutant phenotype analyses, 2 mutant embryos and 2 wild type siblings were kept, after genotyping.

Image analysis

The following image analysis was performed on Icy software.

For each segment, we generated a 2D-cartography of the eGFP-Jam signals at intercellular contacts of aortic cells, using the Tubeskinner plugin, according to the protocol described in

Lancino et al 2018. Briefly, the aorta was rotated to face the lumen, a circular ROI fitting the interior of the aorta was initialized by the experimenter on the first plane, and for each plane sequentially, the algorithm will more accurately fit the ROI to the aortic perimeter and collect the fluorescence intensity all along its longitudinal axis. The collected intensity was then projected on a 2D-plane, where the Y-axis of the 2D-cartography corresponds to the perimeter of the aorta, and the X-axis corresponds to the X-axis of the original z-stack.

Before further processing, a metadata table recapitulating the dates and conditions of experiments for each embryo was generated, and a random label was assigned to rename each acquisition. This allowed for the later part of the analysis, that involves semi-automated segmentation and classification by the user, to be blind and avoid potential bias.

Each 2D-cartography was then manually pre-segmented using the ROI Polygon tool to draw the contour of each aortic cell, using the original 3D z-stack as reference. Due to technical limitation (decreased fluorescence signal collection on the farthest lateral side of the aorta), only about 2/3 of the 2D-cartographies could be segmented (comprising the floor, the right lateral side of the aorta and the roof). The manual segmentation was then improved using the "Active Contour" plugin, that improved the fit of the cellular contour to the fluorescence signal and slightly dilated the cell contours until the ROIs formed a joint paving. All morphometric descriptors were extracted for each cell. The number of neighbours was automatically generated for each cell by counting the number of touching adjacent ROIs.

Additionally, cells were manually classified into cell types according to morphometric parameters using as reference the original 3D z-stack and in particular the nls-mKate2 nuclear signal. EHT-undergoing cells were positioned on the floor of the aorta, have reduce antero-posterior axis length, luminal membrane inward bending for EHT pol+ cells and luminal membrane outward bending for EHT pol- cells, and a thickened nucleus. Hemogenic cells whose criteria were established in Lancino et al 2018 (elongated in the antero-posterior axis, with lateral membranes not trespassing the equatorial plane of the aortic wall), are positioned on the floor of the aorta, systematically have a reduced width perpendicular to the blood flow

and, importantly, a thickened nucleus that protrudes out of the aortic plane. Finally, endothelial cells have a flattened nucleus positioned high on the lateral side or on the roof of the aorta.

Measurement of the aortic perimeter

An accurate measurement of the aortic perimeter was obtained using the z-stack generated for the aortic cells' morphometric analysis. Briefly, the z-stack was rotated to face the lumen of the aorta and a ROI fitting the aortic perimeter was drawn by the user and optimized by the "Cell Contour" plugin. The length of the perimeter was then extracted from the ROI statistics.

Fluorescence Recovery After Photobleaching (FRAP) measurements and analysis

Measurement of junctional turn-over was performed on 48-55 hpf *Tg(kdrl:eGFP-JAM3b; kdrl:nls-mKate2)* embryos using a Nikon Ti2e spinning disk microscope equipped with a sCMOS camera (Photometrics, Prime 95B, pixel size 11μm, 1200×1200 pixels, QE 95%) and a 40x water objective (Numerical Aperture 1.15, Working Distance 0.6mm, xy pixel size of 0.27μm). Embryos were mounted as previously described.

Samples

For ArhGEF11 splicing morpholino phenotypic analysis, 10 different embryos (injected with the splicing morpholino) obtained from 3 separate experiments and 30 control embryos (non-injected siblings or control morpholino injected siblings) obtained from 6 separate experiments were analyzed.

For EHT analysis, 16 embryos over 4 separate experiments were analyzed.

For ArhGEF11 CRISPR/Cas9 Cter deletion phenotypic analysis, 8 mutant embryos and 12 wild type siblings over 3 separate experiments were analyzed.

Overall, the exact number of interfaces analyzed is written on each figure panel.

Acquisitions

For each acquisition, a wide two channels z-stack of the aorta was generated to capture the whole aortic volume and generate a 2D-cartography of the aortic environment (Icy, plugin

Tubeskinner). This 2D-cartography of the cellular contours and the z-stack with the cellular contours and nuclei were used jointly to identify un-ambiguously cellular and junctional types and define one or multiple single point regions of interest (ROIs) for subsequent bleaching and fluorescence recovery measurement.

The sequence of acquisitions before/after bleach focused only on the eGFP-Jam3b signal to speed up the acquisition and improve the temporal resolution. The 5 steps of the acquisition can be recapitulated as follows and we obtained/performed: (1) a single z-stack of 20μm centered on the plane of focus, (2) a 30 sec time-lapse acquisition on the plane of focus to measure average pre-bleach intensity with an image every second, (3) a high intensity stimulation of the ROIs (25% 300ms 488 FRAP laser exposure, leading to the bleaching of the Jam3b-eGFP signal), (4) a 3 min time-lapse acquisition on the plane of focus to measure fast post-bleach recovery with an image every second, and (5) a 7 min time lapse acquisition of 8μm z-stack centered around focus plane with a 20 sec time interval to measure slow post-bleach recovery. Each step was save separately as .nd2 files.

Signal quantification and recovery analysis

File were converted from .nd2 to .tiff using FIJI batch converter, scale factor 1.00, bilinear interpolation, no average when downsizing, images read using bioformat.

To collect fluorescence intensity, ROIs for each stimulation point was manually drawn using Fiji and named with an individual label using Fiji ROI manager. A metadata table was manually curated with all information for each ROI (junction type, condition, date of experiment, embryo number). An additional ROI was created to collect background intensity for subsequent corrections. Acquisitions with clear embryo movement or drifting were either completely removed from the dataset (~5% of the acquisitions) or only kept for early recovery analysis (see below) if the drift only occurred in the last step (fifth) of the acquisition.

Fluorescence intensity for each ROI was collected and saved automatically as a .csv file for each acquisition using a homemade Fiji macro.

All further analysis were performed using R for automatization.

Briefly, for each ROI: the fluorescent signal was normalized to the background signal ($I_{background\ normalized} = I_{roi} - I_{background}$), then normalized to mean intensity pre-bleach ($I_{normalized} = I_{background\ normalized\ ROI\ post\text{-}bleach} / I_{background\ normalized\ ROI\ pre\text{-}bleach}$), and finally scaled ($I_{full\ scaled\ normalized} = (I_{normalized} - \min(I_{normalized}))/ (1 - \min(I_{normalized}))$.

A single exponential equation was used to fit the data using the nls:multistart package for parameter optimization:

$F(t) = A*(1-e^{-t*\tau})$

With A the maximum amplitude of the curve, t the time, and τ a constant defining the growth rate of the curve.

The fitted curve allowed to extract quantitative information describing the recovery of each type of junction in different conditions: the mobile fraction of the bleached pool (corresponding to A, the amplitude of recovery) and the time of half recovery, related to the speed of recovery, that can be extracted from τ:

$T_{half\text{-}recovery} = \ln(0.5)/(-\tau)$

A more precise description of the recovery speed was extracted from the observation of the early time period (until 30s post bleach), were the fluorescence intensity increases uniformly. A first-degree polynomial equation was fitted to the data (using lm() function from the stats package), and the coefficient corresponding to the slope of the fitted curve was used as a metric for speed of fluorescence recovery.

Statistical analysis

Statistical tests used are described for each figure panel in the legend. Since our samples are usually small, the test used is an unpaired two samples non-parametrical Wilcoxon mean comparison test, without a priori knowledge on sample normal distribution or homoscedasticity.

Data and software availability

All graphics and plots were generated using RStudio and packages including: ggplot2 (Wickham 2016), readr (Wickham, Hester, and Bryan 2022), dplyr (Wickham et al. 2023), stringr (Wickham 2022), ggstatsplot (Patil 2022), ggpubr (Kassambara 2020), wesanderson (Ram and Wickham 2018), cowplot(Wilke 2020), ggsci (Xiao 2018), ggbeeswarm (Clarke and Sherrill-Mix 2017), viridis (Garnier 2021), DT (Xie, Cheng, and Tan 2022), SciViews (Grosjean 2019), nls.multstart (Padfield and Matheson 2020), matrixStats (Bengtsson 2022).

Acknowledgments

We wish to warmly thank Philippe Herbomel for his encouragements and for ensuring the funding of this study.

We thank our fish facility members Y. Rolin and K. Sebastien for their daily help, R. Patient (University of Oxford) for the Hsp70 promoter. This work was supported by Institut Pasteur, CNRS, grants to P. Herbomel from the Fondation pour la Recherche Médicale (#DEQ20160334881), the Fondation ARC pour la Recherche sur le Cancer, and the Agence Nationale de la Recherche Laboratoire d'Excellence Revive (Investissement d'Avenir, ANR-10-LABX-73), and a grant to AS from the Institut Pasteur (PTR 439-2021). LT was recipient of a PhD fellowship from the Collège Doctoral, Sorbonne Université, and from the Labex Revive (ANR-10-LABX-73).

Authors contributions

LT designed, performed and analyzed experiments, and wrote the Method section and the Figure legends. SM designed and conducted experiments. CV conducted experiments. AS conceived the project, designed, performed and analyzed experiments, wrote the manuscript with input from LT, and obtained funding.

Declaration of interests

1187 The authors declare no competing interests.

Figure legends

Figure 1: Tracing the evolution of the luminal membrane using the polarity marker Podocalyxin points at the biological significance of apicobasal polarity establishment in EHT cell emergence complexity. A, cartoons depicting the early and late steps of EHT cells emerging from the aortic floor (steps 1 and 2, as previously described in the zebrafish embryo, see (Kissa and Herbomel 2010; Lancino et al. 2018)) and with hypothetical evolution of the luminal membrane (in green) before (3 and 4) and after the release (2', the cell detaches from the endothelial layer via junction downregulation leading to exposure of the luminal membrane with le extracellular milieu; 3', the luminal membrane is consumed via endocytic recycling (E) and/or lysosomal degradation (Lys) prior to detachment; 4', the luminal membrane in 4 is released inside the cell (twisted arrow) before detachment. Grey area= nucleus. **B**, PodocalyxinL2 (Podxl2) construct designed to establish transgenic fish lines. Cartoons representing full length (top drawing) and deleted Podxl2 (amino-acid sequence 341-587) in which the mucin domain (serine/threonine-rich O-glycosylation domain) is replaced by either eGFP or mKate2. The tetracystein-containing globular domain (subjected to N-glycosylation) was kept as favoring apical membrane retention. TMD, transmembrane domain; DTHL, C-terminal peptidic motif involved in partnership with PDZ domain containing proteins. **C-D**, EHT performing cells visualized using *Tg(Kdrl:Gal4;UAS:RFP;4xNR:eGFP-Podxl2)* embryos and time-lapse sequences initiated at 55 hpf obtained with spinning disk confocal microscopy (imaging was performed at the boundary between the most downstream region of the AGM and the beginning of the caudal hematopoietic tissue). Top grey panels show the green, eGFP channels for eGFP-Podxl2 only. Bottom panels show the merge between green and red (soluble RFP, in magenta) channels. Bars: 8μm. **C**, single plane images of 2 EHT pol+ cells extracted from a time-lapse sequence at t = 0 and t = 45 min, with the right cell (eht cell 2) more advanced in the emergence process than the left one (eht cell1). Note the enrichment

of eGFP-Podxl2 at the luminal membrane (surrounding the cavity labelled with an asterisk) in comparison to the basal membrane (white arrow). Note also the evolution of the luminal membranes with time, with the aortic and eht cell 1 lumens still connecting at t = 0 (green arrow), the apparent fragmentation of the cytosolic vacuole (2 asterisks for eht cell 1 at t = 45 min) and the compaction of Podxl2-containing membranes for eht cell 2 at t = 45 min. More details on the evolution of the connection between the aortic/eht cell lumens are shown in ***Figure 1 – figure supplement 1A***. **D**, single plane images of 2 EHT pol- cells extracted from a time-lapse sequence at t = 30 min and t = 210 min (see ***Figure 1 – video 3*** for the full-time lapse sequence), with the right cell (eht cell 2) slightly more advanced in the emergence than the left one (eht cell 1, with the latest attachment point between the emerging cell and the aortic floor (pink arrow)). Note, in comparison with the cells in panel C, the ovoid shapes of cells, the absence of enrichment of eGFP-Podxl2 at luminal membranes (green arrows) and the accumulation of eGFP-Podxl2 at basal membrane rounded protrusions (white arrows).

Figure 2: Immature HE is not polarized and controls membrane delivery of intra-cytosolic vesicular pools. **A**, *Tg(Kdrl:Gal4;UAS:RFP;4xNR:eGFP-Podxl2)* embryo imaged using spinning disk confocal microscopy. Black and white images show eGFP-Podxl2 only. Images were obtained from a time-lapse sequence (initiated at 35 hpf) lasting for 435 min (7.25 hrs), with intervals of 15 min between each z-stack. Example of an HE cell with equal partitioning of eGFP-podxl2 between luminal and abluminal membranes (at t = 0 min), with eGFP-podxl2 containing intra-cytosolic vesicles (one labelled with a green asterisk) and undergoing mitosis at t = 30 min (HE cell 1' and HE cell 1'' are daughter cells). Note the inheritance of the largest micropinocytic-like vacuole by HE cell 1' and its maintenance through time until EHT emergence initiation at t = 180 min (green asterisk in 1.5x magnified areas at t = 60 and 90 min). At t = 360 min (green box) both fluorescence channels are shown; bottom panel: green (eGFP-Podxl2), magenta (soluble RFP). The magenta arrow points at the basal

side of the EHT pol + cell that does not contain any detectable eGFP-Podxl2; on the contrary, eGFP-Podxl2 is enriched at the luminal/apical membrane (note that exocytosis of the large vacuolar structure may have contributed to increase the surface of the apical/luminal membrane (the green asterisk labels the lumen of the EHT pol + cell). The green arrow points at the abluminal membrane of the EHT cell derived from HE cell 1'' and that contains eGFP-Podxl2 (with no evidence of a significant expansion of a luminal/apical membrane); this indicates that this cell is more likely to be an EHT pol- cell that does not sort the vesicular cargo to the luminal/apical membrane. Bar = 10μm. **B**, model summarizing the evolution of HE cells that involves the tuning of apicobasal polarity thus leading to cells competent for giving birth to either EHT pol+ or EHT pol- cells (including the oriented release of large vesicular macropinocytic-like vacuoles preferentially toward the luminal membrane of future EHT pol + cells). The polarity status of the HE is proposed to evolve throughout the entire time window of the EHT, leading to asynchrony in its ability to give birth to EHT cells (emergence of EHT pol+ and EHT pol- cells are both observed until 72 hpf, see main text).

Figure 3: Molecular variants and deletion mutants to investigate the control of apicobasal polarity during the 30-32 and 48-50 hpf time-windows. A, Expression of Pard3ab and bb isoforms in the zebrafish embryo at 35 hpf using whole mount in situ hybridization (WISH). Expression in the dorsal aorta, in the trunk region (delimited areas), is marked by arrowheads as well as in the veinous plexus of the caudal hematopoietic tissue, in the tail. ey = elongated yolk. **B,** Pard3ab and bb zebrafish isoforms and natural variants to investigate the regulation of apicobasal polarity during the 30-32 hpf and 48-50 hpf time windows. The cartoons show the 3 sequential PDZ domains (PDZ1-3), the CR1 and CR3 conserved regions involved in oligomerization and atypical protein kinase C (aPKC) binding, respectively. For each isoform, the variants that we have cloned either contain or exclude (+/- exon) the peptides encoded by specific exons (see ***Materials and Methods***); of relevance for our purpose (investigating the expression of potential interfering isoforms), we focused on

isoforms deleted from exons encoding for part of the PDZ domains (covering the amino-terminus of Pard3ab PDZ2 and the carboxy-terminus of Pard3bb PDZ3). Note that deletion of exon 10 of Pard3ab triggers a frame shift in the ORF leading to a complete deletion of PDZ2 and to a premature stop codon upstream of PDZ3. In this case, this should lead to the synthesis of a deleted proteins with major loss of function or, alternatively, the degradation of the mRNA via alternative splicing activated non-sense mediated decay (NMD, as exemplified in the EMT process, see (Pradella et al. 2017)). The position of the primers used to amplify cDNA fragments is depicted (fw (forward), rev (reverse), magenta: primers for WISH probes; see ***Materials and Methods***). Note that, in this study and for the PDZ1 domain of Pard3ab, we did not address the expression levels of the isoforms containing or not the insert encoding for the YVFR peptide. **C**, **left:** cartoons representing the zebrafish full-length runx1a amino-acid sequence and the dt-runx1 mutant deleted from the trans-activation domain and of the C-terminus (note that the construct encodes for a C-terminal fusion with eGFP that is released upon expression via a cleavable T2A peptide (introduced between the 2xHA tag and the N-terminus of eGFP, to prevent from potential steric hindrance). nls, nuclear localization signal. **Right:** anti-HA tag immunofluorescence obtained after z-projection of the dorsal aorta of a 50 hpf *Tg(dt-runx1)* embryo. Note the localization of the 2xHA-tagged dt-runx1 protein in nuclei (some of them are pointed by red arrowheads) and of eGFP in nuclei and the cytosol of aortic cells. Bar: 25*μ*m.

Figure 4: Pard3 isoforms and variants are differentially regulated during the 30-32 and 48-50 hpf time-windows. qRT-PCR analysis of gene products of interest in trunks isolated from 30-32 hpf and 48-50 hpf embryos. Trunks were collected from eGFP positive or eGFP negative incrosses of heterozygous *Tg(dt-runx1) fishes* (dt-runx1 incross and sibling controls, respectively) and from *Tg(kdrl:Gal4;UAS:RFP)* embryos injected or not at the single cell stage with the *sih* morpholino (morpholino sih). Graphs show the measured mean fold changes relative to the expression of ef1α and to the expression in control embryos. Statistical tests:

two sided unpaired two samples Wilcoxon test, with p-values of significant differences. **A,** gene expression levels of (**left)** the 3 isoforms of Pard3 proteins (Pard3ab, bb, b and ba, see ***Materials and Methods*** for accession numbers and primers) and (**right**) the hematopoietic marker cmyb and the polarity protein Scrib (for the cellular basolateral domain establishment/maintenance). **B,** Pard3ab and Pard3bb gene expression levels for dt-runx1 mutants (red boxes) and for the *sih* morpholino (yellow boxes), all relative to control conditions. **C,** Pard3ab +/- PDZ2 (top 2 panels) and Pard3bb +/- PDZ3 (bottom 2 panels) gene splicing variants expression levels for dt-runx1 mutants (left panels, red boxes) or the *sih* morpholino (right panels, yellow boxes), all relative to control conditions.

Figure 5: eGFP-Jam3b localization is reinforced at antero-posterior sites of the endothelial/EHT interface and at tri-cellular junctions. A, cartoons representing homodimers of full-length JAMs with the C-terminal cytosolic part interacting with Pard3 (JAMs interact with the first PDZ domain of Pard3) as well as the constructs generated in this study and containing eGFP inserted between the Immunoglobulin-like (Ig) domains and the trans-membrane region (TMD). The constructs were obtained for zebrafish JAM2a and JAM3b. **B, C**, 52 hpf *Tg(kdrl:eGFP-Jam3b; kdrl:nls-mKate2)* embryos were imaged in the trunk region (AGM) using spinning disc confocal microscopy. The panels are either maximum z-projections (top two) or single plane z-sections (bottom two, focusing on the aortic floor) of aortic segments, with either the merged nls-mkate2 and eGFP-Jam3b fluorescence signals (magenta and green) or the eGFP-Jam3b signal only (black and white images). Bottom of the Figure: 2D-cartographies obtained after deploying aortic cylinders and showing the eGFP-Jam3b signals only. **B**, example of an EHT pol+ cell (cell 1, white arrows point at reinforcement of signal at antero-posterior junctions). On the 2D cartography, cell 1 (red) is contacting endothelial cells 2 and 3; note the reinforcement of eGFP-Jam3b signals along antero-posterior membrane interfaces perpendicular to blood flow (red arrows) as well as at the two tri-cellular junctions visible between cells 1, 2 and 3 (black arrows). **C**, example of two EHT

pol- cells (cells 1 and 2, white arrows point at reinforcement of signal at antero-posterior junctions). On the 2D cartography, cells 1 and 2 (red) are contacting endothelial cells 3, 4, 6 and 3, 6 respectively; note the reinforcement of eGFP-Jam3b signals along antero-posterior membrane interfaces perpendicular to blood flow (red arrows) and endothelial cell 6 that has intercalated between endothelial cell 7 and EHT pol- cell 2 (blue arrow). In right margins, magenta and green arrowheads designate the aortic floor and roof, respectively. Bars = 10μm.

Figure 6: Junctional recycling at tri-cellular contacts is differentially controlled between the two EHT types. 48-55 hpf *Tg(kdrl:eGFP-Jam3b; kdrl:nls-mKate2)* embryos were imaged using spinning disc confocal microscopy and illuminated for Fluorescence Recovery After Photobleaching (FRAP) in the trunk region (AGM, Aorta Gonad Mesonephros). **A, B**, panels are either maximum z-projections (top left) or single plane z-sections (bottom left and top right, focusing on the aortic floor) of aortic segments, with either the merged nls-mkate2 and eGFP-Jam3b fluorescence signals (magenta and green) or the eGFP-Jam3b signal only (black and white images). White arrows point at reinforcement of signal at antero-posterior junctional pools of an EHT pol+ cell (**A**) or of an EHT pol- cell (**B**), both marked by asterisks. Bottom right: 2D-cartographies obtained after deploying aortic cylinders and showing the eGFP-Jam3b signals only. Black arrows point at antero-posterior junctional pools, in particular at tri-junctional regions that exhibit increase in signal density (well visible in **A,** black arrows). 2 and 3 endothelial cells are contacting the EHT pol+ cell (**A**) and the EHT pol- cell (**B**), respectively. In right margins, magenta and green arrowheads designate the aortic floor and roof, respectively. Bars = 20μm. **C - G,** FRAP analyses. EGFP-Jam3b junctional pools corresponding to the brightest spots inside junctional regions of interest were bleached for FRAP measurements (these high intensity pools were localized at the level of bi- and tri-junctions for endothelial cells (EC) and in tri-junctional regions for EHT pol+ and EHT pol- cells; all these junctional pools were systematically visualized by deploying each aortic segment before bleaching as shown in the 2D-cartographies in A and B as well as in ***Figure 6 – figure***

supplement 1, see also ***Materials and Methods***). FRAP analysis concerned 3 types of junctional interfaces: between endothelial cells (EC – EC, black and grey), EHT pol- and endothelial cells (pol- – EC, brown), EHT pol+ and endothelial cells (pol+ – EC, blue). **C, D**, evolution of mean fluorescence intensity for each type of junctional interface over time (10 min), after photobleaching (t = 0s). **E**, median maximum amplitude of recovery of all determinations and for each type of junctional interface (maximum of simple exponential fitted curves). **F, G**, early fluorescence recovery. Early evolution (over the first 30s) of the mean fluorescence intensity for each type of junctional interface over time after photobleaching (t = 0s). **F**, the fitted lines correspond to linear regressions of mean fluorescence intensities. **G**, median values of fluorescence recovery slopes (linear regressions) of all determinations and for each type of junctional interface. Statistical tests: two sided unpaired two samples Wilcoxon test.

Figure 7: Interfering with ArhGEF11/PDZ-RhoGEF function leads to the accumulation of hemogenic cells and impairs EHT progression. A-C, numeration and morphometric analyses of aorta and cell types for *Tg(kdrl:eGFP-Jam3b; kdrl:nls-mKate2)* ArhGEF11 exon 38 splicing morpholino-injected and control embryos (**A**), or for *(Kdrl:eGFP-Jam3b; kdrl:*ArhGEF11$^{CRISPR\text{-}Cterdel+/+}$) homozygous ArhGEF11 C-ter deletion mutants and control siblings (**B**). 48-55 hpf embryos were imaged using spinning disk confocal microscopy. **Aa, Bb**, 2D-cartographies obtained after deploying aortic cylinders and showing the eGFP-Jam3b signals only with cell contours delineated either in blue (endothelial cells), yellow (hemogenic cells, see ***Materials and Methods*** for their morphological definition), red (morphologically characterized EHT cells, for controls), and small cells delineated by cyan boxes (morphologically uncharacterized EHT cells and putative post-mitotic cells remaining as pairs, included in the numeration as hemogenic cells). Cellular contours have been semi-automatically segmented along the cellular interfaces labelled with eGFP-Jam3b (see

Materials and Methods). Scale bars: 10μm. **Aa', Bb'**, **left:** numeration of endothelial, hemogenic and EHT-undergoing cells according to the position of their geometrical center (either on the aortic floor, or on the roof, or on the lateral side), for each condition; **right**: number of endothelial, hemogenic and EHT-undergoing cells in each condition calculated from the segmentation of 3 x 2D-projections per embryo and covering the entire aortic regions in the trunk. **Aa'', Bb''**, **left**: length of hemogenic cells (in the longest axis) in function of their orientation (°) relative to the blood flow axis (0 – 180°); **right**: distribution of the orientation of hemogenic cells relative to the blood flow axis, displayed as a mean distribution of cells per embryo. **Aa''', Bb'''**, hemogenic cell elongation factors in arbitrary Units (scale factor given by the ratio between the first- and the second-best fitting ellipse diameters, the minimum value being 1 for a non-elongated object) represented as boxplot distribution of all segmented cells (**left**) or as the distribution of cell elongation factor per embryo (**right**), for controls and for interfering conditions as indicated. **Aa'''', Bb''''**, hemogenic cell area represented as boxplot distribution of all segmented cells (**left**) or as the distribution of cell area per embryo (**right**), for controls and for interfering conditions as indicated. **C**, aortic perimeter (in μm) for controls and mutant conditions as indicated. Statistical tests: two sided unpaired two samples Wilcoxon test. For the ArhGEF11 exon 38 splicing morpholino condition, analysis was performed on 2 x control (non-injected embryos) and 3 x embryos injected at the one-cell stage; for the CRISPR mutant condition, analysis was performed on 2 x wild-type siblings for control and 2 x homozygous mutant embryos whose DNA mutation was confirmed by sequencing. 3 consecutive aortic segments per embryo were analyzed to cover the whole length of the dorsal aorta, in the trunk region (covering a distance of 990μm per embryo).

Figure 8: Interfering with the function of ArhGEF11/PDZ-RhoGEF suggests an activity at the interface between endothelial and hemogenic cells that relies on restricting the mobility of junctional pools at tri-cellular junctions, with a prominent role of the +exon

38 variant during endothelial cell intercalation. A, 2D-cartography of an aortic segment of a *Tg(kdrl:eGFP-Jam3b; kdrl:nls-mkate2)* embryo injected at the one cell stage with the ArhGEF11 exon 38 splicing morpholino. All the arrows pointing at reinforced junctional contacts between cells were bleached and imaged for FRAP analysis (the bleached areas correspond to the spots of highest intensities in the regions of interest, as visualized at the fluorescent confocal microscope, see ***Materials and Methods***). Black and Magenta arrows point at he-he-ec and he-ec-ec tri-cellular junctions, respectively (he: hemogenic cell; ec: endothelial cell). Green arrows point at he-ec bi-cellular junctions. ec: endothelial cell, he: hemogenic cell. Bar = 20μm. **B, C**, FRAP analysis of bleached eGFP-Jam3b localized in regions of interest in controls (grey) and ArhGEF11 exon 38 splicing morpholino injected embryos (blue) or homozygous ArhGEF11$^{CRISPR\text{-}Cterdel+/+}$ mutants (green). Statistical tests: two sided unpaired two samples Wilcoxon test. Bb, Cc, evolution, after photobleaching (at t=0s), of the mean fluorescence intensity per condition at HE-EC, HE-EC-EC and HE-HE-EC bi- and tri-junctions over time (10 min). Bb', Cc', median values for maximum amplitude of recovery (maximum of simple exponential fitted curves, see ***Materials and Methods***). Bb'', Cc'', early evolution, after photobleaching (at t=0s), of the mean fluorescence intensity per condition over time (for the first 30 seconds). The fitted lines correspond to the linear regression of the mean fluorescence intensities. Bb''', Cc''', median fluorescence recovery slopes (linear regression). **D**, Model (2D deployment of the aortic wall) representing the endothelial/hemogenic dynamic interplay and the proposed function of ArhGEF11 and of its +exon 38 peptide encoding variant at junctional and membrane interfaces. This interplay involves 2 essential dynamic events requiring junctional remodeling: **1** (left cartoon, magenta arrows), the mobility of he-ec-ec tri-junctional contacts accompanying the movement of endothelial cells (ex: for ec1 and ec2) along lateral sides of hemogenic cells which is required to decrease the number of adjoining cells (see Lancino et al. 2018). This takes place contemporarily to - or in alternance with -, the contraction of HE and EHT cells as they are progressing throughout the emergence and reducing contacting membrane surfaces along the longitudinal axis (the reduction in contacting

membrane surfaces also involves membrane retrieval, hypothetically via endocytosis). Our data obtained with the CRISPR deletion mutants (a slight tendency to increase, on average, the turnover and mobile pool of these he-ec-ec junctions) suggest that ArhGEF11, in the wild type condition, should be slowing down the recycling of junctional components at tri-junctions, which hypothetically should contribute to increase adhesion strength. This may be required also to stabilize the junction-cytoskeleton interface involved in controlling the contraction/shrinkage of HE cells along the longitudinal axis, a hypothesis that is compatible with the mutant phenotype observed in this study, i.e the increase in frequency of more elongated HE cells and the decrease in HE cell progression throughout EHT (see ***Figure 7***); **2** (right cartoon, cyan arrow and bottom cartoons a-c), the intercalation of an endothelial cell to isolate 2 adjacent hemogenic cells or 2 daughter cells after mitosis (not depicted). This is mandatory for EHT progression and completion which requires adjoining endothelial cells to protrude membrane extensions that will anastomose to seal the aortic floor (see Lancino et al. 2018). The accumulation of adjoining cells of rather small length and apparently impaired in EHT progression that we describe in ***Figure*** 7 upon MO interference (that may also indicate impairment in abscission completion) suggests that the ArhGEF11 +exon 38 peptide encoding variant is more specifically involved in controlling the remodeling of the he/he interface that leads to endothelial cell intercalation (bottom cartoons, the remodeling of he-he-ec junctions is leading to he-ec-ec junctions and takes place between b and c). The increase in the recycling parameters that we measure in this interfering condition (mobile pool and early speed of recovery) indicates that the activity of ArhGEF11, and in particular of its +exon 38 peptide encoding variant, negatively controls junctional recycling. Hypothetically, the junctional adhesion strengthening triggered by reducing the recycling of junctional components at the he/he interface may be required during the early phase and progression of intercalation to support increase in membrane tension and environmental constraints (intercalation contributes to reducing the length/surface of the he/he membrane interface preceding junctional

1453 remodeling (cartoons b and c); this reducing membrane interface is in addition submitted to

1454 the shear stress imposed by blood flow).

1455

Legends to supplement figures

Figure 1 – figure supplement 1. A, 2 EHT pol+ cells visualized using a *Tg(Kdrl:Gal4;UAS:RFP;4xNR:eGFP-Podxl2)* embryo and time-lapse sequence (initiated at 55 hpf) obtained with spinning disk confocal microscopy. The images are extracted from the same time lapse sequence than the one used for ***Figure 1C***. Green channel (eGFP-Podxl2) only is shown. Green arrows point at the evolution of the connection between the aortic/eht cell lumens at t = 0, 10, 30 min. Asterisks label the lumen delimited by the luminal/apical membranes. Bar = 8μm. **B**, Model summarizing and interpreting the temporal evolution of the luminal/apical membrane (in green, the asterisks mark the lumen of the apparent vacuole-like intracellular membrane structures) after the release of an EHT pol+ cell from the aortic floor. **Step 1**, the pseudo-vacuole filled with fluid and delimited by eGFP-Podxl2 as visualized at t = 65 min in **A** (and also at 45 min in ***Figure 1C***, 2 asterisks) is consumed partly via budding (after sorting of eGFP-Podxl2); these budding profiles can be seen on the left image (pink arrowheads) corresponding, for eht cell 1, to the plane 16 of the time point t = 80 min of the time lapse sequence (see the Z-stack in ***Figure 1 – video 2***). **Step 2**, after sorting and budding, the cell remains with pseudo-endocytic Podxl2 containing membranes and the remaining vacuolar structures filled up with fluid regress, putatively by chasing water as illustrated in **step 3**. **Step 4**, the eht cell remains with pseudo-endocytic Podxl2 containing membranes that label newly born precursors of HSPCs. Note that since the cell remains in contact with the aortic floor while the pseudo-vacuole is regressing, the vacuole-like intracellular membrane proximal to aortic cells may never undergo fission (see ***Figure 1A***, steps 4-4') but gets consumed via budding and flattening upon water chase (steps 1-3 that are similar to ***Figure 1A***, steps 3-3').

Figure 1 – video 1. EHT pol+ cells at early timing. Z-stack (37 planes) corresponding to the time point t = 0 min whose plane 21 is shown ***Figure 1C***.

Figure 1 – video 2. EHT pol+ cells at late timing. Z-stack (37 planes) corresponding to the time point t = 80 min whose planes 16 (for eht cell 1) and 22 (for eht cell 2) are shown ***Figure 1 – figure supplement 1B.***

Figure 1 – video 3. Emergence of EHT pol- cells. Time-lapse sequence using a *Tg(Kdrl:Gal4;UAS:RFP;4xNR:eGFP-Podxl2)* embryo, obtained with spinning disk confocal microscopy (38 timing points, each acquired with 10 min intervals, starting at 55 hpf) and from which the images of the 2 emerging EHT pol- cells shown Figure 1D were extracted.

Figure 2 – figure supplement 1. HE cells are not polarized at 30 hpf. *Tg(Kdrl:Gal4;UAS:RFP;4xNR:eGFP-Podxl2)* 30 hpf embryo imaged using spinning disk confocal microscopy. **Top 2 panels**: green (eGFP-Podxl2) and red (soluble RFP, in magenta) channels. White arrows point at 2 individual EHT cells. Note that HE cell 1 protrudes long filopodia, some of which inside the aortic lumen (live imaging shows that they are moving along the blood flow, data not shown). **Bottom 2 panels**: 1.625X magnification of EHT cell 1 and 2 in top panels. Green channel (eGFP-Podxl2) only. Green arrows point at very large intracellular vesicles, the largest reaching approximately 30μm. Asterisks mark the cytoplasm. Bar: 100μm.

Figure 2 – figure supplement 2. Evolution of non-polarized HE cells throughout emergence. *Tg(Kdrl:Gal4;UAS:RFP;4xNR:eGFP-Podxl2)* embryo imaged using spinning disk confocal microscopy. Images were obtained from discontinuous time-lapse sequences covering a period of 13 hours (from 35 – to – 48 hpf). Successive phases of the evolution of HE cells are visible, from a non-polarized status (with the accumulation of Podxl2-containing intra-cytosolic vesicles as well as cell division) to post-emergence EHT cells remaining beneath the aortic floor. The top panel is a z-projection of 69 consecutive z-sections interspaced by 0.3μm; green (eGFP-Podxl2) and red (soluble RFP, in magenta) channels are

shown; 4 individual HE cells (1 – 4, green arrows)) are marked, with cells 1 and 4 more advanced in the process of emergence. All the other panels are z-sections focused on the aortic floor, allowing visualizing the progression of the EHT, in particular at 35 hpf (t = 0), a timing point at which the separation between the luminal and basal membranes are equally labelled with eGFP-Podxl2, attesting for the absence of apicobasal polarity (see cells 1 and 4, see also cell 1 at t = 2.5 hours (hrs) and cells 3' and 3'' at t = 5 hrs). Note, at t = 2.5 and 5.0 hrs, the presence of intracytoplasmic eGFP-Podxl2 labelled vesicles inside HE cells, suggesting vesicular transport (white arrowheads, to be compared with images ***Figure 2 – figure supplement 1***, at 30 hpf). At 48 hpf (bottom panel), HE cells have emerged and remain, for some of them, in close contact with the aortic floor (after having performed mitosis (notably for HE cell 2 (the division is visualized at 5hrs) and for HE cell 3, each one giving rise to cells 2' - 2'' and 3' - 3'' respectively, all containing residual eGFP-Podxl2 containing membranes as EHT signature). Bar = 80μm.

Figure 3 – figure supplement 1. Phenotypic analysis of dt-runx1 expressing mutants: expansion of the thymus. A, maximum z-projections of confocal spinning disk sections of the thymus region of 5 dpf *Tg(kdrl:gal4;UAS:RFP)* (left, control) and incrossed *Tg(kdrl:Gal4;UAS:RFP;4xNR:dt-runx1-eGFP)* (right, dt-runx1) larva. The area for each thymus is delimitated (white lines); note the systematic expansion of thymic cells on the right sides of each image for dt-runx1 mutants in comparison to controls. Bar: 20μm. **B**, Area of projected thymus for the 2 conditions illustrated in A. Statistical tests: two sided unpaired two samples Wilcoxon test, with p-values of significant differences only.

Figure 3 – figure supplement 2. Phenotypic analysis of dt-runx1 expressing mutants: evidence for apicobasal polarity of hemogenic cells. 30-32 hpf embryos obtained from

outcrossed Tg(Kdrl:Gal4;UAS:RFP;4xNR:mKate2-Podxl2) X Tg(kdrl:Gal4;UAS:RFP;4xNR:dt-runx1-eGFP) fishes and imaged in the trunk (AGM) region using spinning disk confocal microscopy. Images are depicting typical HE cells (in boxes) from hemogenic regions, with apical and basal membranes clearly separated from each other owing to reduction of their surface area (in comparison to flat aortic cells) and elongation in the antero-posterior axis. Luminal membranes are enriched with (magenta arrows) or more or less devoid of (green arrows) mkate2-Podxl2. Green: cytosolic eGFP released from the cleavage of *dt-runx1-eGFP*. Note that because of mosaicism, he cell 2 does not express mkate2-Podxl2. Bars:100μm.

Figure 3 – figure supplement 3. Phenotypic analysis of dt-runx1 expressing mutants: slowing down of the emergence process and accumulation of EHT cells. *Tg(kdrl:Gal4;UAS:RFP;4xNR:dt-runx1-eGFP)* embryos imaged using spinning disk confocal microscopy and analyzed in the AGM/trunk region. **A,** z-projections of the dorsal aorta obtained from 52-55 hpf embryos. Top panel: fluorescence from the red channel is shown for the *Tg(Kdrl:Gal4;UAS:RFP)* control. Bottom panels: fluorescence in the green channel only is shown for the mutants (eGFP, released form the dt-runx1-eGFP cleavage). The black asterisks point at emerged cells that are in close contact with the aortic floor. Green arrows: EHT pol+ cells on aortic floor; magenta arrows: EHT pol+ cells in the lateral aortic wall; white arrows: uncharacterized emerging cells; he: hemogenic cells. **B,** evolution of an EHT cell extracted from a 7 hrs time-lapse sequence (0 to 420 min) and showing significant changes in its morphology throughout emergence. Note the sub-luminal and cytosolic localization of pools of Podxl2 (notably at t = 30 min, magenta arrows) suggesting enhanced trafficking of the protein and relative instability of apical polarity features, consistently with apparent fluctuation of the luminal membrane surface contacting the aortic lumen (green arrows, in particular at t = 240 min). At t = 420 min, the cell has emerged and Podxl2 containing membranes remain in close contact with the membrane contacting the aortic floor. Bars:20μm.

Figure 5 – figure supplement 1. Model depicting the evolution of junctional interfaces and of the differential mobility of antero-posterior junctional complexes for EHT pol+ and EHT pol- cell emergence types. Top panel: EHT pol+ cell whose emergence depends on the constriction of circumferential actomyosin (orange, see Lancino et al. 2018) and the reduction of the membrane interface contacting endothelial neighbors shrinking along the longitudinal axis (horizontal double arrows) and in the 2D plane (endothelial neighbors are not depicted and are embedded in the blue X-Y plane). Presumably, the reduction of membrane interfaces relies on consumption via endocytosis. Green ovals: junctional complexes reinforced at antero-posterior poles. Green line: apical/luminal membrane with typical inward bending. **Bottom panel**: EHT pol- cell whose emergence depends on the dynamics of adhesion pools that move synchronously in 3D (X, Y, Z), both at antero-posterior poles (blue ovals) and at lateral sides of the emerging cell contacting endothelial neighbors (adjoining endothelial cells are not depicted and are embedded in the blue X-Y plane). Presumably, this type of emergence in which endothelial cells crawl over the EHT cell (curved arrows) involves, for the latter, a partial retrograde endocytic recycling of junctional complexes (opposite to the direction of emergence). Note that nuclei are not drawn at scale.

Figure 5 – figure supplement 2. JAM2a and JAM3b expression and localization in diverse embryonic tissues. Localization of transiently expressed eGFP-Jam2a (**A-D**) and eGFP-Jam3b (**E-G**) in 52 hpf embryos, using spinning disk confocal microscopy. Plasmid constructs were expressed under the control of the heat shock *Hsp70* promoter. For both constructs, expression was induced approximately 6 hrs before imaging, by 1hour balneation in 39°C embryo medium. All images are maximum z-projections. **A, E,** ependymal cells. White and red arrows point at reinforcement of eGFP-Jam2a and eGFP-Jam3b at apical intercellular junctions and at basolateral membranes, respectively. **B,** pronephric tubule cells. White arrows point at the reinforcement of the eGFP-Jam2a signal at apical sides of membranes of polarized

cells constituting pronephric tubules. The red arrow points at baso-lateral localization of eGFP-Jam2a. **C, F,** skin epithelial cells. White arrows point at the localization of eGFP-Jam2a and eGFP-Jam3b at lateral junctional interfaces between two neighboring cells. Red arrows point at tri-cellular junctions at which the density of eGFP-Jam2a and eGFP-Jam3b is reinforced. **D,** skin epithelial cells. White arrows point at membrane protrusions. **G,** Striated muscle cells. Red arrows point at T-tubules (invagination of the sarcolemmal membranes); white arrows point at the plasma membranes of myofibrils. Bars: 20μm.

Figure 6 – figure supplement 1. Examples of junctional contacts targeted by FRAP in the aortic landscape. After performing z-stack acquisitions in trunk regions followed by 2D-deployment of aortic segments (**A-C**), 4 different *Tg(kdrl:eGFP-Jam3b; kdrl:nls-mKate2)* 48-55 hpf embryos were illuminated for FRAP. Panels (**A)** and (**B)** are the entire segments from which cropped images of EHT pol+ and EHT pol- cells (black asterisks) and surroundings were extracted to build the panels A and B of ***Figure 6***. Panels (**C**) and (**D**) are from 2 other embryos. The 2D-cartographies allow visualizing the junctions that were selected for FRAP, with the black arrows pointing at junctional interfaces between EHT and endothelial cells (all are in the area of tri-junctions) and the green arrows pointing at bi-junctions (Bj) or tri-junctions between endothelial cells (green asterisks). Bar = 20μm.

Figure 7 – figure supplement 1. Searching for PDZ-domain containing RhoGEFs potentially involved in the EHT. A, cartoons representing the domains composing the 9 PDZ domain-containing RhoGEFs that were investigated in this study (all these RhoGEFs are encoded by different genes in the zebrafish; protein respective length is not drawn at scale). **B,** results obtained from 3 independent qRT-PCR experiments and performed on material extracted from trunk regions of 35 and 48 hpf embryos obtained from incrossed *Tg(kdrl:Gal4;UAS:RFP;4xNR:dt-runx1-eGFP)* adult fishes. Statistical tests: two sided unpaired two samples Wilcoxon test, with p-values of significant differences. GEF: guanine nucleotide-

exchange factor; PDZ: postsynaptic density protein of 95 kDa, Discs large and Zona occludens-1; PH: Plekstrin homology; RGS: regulator of G-protein signaling; DH: Dbl (diffuse B-cell lymphoma) homology; RBD: Ras-binding domain; DEP: Dishevelled Egl-10 and Plekstrin; InsPx4-PTPase: PtdIns(1,3,4,5)P4 phosphatidylinositol phosphatase; TIAM: T-cell-lymphoma invasion and metastasis; LARG: leukemia-associated Rho guanine-nucleotide exchange factor; PRex: PtdIns(3,4,5)P3-dependant Rac exchanger-1 and 2.

Figure 7 – figure supplement 2. Whole mount in situ hybridizations (WISH) performed on 30-32 hpf and 48-50 hpf embryos, with probes specific for all 9 PDZ-domain containing RhoGEFs that were investigated in this study. Note that all RhoGEFs are detected in the dorsal aorta of the trunk region (white arrowheads).

Figure 7 – figure supplement 3. **A N-terminal fragment of ArhGEF11/PDZ-RhoGEF localizes at junctional membranes with enrichment at antero-posterior sites of EHT cells. A,** domains of ArhGEF11, including its actin binding site (L/IIxxFE) and the position of exon 38 encoded peptide. The bottom cartoon represents a protein deleted from its DH-PH domains and C-terminus that are replaced by eGFP (PDZ-PRD-RGS-eGFP) to follow the localization of the truncated fusion protein in expressing cells. **B**, localization of the ArhGEF11 PDZ-PRD-RGS-eGFP fusion protein after transient expression in the aorta (expression was obtained after injection of the plasmid, at the one cell stage, in the *Tg(Kdrl:Gal4;UAS:RFP)* fish line). Confocal images extracted from a time-lapse sequence (timing points t = 0 and t = 77 min) and showing either the eGFP channel only (left), or the merge between the green and the red channels (RFP labels the cytoplasm). Note the localization of PDZ-PRD-RGS-eGFP at membrane interfaces at early time point of the emergence and at the rim of an emerging cell (white arrowheads, second cell from the right) and its enrichment at antero-posterior sites of an EHT pol+ cell proceeding throughout emergence (right cell, at t = 0 and t = 77 min and bottom cartoons, green arrows point at localization/concentration of PDZ-PRD-RGS-eGFP).

Figure 7 – figure supplement 4. MO and CRISPR approaches to investigate the function of ArhGEF11/PDZ-RhoGEF in the EHT. A, splicing MO interfering with integration of exon 38. **Top panel**: cartoon representing exons/introns (not drawn at scale) composing the 3-prime region of the gene encoding for ArhGEF11, with the position of the splicing MO. **Middle panel**: agarose gel showing the 2 alternative mRNAs encoding for ArhGEF11 in control animals (left track, control) and after injection of the MO at the one cell stage (right track, +MO at 2 and 5ng). **Bottom panel**: ArhGEF11 DNA sequences obtained after RT-PCR, cloning and sequencing for 1 control and 2 +MO clones (+MO1, +MO3). **B**, morphologies of control and +MO injected 48 hpf embryos. Note the absence of malformations. **C**, **top panel**: ArhGEF11 wild type and CRISPR-mediated 7bp deletion in the 3-prime region of exon 38 leading to a frame-shift in the ORF and a downstream premature stop codon; **middle panel**: CRISPR del/C-ter nucleotide/aa sequence and wild type nucleotide/aa sequence covering the extreme C-ter of the full-length protein; **bottom panel**: CLUSTAL 2.1 multiple sequence alignment of mouse and zebrafish C-termini highlighting the sequences of spliced variants of potentially similar activity in the regulation of ArhGEF11 activity on RhoA. Accession numbers: NP_001003912.1 and NP_001027010.1 for the mouse and Danio rerio sequence, respectively. **D,** morphologies of control and homozygous ArhGEF11$^{CRISPR\text{-}Cterdel+/+}$ 48 hpf embryos (*(Kdrl:eGFP-Jam3b; kdrl:*ArhGEF11$^{CRISPR\text{-}Cterdel+/+}$) embryos). Note the edema in the cardiac region (35 hpf embryos also exhibited retardation in blood circulation).

Figure 7 – figure supplement 5. Supplementary data on the ArhGEF11/PDZ-RhoGEF exon 38 splicing morpholino phenotype. *Tg(kdrl:eGFP-Jam2a; kdrl:nls-mKate2)* control (**A, C, E**) or MO-injected (**B, D, F**) embryos were imaged using spinning disk confocal microscopy (48-55 hpf time-window). Aorta segments (330 μm each) were imaged in the trunk region (AGM). The 2D-cartographies with delimited cellular contours in panels **A** and **B** are presented

1668 ***Figure 7A*** with the corresponding un-modified 2D-cartographies shown on top for unmasking
1669 of contours. Panels **A** and **C** illustrate 2 different segments from the same embryo. Panels **B,**
1670 **D, F** illustrate segments from 3 different embryos. (a-f) Maximum z-projections of merged nls-
1671 mkate2 and eGFP-Jam2a signals for control (a, c, e) and for ArhGEF11 exon 38 splicing
1672 morpholino (b, d, f) conditions. For panels (a) and (b), maximum z-projections of the eGFP-
1673 Jam2a signal only are also shown. (a'-f') Single z-plane images of merged nls-mkate2 and
1674 eGFP-Jam2a signals for control (a', c', e') and for ArhGEF11 exon 38 splicing morpholino (b',
1675 d', f') conditions. For **e'**, the image is a composition of 2 different z-planes from the same field
1676 (the boundaries are marked with white ticks). In right margins, magenta and green arrowheads
1677 designate the aortic floor and roof, respectively. (a''-f'') 2D-cartographies (bottom, with
1678 delineated cellular contours) obtained from eGFP-Jam2a signals for control (a'', c'', e'') and for
1679 the ArhGEF11 exon 38 splicing morpholino (b'', d'', f'') conditions, respectively. Cell contours
1680 are delineated either in blue (endothelial cells), yellow (hemogenic cells), red (morphologically
1681 characterized EHT cells, red arrows), and small cells delineated by cyan boxes
1682 (morphologically uncharacterized EHT cells and putative post-mitotic cells remaining as pairs).
1683 Cellular contours have been semi-automatically segmented along the cellular interfaces
1684 labelled with eGFP-Jam3b (see ***Materials and Methods***). White and black arrows designate
1685 hemogenic cells with their nucleus visible on the z-section. Analyses were performed on 2 x
1686 control non-injected embryos and 3 x embryos injected at the one-cell stage with the
1687 ArhGEF11 exon 38 splicing MO. Bars = 20μm.
1688
1689 **Figure 7 – figure supplement 6. Supplementary data on the ArhGEF11/PDZ-RhoGEF**
1690 **CRISPR C-ter deletion phenotype.** *(Kdrl:eGFP-Jam3b; kdrl:*ArhGEF11$^{CRISPR\text{-}Cterdel+/+}$)
1691 homozygous ArhGEF11 C-ter deletion mutants (CRISPR ArhGEF11: panels **B, D, F**) and
1692 control siblings (Control: panels **A, C, E**) were imaged using spinning disk confocal microscopy
1693 (48-55hpf time-window). Note that the genetic background of the CRISPR fish line is

(Kdrl:GAL4; UAS:RFP) thus allowing the red cytosolic staining of aortic and hemogenic cells. Aorta segments (330 μm each) were imaged in the trunk region. The 2D-cartographies with delimited cellular contours in panels **A** and **B** are presented ***Figure 7B*** with the corresponding un-modified 2D-cartographies shown on top for unmasking of contours. Panels **A, C** and **D, F** illustrate 2 different segments from the same embryo. (a-f) Maximum z-projections of merged nls-mkate2 and eGFP-Jam3b signals for control (a, c, e) and for the CRISPR mutant (b, d, f) conditions. For panels (a) and (b), maximum z-projections of the eGFP-Jam2a signal only are also shown. (a'-f') Single z-plane images of merged nls-mkate2 and eGFP-Jam3b signals for control (a', c', e') and for ArhGEF11 exon 38 splicing morpholino (b', d', f') conditions. For b' and d', the image is a composition of 2 different z-planes from the same field (the boundaries are marked with white ticks). In right margins, magenta and green arrowheads designate the aortic floor and roof, respectively. (a''-f'') 2D-cartographies (bottom, with delineated cellular contours) obtained from eGFP-Jam3b signals for control (a'', c'', e'') and for the CRIPR mutant (b'', d'', f'') conditions, respectively.

Cell contours are delineated either in blue (endothelial cells), yellow (hemogenic cells), red (morphologically characterized EHT cells, red arrows), and small cells delineated by cyan boxes (morphologically uncharacterized EHT cells). Cellular contours have been semi-automatically segmented along the cellular interfaces labelled with eGFP-Jam3b (see ***Materials and Methods***). White and black arrows designate hemogenic cells with their nucleus visible on the z-section. Analyses were performed on 2 x wild-type siblings for controls and 2 x mutant embryos whose mutation was confirmed by DNA sequencing. Bars = 20μm.

References

Adamo, Luigi, Olaia Naveiras, Pamela L. Wenzel, Shannon McKinney-Freeman, Peter J. Mack, Jorge Gracia-Sancho, Astrid Suchy-Dicey, et al. 2009. "Biomechanical Forces Promote Embryonic Haematopoiesis." *Nature* 459 (7250): 1131–35. https://doi.org/10.1038/nature08073.

Akitake, Courtney M., Michelle Macurak, Marnie E. Halpern, and Mary G. Goll. 2011. "Transgenerational Analysis of Transcriptional Silencing in Zebrafish." *Developmental Biology* 352 (2): 191–201. https://doi.org/10.1016/j.ydbio.2011.01.002.

Barone, Cristiana, Roberto Orsenigo, Raffaella Meneveri, Silvia Brunelli, and Emanuele Azzoni. 2022. "One Size Does Not Fit All: Heterogeneity in Developmental Hematopoiesis." *Cells* 11 (6): 1061. https://doi.org/10.3390/cells11061061.

Bayless, Kayla J., and George E. Davis. 2002. "The Cdc42 and Rac1 GTPases Are Required for Capillary Lumen Formation in Three-Dimensional Extracellular Matrices." *Journal of Cell Science* 115 (6): 1123–36. https://doi.org/10.1242/jcs.115.6.1123.

Bengtsson, Henrik. 2022. *MatrixStats: Functions That Apply to Rows and Columns of Matrices (and to Vectors)*. https://github.com/HenrikBengtsson/matrixStats.

Bertrand, Julien Y., Neil C. Chi, Buyung Santoso, Shutian Teng, Didier Y. R. Stainier, and David Traver. 2010. "Haematopoietic Stem Cells Derive Directly from Aortic Endothelium during Development." *Nature* 464 (7285): 108–11. https://doi.org/10.1038/nature08738.

Bertrand, Julien Y., Albert D. Kim, Emily P. Violette, David L. Stachura, Jennifer L. Cisson, and David Traver. 2007. "Definitive Hematopoiesis Initiates through a Committed Erythromyeloid Progenitor in the Zebrafish Embryo." *Development* 134 (23): 4147–56. https://doi.org/10.1242/dev.012385.

Boisset, Jean-Charles, Wiggert van Cappellen, Charlotte Andrieu-Soler, Niels Galjart, Elaine Dzierzak, and Catherine Robin. 2010. "In Vivo Imaging of Haematopoietic Cells Emerging from the Mouse Aortic Endothelium." *Nature* 464 (7285): 116–20. https://doi.org/10.1038/nature08764.

Bonkhofer, Florian, Rossella Rispoli, Philip Pinheiro, Monika Krecsmarik, Janina Schneider-Swales, Ingrid Ho Ching Tsang, Marella de Bruijn, Rui Monteiro, Tessa Peterkin, and Roger Patient. 2019. "Blood Stem Cell-Forming Haemogenic Endothelium in Zebrafish Derives from Arterial Endothelium." *Nature Communications* 10 (1): 3577. https://doi.org/10.1038/s41467-019-11423-2.

Bosveld, Floris, Zhimin Wang, and Yohanns Bellaïche. 2018. "Tricellular Junctions: A Hot Corner of Epithelial Biology." *Current Opinion in Cell Biology*, Cell Dynamics, 54 (October): 80–88. https://doi.org/10.1016/j.ceb.2018.05.002.

Bruijn, Marella F. T. R de, Xiaoqian Ma, Catherine Robin, Katrin Ottersbach, Maria-Jose Sanchez, and Elaine Dzierzak. 2002. "Hematopoietic Stem Cells Localize to the Endothelial Cell Layer in the Midgestation Mouse Aorta." *Immunity* 16 (5): 673–83. https://doi.org/10.1016/S1074-7613(02)00313-8.

Bryant, David M., Julie Roignot, Anirban Datta, Arend W. Overeem, Minji Kim, Wei Yu, Xiao Peng, et al. 2014. "A Molecular Switch for the Orientation of Epithelial Cell Polarization." *Developmental Cell* 31 (2): 171–87. https://doi.org/10.1016/j.devcel.2014.08.027.

Buckley, Clare E., and Daniel St Johnston. 2022. "Apical–Basal Polarity and the Control of Epithelial Form and Function." *Nature Reviews Molecular Cell Biology* 23 (8): 559–77. https://doi.org/10.1038/s41580-022-00465-y.

Burns, Caroline Erter, Tony DeBlasio, Yi Zhou, Jin Zhang, Leonard Zon, and Stephen D Nimer. 2002. "Isolation and Characterization of Runxa and Runxb, Zebrafish Members of the Runt Family of Transcriptional Regulators." *Experimental Hematology* 30 (12): 1381–89. https://doi.org/10.1016/S0301-472X(02)00955-4.

Butko, Emerald, Martin Distel, Claire Pouget, Bart Weijts, Isao Kobayashi, Kevin Ng, Christian Mosimann, et al. 2015. "Gata2b Is a Restricted Early Regulator of Hemogenic Endothelium in the Zebrafish Embryo." *Development* 142 (6): 1050–61. https://doi.org/10.1242/dev.119180.

Campinho, Pedro, Paola Lamperti, Francesco Boselli, Andrej Vilfan, and Julien Vermot. 2020. "Blood Flow Limits Endothelial Cell Extrusion in the Zebrafish Dorsal Aorta." *Cell Reports* 31 (2): 107505. https://doi.org/10.1016/j.celrep.2020.03.069.

Chalin, Dmitrii, Charlotte Bureau, Andrea Parmeggiani, Sergei Rochal, Karima Kissa, and Ivan Golushko. 2021. "Modeling and Live Imaging of Mechanical Instabilities in the Zebrafish Aorta during Hematopoiesis." *Scientific Reports* 11 (1): 9316. https://doi.org/10.1038/s41598-021-88667-w.

Chi, Neil C., Robin M. Shaw, Sarah De Val, Guson Kang, Lily Y. Jan, Brian L. Black, and Didier Y. R. Stainier. 2008. "Foxn4 Directly Regulates Tbx2b Expression and Atrioventricular Canal Formation." *Genes & Development* 22 (6): 734–39. https://doi.org/10.1101/gad.1629408.

Chikumi, Hiroki, Ana Barac, Babak Behbahani, Yuan Gao, Hidemi Teramoto, Yi Zheng, and J. Silvio Gutkind. 2004. "Homo- and Hetero-Oligomerization of PDZ-RhoGEF, LARG and P115RhoGEF by Their C-Terminal Region Regulates Their in Vivo Rho GEF Activity and Transforming Potential." *Oncogene* 23 (1): 233–40. https://doi.org/10.1038/sj.onc.1207012.

Ciau-Uitz, Aldo, Rui Monteiro, Arif Kirmizitas, and Roger Patient. 2014. "Developmental Hematopoiesis: Ontogeny, Genetic Programming and Conservation." *Experimental Hematology*, Genomics and Model Organisms: New Horizons for Experimental Hematology, 42 (8): 669–83. https://doi.org/10.1016/j.exphem.2014.06.001.

Clarke, Erik, and Scott Sherrill-Mix. 2017. *Ggbeeswarm: Categorical Scatter (Violin Point) Plots*. https://github.com/eclarke/ggbeeswarm.

Cumano, Ana, Françoise Dieterlen-Lievre, and Isabelle Godin. 1996. "Lymphoid Potential, Probed before Circulation in Mouse, Is Restricted to Caudal Intraembryonic Splanchnopleura." *Cell* 86 (6): 907–16. https://doi.org/10.1016/S0092-8674(00)80166-X.

Daniel, Michael G., David Sachs, Jeffrey M. Bernitz, Yesai Fstkchyan, Katrina Rapp, Namita Satija, Kenneth Law, et al. 2019. "Induction of Human Hemogenesis in Adult Fibroblasts by Defined Factors and Hematopoietic Coculture." *FEBS Letters* 593 (23): 3266–87. https://doi.org/10.1002/1873-3468.13621.

Davis, George E., Kayla J. Bayless, and Anil Mavila. 2002. "Molecular Basis of Endothelial Cell Morphogenesis in Three-Dimensional Extracellular Matrices." *The Anatomical Record* 268 (3): 252–75. https://doi.org/10.1002/ar.10159.

De Chaumont, Fabrice, Stéphane Dallongeville, Nicolas Chenouard, Nicolas Hervé, Sorin Pop, Thomas Provoost, Vannary Meas-Yedid, et al. 2012. "Icy: An Open Bioimage Informatics Platform for Extended Reproducible Research." *Nature Methods* 9 (7): 690–96. https://doi.org/10.1038/nmeth.2075.

Dignum, Tessa, Barbara Varnum-Finney, Sanjay R. Srivatsan, Stacey Dozono, Olivia Waltner, Adam M. Heck, Takashi Ishida, et al. 2021. "Multipotent Progenitors and Hematopoietic Stem Cells Arise Independently from Hemogenic Endothelium in the Mouse Embryo." *Cell Reports* 36 (11): 109675. https://doi.org/10.1016/j.celrep.2021.109675.

Dufour, Alexandre, Roman Thibeaux, Elisabeth Labruyere, Nancy Guillen, and Jean-Christophe Olivo-Marin. 2011. "3-D Active Meshes: Fast Discrete Deformable Models for Cell Tracking in 3-D Time-Lapse Microscopy." *IEEE Transactions on Image Processing* 20 (7): 1925–37. https://doi.org/10.1109/TIP.2010.2099125.

Ebnet, Klaus. 2017. "Junctional Adhesion Molecules (JAMs): Cell Adhesion Receptors With Pleiotropic Functions in Cell Physiology and Development." *Physiological Reviews* 97 (4): 1529–54. https://doi.org/10.1152/physrev.00004.2017.

1818 Ebnet, Klaus, Michel Aurrand-Lions, Annegret Kuhn, Friedemann Kiefer, Stefan Butz, Kerstin
1819 Zander, Maria-Katharina Meyer Zu Brickwedde, Atsushi Suzuki, Beat A. Imhof, and
1820 Dietmar Vestweber. 2003. "The Junctional Adhesion Molecule (JAM) Family Members
1821 JAM-2 and JAM-3 Associate with the Cell Polarity Protein PAR-3: A Possible Role for
1822 JAMs in Endothelial Cell Polarity." *Journal of Cell Science* 116 (19): 3879–91.
1823 https://doi.org/10.1242/jcs.00704.
1824 Ebnet, Klaus, and Volker Gerke. 2022. "Rho and Rab Family Small GTPases in the Regulation
1825 of Membrane Polarity in Epithelial Cells." *Frontiers in Cell and Developmental Biology*
1826 10. https://www.frontiersin.org/articles/10.3389/fcell.2022.948013.
1827 Ebnet, Klaus, Daniel Kummer, Tim Steinbacher, Amrita Singh, Masanori Nakayama, and Maja
1828 Matis. 2018. "Regulation of Cell Polarity by Cell Adhesion Receptors." *Seminars in Cell*
1829 *& Developmental Biology*, Cell Polarity and Planar Cell Polarity Proteins, 81
1830 (September): 2–12. https://doi.org/10.1016/j.semcdb.2017.07.032.
1831 Ebnet, Klaus, Atsushi Suzuki, Yosuke Horikoshi, Tomonori Hirose, Maria-Katharina Meyer zu
1832 Brickwedde, Shigeo Ohno, and Dietmar Vestweber. 2001. "The Cell Polarity Protein
1833 ASIP/PAR-3 Directly Associates with Junctional Adhesion Molecule (JAM)." *The EMBO*
1834 *Journal* 20 (14): 3738–48. https://doi.org/10.1093/emboj/20.14.3738.
1835 Eilken, Hanna M., Shin-Ichi Nishikawa, and Timm Schroeder. 2009. "Continuous Single-Cell
1836 Imaging of Blood Generation from Haemogenic Endothelium." *Nature* 457 (7231): 896–
1837 900. https://doi.org/10.1038/nature07760.
1838 Frame, Jenna M., Katherine H. Fegan, Simon J. Conway, Kathleen E. McGrath, and James
1839 Palis. 2016. "Definitive Hematopoiesis in the Yolk Sac Emerges from Wnt-Responsive
1840 Hemogenic Endothelium Independently of Circulation and Arterial Identity." *Stem Cells*
1841 34 (2): 431–44. https://doi.org/10.1002/stem.2213.
1842 Gama-Norton, Leonor, Eva Ferrando, Cristina Ruiz-Herguido, Zhenyi Liu, Jordi Guiu, Abul B.
1843 M. M. K. Islam, Sung-Uk Lee, et al. 2015. "Notch Signal Strength Controls Cell Fate in
1844 the Haemogenic Endothelium." *Nature Communications* 6 (1): 8510.
1845 https://doi.org/10.1038/ncomms9510.
1846 Ganuza, Miguel, Brandon Hadland, Ashley Chabot, Chen Li, Guolian Kang, Irwin Bernstein,
1847 and Shannon McKinney-Freeman. 2017. "Murine Hemogenic Endothelial Precursors
1848 Display Heterogeneous Hematopoietic Potential Ex Vivo." *Experimental Hematology*
1849 51 (July): 25-35.e6. https://doi.org/10.1016/j.exphem.2017.04.006.
1850 Gao, Long, Joanna Tober, Peng Gao, Changya Chen, Kai Tan, and Nancy A. Speck. 2018.
1851 "RUNX1 and the Endothelial Origin of Blood." *Experimental Hematology* 68
1852 (December): 2–9. https://doi.org/10.1016/j.exphem.2018.10.009.
1853 Garcia-Porrero, Juan A., Isabelle E. Godin, and Françoise Dieterlen-Lièvre. 1995. "Potential
1854 Intraembryonic Hemogenic Sites at Pre-Liver Stages in the Mouse." *Anatomy and*
1855 *Embryology* 192 (5): 425–35. https://doi.org/10.1007/BF00240375.
1856 Garnier, Simon. 2021. *Viridis: Colorblind-Friendly Color Maps for R*. https://CRAN.R-
1857 project.org/package=viridis.
1858 Garrido-Urbani, S., P. F. Bradfield, and B. A. Imhof. 2014. "Tight Junction Dynamics: The Role
1859 of Junctional Adhesion Molecules (JAMs)." *Cell and Tissue Research* 355 (3): 701–15.
1860 https://doi.org/10.1007/s00441-014-1820-1.
1861 Ghosn, Eliver, Momoko Yoshimoto, Hiromitsu Nakauchi, Irving L. Weissman, and Leonore A.
1862 Herzenberg. 2019. "Hematopoietic Stem Cell-Independent Hematopoiesis and the
1863 Origins of Innate-like B Lymphocytes." *Development* 146 (15): dev170571.
1864 https://doi.org/10.1242/dev.170571.
1865 Grosjean, Philippe. 2019. *SciViews: SciViews - Main Package*. https://CRAN.R-
1866 project.org/package=SciViews.
1867 Gudipaty, Swapna Aravind, and Jody Rosenblatt. 2017. "Epithelial Cell Extrusion: Pathways
1868 and Pathologies." *Seminars in Cell & Developmental Biology*, Extracellular Vesicles,
1869 67 (July): 132–40. https://doi.org/10.1016/j.semcdb.2016.05.010.

Hadland, Brandon, and Momoko Yoshimoto. 2018. "Many Layers of Embryonic Hematopoiesis: New Insights into B-Cell Ontogeny and the Origin of Hematopoietic Stem Cells." *Experimental Hematology* 60 (April): 1–9. https://doi.org/10.1016/j.exphem.2017.12.008.

Herbert, Shane P., Jan Huisken, Tyson N. Kim, Morri E. Feldman, Benjamin T. Houseman, Rong A. Wang, Kevan M. Shokat, and Didier Y. R. Stainier. 2009. "Arterial-Venous Segregation by Selective Cell Sprouting: An Alternative Mode of Blood Vessel Formation." *Science* 326 (5950): 294–98. https://doi.org/10.1126/science.1178577.

Herwig, Lukas, Yannick Blum, Alice Krudewig, Elin Ellertsdottir, Anna Lenard, Heinz-Georg Belting, and Markus Affolter. 2011. "Distinct Cellular Mechanisms of Blood Vessel Fusion in the Zebrafish Embryo." *Current Biology* 21 (22): 1942–48. https://doi.org/10.1016/j.cub.2011.10.016.

Itoh, Masahiko. 2013. "ARHGEF11, a Regulator of Junction-Associated Actomyosin in Epithelial Cells." *Tissue Barriers* 1 (2): e24221. https://doi.org/10.4161/tisb.24221.

Itoh, Masahiko, Derek C. Radisky, Masaaki Hashiguchi, and Hiroyuki Sugimoto. 2017. "The Exon 38-Containing ARHGEF11 Splice Isoform Is Differentially Expressed and Is Required for Migration and Growth in Invasive Breast Cancer Cells." *Oncotarget* 8 (54): 92157–70. https://doi.org/10.18632/oncotarget.20985.

Itoh, Masahiko, Hiroyuki Sasaki, Mikio Furuse, Harunobu Ozaki, Toru Kita, and Shoichiro Tsukita. 2001. "Junctional Adhesion Molecule (JAM) Binds to PAR-3." *Journal of Cell Biology* 154 (3): 491–98. https://doi.org/10.1083/jcb.200103047.

Itoh, Masahiko, Sachiko Tsukita, Yuji Yamazaki, and Hiroyuki Sugimoto. 2012. "Rho GTP Exchange Factor ARHGEF11 Regulates the Integrity of Epithelial Junctions by Connecting ZO-1 and RhoA-Myosin II Signaling." *Proceedings of the National Academy of Sciences* 109 (25): 9905–10. https://doi.org/10.1073/pnas.1115063109.

Ivanovs, Andrejs, Stanislav Rybtsov, Elizabeth S. Ng, Edouard G. Stanley, Andrew G. Elefanty, and Alexander Medvinsky. 2017. "Human Haematopoietic Stem Cell Development: From the Embryo to the Dish." *Development* 144 (13): 2323–37. https://doi.org/10.1242/dev.134866.

Ivanovs, Andrejs, Stanislav Rybtsov, Lindsey Welch, Richard A. Anderson, Marc L. Turner, and Alexander Medvinsky. 2011. "Highly Potent Human Hematopoietic Stem Cells First Emerge in the Intraembryonic Aorta-Gonad-Mesonephros Region." *Journal of Experimental Medicine* 208 (12): 2417–27. https://doi.org/10.1084/jem.20111688.

Jaffredo, Thierry, Rodolphe Gautier, Anne Eichmann, and Françoise Dieterlen-Lièvre. 1998. "Intraaortic Hemopoietic Cells Are Derived from Endothelial Cells during Ontogeny." *Development* 125 (22): 4575–83. https://doi.org/10.1242/dev.125.22.4575.

Jaffredo, Thierry, and Laurent Yvernogeau. 2014. "How the Avian Model Has Pioneered the Field of Hematopoietic Development." *Experimental Hematology*, Genomics and Model Organisms: New Horizons for Experimental Hematology, 42 (8): 661–68. https://doi.org/10.1016/j.exphem.2014.05.009.

Jin, Suk-Won, Dimitris Beis, Tracy Mitchell, Jau-Nian Chen, and Didier Y. R. Stainier. 2005. "Cellular and Molecular Analyses of Vascular Tube and Lumen Formation in Zebrafish." *Development* 132 (23): 5199–5209. https://doi.org/10.1242/dev.02087.

Kalev-Zylinska, Maggie L., Julia A. Horsfield, Maria Vega C. Flores, John H. Postlethwait, Maria R. Vitas, Andrea M. Baas, Philip S. Crosier, and Kathryn E. Crosier. 2002. "Runx1 Is Required for Zebrafish Blood and Vessel Development and Expression of a Human RUNX1-CBF2T1 Transgene Advances a Model for Studies of Leukemogenesis." *Development* 129 (8): 2015–30. https://doi.org/10.1242/dev.129.8.2015.

Kamei, Makoto, W. Brian Saunders, Kayla J. Bayless, Louis Dye, George E. Davis, and Brant M. Weinstein. 2006. "Endothelial Tubes Assemble from Intracellular Vacuoles in Vivo." *Nature* 442 (7101): 453–56. https://doi.org/10.1038/nature04923.

Kassambara, Alboukadel. 2020. *Ggpubr: Ggplot2 Based Publication Ready Plots*. https://rpkgs.datanovia.com/ggpubr/.

Kataoka, Hiroko, Mitsuo Ochi, Koh-ichi Enomoto, and Akira Yamaguchi. 2000. "Cloning and Embryonic Expression Patterns of the Zebrafish Runt Domain Genes, Runxa and Runxb." *Mechanisms of Development* 98 (1): 139–43. https://doi.org/10.1016/S0925-4773(00)00445-7.

Kimmel, Charles B., William W. Ballard, Seth R. Kimmel, Bonnie Ullmann, and Thomas F. Schilling. 1995. "Stages of Embryonic Development of the Zebrafish." *Developmental Dynamics* 203 (3): 253–310. https://doi.org/10.1002/aja.1002030302.

Kissa, Karima, and Philippe Herbomel. 2010. "Blood Stem Cells Emerge from Aortic Endothelium by a Novel Type of Cell Transition." *Nature* 464 (7285): 112–15. https://doi.org/10.1038/nature08761.

Kobayashi, Isao, Jingjing Kobayashi-Sun, Yuto Hirakawa, Madoka Ouchi, Koyuki Yasuda, Hiroyasu Kamei, Shigetomo Fukuhara, and Masaaki Yamaguchi. 2020. "Dual Role of Jam3b in Early Hematopoietic and Vascular Development." *Development* 147 (1): dev181040. https://doi.org/10.1242/dev.181040.

Lagendijk, Anne Karine, Alpha S Yap, and Benjamin M Hogan. 2014. "Endothelial Cell–Cell Adhesion during Zebrafish Vascular Development." *Cell Adhesion & Migration* 8 (2): 136–45. https://doi.org/10.4161/cam.28229.

Lancino, Mylene, Sara Majello, Sebastien Herbert, Fabrice De Chaumont, Jean-Yves Tinevez, Jean-Christophe Olivo-Marin, Philippe Herbomel, and Anne Schmidt. 2018. "Anisotropic Organization of Circumferential Actomyosin Characterizes Hematopoietic Stem Cells Emergence in the Zebrafish." *ELife* 7 (August): e37355. https://doi.org/10.7554/eLife.37355.

Lancrin, Christophe, Milena Mazan, Monika Stefanska, Rahima Patel, Monika Lichtinger, Guilherme Costa, Özge Vargel, et al. 2012. "GFI1 and GFI1B Control the Loss of Endothelial Identity of Hemogenic Endothelium during Hematopoietic Commitment." *Blood* 120 (2): 314–22. https://doi.org/10.1182/blood-2011-10-386094.

Lee, SungKyoung, Benjamin Cieply, Yueqin Yang, Natoya Peart, Carl Glaser, Patricia Chan, and Russ P. Carstens. 2018. "Esrp1-Regulated Splicing of Arhgef11 Isoforms Is Required for Epithelial Tight Junction Integrity." *Cell Reports* 25 (9): 2417-2430.e5. https://doi.org/10.1016/j.celrep.2018.10.097.

Lie-A-Ling, Michael, Elli Marinopoulou, Yaoyong Li, Rahima Patel, Monika Stefanska, Constanze Bonifer, Crispin Miller, Valerie Kouskoff, and Georges Lacaud. 2014. "RUNX1 Positively Regulates a Cell Adhesion and Migration Program in Murine Hemogenic Endothelium Prior to Blood Emergence." *Blood* 124 (11): e11–20. https://doi.org/10.1182/blood-2014-04-572958.

Lundin, Vanessa, Wade W. Sugden, Lindsay N. Theodore, Patricia M. Sousa, Areum Han, Stephanie Chou, Paul J. Wrighton, et al. 2020. "YAP Regulates Hematopoietic Stem Cell Formation in Response to the Biomechanical Forces of Blood Flow." *Developmental Cell* 52 (4): 446-460.e5. https://doi.org/10.1016/j.devcel.2020.01.006.

Mack, Natalie Ann, and Marios Georgiou. 2014. "The Interdependence of the Rho GTPases and Apicobasal Cell Polarity." *Small GTPases* 5 (2): e973768. https://doi.org/10.4161/21541248.2014.973768.

Marshall, Caroline J., and Adrian J. Thrasher. 2001. "The Embryonic Origins of Human Haematopoiesis." *British Journal of Haematology* 112 (4): 838–50. https://doi.org/10.1046/j.1365-2141.2001.02537.x.

Meder, Doris, Anna Shevchenko, Kai Simons, and Joachim Füllekrug. 2005. "Gp135/Podocalyxin and NHERF-2 Participate in the Formation of a Preapical Domain during Polarization of MDCK Cells." *Journal of Cell Biology* 168 (2): 303–13. https://doi.org/10.1083/jcb.200407072.

1973 Medvinsky, Alexander, and Elaine Dzierzak. 1996. “Definitive Hematopoiesis Is Autonomously
1974 Initiated by the AGM Region.” *Cell* 86 (6): 897–906. https://doi.org/10.1016/S0092-
1975 8674(00)80165-8.
1976 Medvinsky, Alexander L., Nina L. Samoylina, Albrecht M. Müller, and Elaine A. Dzierzak. 1993.
1977 “An Early Pre-Liver Intraembryonic Source of CFU-S in the Developing Mouse.” *Nature*
1978 364 (6432): 64–67. https://doi.org/10.1038/364064a0.
1979 Monteiro, Rui, Philip Pinheiro, Nicola Joseph, Tessa Peterkin, Jana Koth, Emmanouela
1980 Repapi, Florian Bonkhofer, Arif Kirmizitas, and Roger Patient. 2016. “Transforming
1981 Growth Factor β Drives Hemogenic Endothelium Programming and the Transition to
1982 Hematopoietic Stem Cells.” *Developmental Cell* 38 (4): 358–70.
1983 https://doi.org/10.1016/j.devcel.2016.06.024.
1984 Moreno-Mateos, Miguel A., Charles E. Vejnar, Jean-Denis Beaudoin, Juan P. Fernandez,
1985 Emily K. Mis, Mustafa K. Khokha, and Antonio J. Giraldez. 2015. “CRISPRscan:
1986 Designing Highly Efficient SgRNAs for CRISPR-Cas9 Targeting in Vivo.” *Nature*
1987 *Methods* 12 (10): 982–88. https://doi.org/10.1038/nmeth.3543.
1988 Müller, A. M., A. Medvinsky, J. Strouboulis, F. Grosveld, and E. Dzierzak. 1994. “Development
1989 of Hematopoietic Stem Cell Activity in the Mouse Embryo.” *Immunity* 1 (4): 291–301.
1990 https://doi.org/10.1016/1074-7613(94)90081-7.
1991 Murayama, Emi, Karima Kissa, Agustin Zapata, Elodie Mordelet, Valérie Briolat, Hui-Feng Lin,
1992 Robert I. Handin, and Philippe Herbomel. 2006. “Tracing Hematopoietic Precursor
1993 Migration to Successive Hematopoietic Organs during Zebrafish Development.”
1994 *Immunity* 25 (6): 963–75. https://doi.org/10.1016/j.immuni.2006.10.015.
1995 Nielsen, Julie S., and Kelly M. McNagny. 2008. “Novel Functions of the CD34 Family.” *Journal*
1996 *of Cell Science* 121 (22): 3683–92. https://doi.org/10.1242/jcs.037507.
1997 Nieto, M. Angela, Ruby Yun-Ju Huang, Rebecca A. Jackson, and Jean Paul Thiery. 2016.
1998 “EMT: 2016.” *Cell* 166 (1): 21–45. https://doi.org/10.1016/j.cell.2016.06.028.
1999 Nishimura, Tamako, Hisao Honda, and Masatoshi Takeichi. 2012. “Planar Cell Polarity Links
2000 Axes of Spatial Dynamics in Neural-Tube Closure.” *Cell* 149 (5): 1084–97.
2001 https://doi.org/10.1016/j.cell.2012.04.021.
2002 North, Trista E., Marella F. T. R. de Bruijn, Terryl Stacy, Laleh Talebian, Evan Lind, Catherine
2003 Robin, Michael Binder, Elaine Dzierzak, and Nancy A. Speck. 2002. “Runx1 Expression
2004 Marks Long-Term Repopulating Hematopoietic Stem Cells in the Midgestation Mouse
2005 Embryo.” *Immunity* 16 (5): 661–72. https://doi.org/10.1016/S1074-7613(02)00296-0.
2006 North, Trista E., Wolfram Goessling, Marian Peeters, Pulin Li, Craig Ceol, Allegra M. Lord,
2007 Gerhard J. Weber, et al. 2009. “Hematopoietic Stem Cell Development Is Dependent
2008 on Blood Flow.” *Cell* 137 (4): 736–48. https://doi.org/10.1016/j.cell.2009.04.023.
2009 North, Trista, Ting-Lei Gu, Terryl Stacy, Qing Wang, Louisa Howard, Michael Binder, Miguel
2010 Marín-Padilla, and Nancy A. Speck. 1999. “*Cbfa2* Is Required for the Formation of Intra-
2011 Aortic Hematopoietic Clusters.” *Development* 126 (11): 2563–75.
2012 https://doi.org/10.1242/dev.126.11.2563.
2013 Olayioye, Monilola A., Bettina Noll, and Angelika Hausser. 2019. “Spatiotemporal Control of
2014 Intracellular Membrane Trafficking by Rho GTPases.” *Cells* 8 (12): 1478.
2015 https://doi.org/10.3390/cells8121478.
2016 Orkin, Stuart H., and Leonard I. Zon. 2008. “Hematopoiesis: An Evolving Paradigm for Stem
2017 Cell Biology.” *Cell* 132 (4): 631–44. https://doi.org/10.1016/j.cell.2008.01.025.
2018 Padfield, Daniel, and Granville Matheson. 2020. *Nls.Multstart: Robust Non-Linear Regression*
2019 *Using AIC Scores*. https://CRAN.R-project.org/package=nls.multstart.
2020 Patil, Indrajeet. 2022. *Ggstatsplot: Ggplot2 Based Plots with Statistical Details*.
2021 https://CRAN.R-project.org/package=ggstatsplot.
2022 Pei, Duanqing, Xiaodong Shu, Ama Gassama-Diagne, and Jean Paul Thiery. 2019.
2023 “Mesenchymal–Epithelial Transition in Development and Reprogramming.” *Nature Cell*
2024 *Biology* 21 (1): 44–53. https://doi.org/10.1038/s41556-018-0195-z.

Pradella, Davide, Chiara Naro, Claudio Sette, and Claudia Ghigna. 2017. "EMT and Stemness: Flexible Processes Tuned by Alternative Splicing in Development and Cancer Progression." *Molecular Cancer* 16 (1): 8. https://doi.org/10.1186/s12943-016-0579-2.

Ram, Karthik, and Hadley Wickham. 2018. *Wesanderson: A Wes Anderson Palette Generator*. https://github.com/karthik/wesanderson.

Ridley, Anne J. 2006. "Rho GTPases and Actin Dynamics in Membrane Protrusions and Vesicle Trafficking." *Trends in Cell Biology*, Membrane Dynamics, 16 (10): 522–29. https://doi.org/10.1016/j.tcb.2006.08.006.

Robert-Moreno, Àlex, Jordi Guiu, Cristina Ruiz-Herguido, M. Eugenia López, Julia Inglés-Esteve, Lluis Riera, Alex Tipping, et al. 2008. "Impaired Embryonic Haematopoiesis yet Normal Arterial Development in the Absence of the Notch Ligand Jagged1." *The EMBO Journal* 27 (13): 1886–95.

Rodriguez-Boulan, Enrique, Anne Müsch, and Andre Le Bivic. 2004. "Epithelial Trafficking: New Routes to Familiar Places." *Current Opinion in Cell Biology* 16 (4): 436–42. https://doi.org/10.1016/j.ceb.2004.06.013.

Román-Fernández, Alvaro, and David M. Bryant. 2016. "Complex Polarity: Building Multicellular Tissues Through Apical Membrane Traffic." *Traffic* 17 (12): 1244–61. https://doi.org/10.1111/tra.12417.

Rossman, Kent L., Channing J. Der, and John Sondek. 2005. "GEF Means Go: Turning on RHO GTPases with Guanine Nucleotide-Exchange Factors." *Nature Reviews Molecular Cell Biology* 6 (2): 167–80. https://doi.org/10.1038/nrm1587.

Sato, Yuki, Mugiho Shigematsu, Maria Shibata-Kanno, Sho Maejima, Chie Tamura, and Hirotaka Sakamoto. 2023. "Aquaporin Regulates Cell Rounding through Vacuole Formation during Endothelial-to-Hematopoietic Transition." *Development* 150 (11): dev201275. https://doi.org/10.1242/dev.201275.

Sehnert, Amy J., Anja Huq, Brant M. Weinstein, Charline Walker, Mark Fishman, and Didier Y. R. Stainier. 2002. "Cardiac Troponin T Is Essential in Sarcomere Assembly and Cardiac Contractility." *Nature Genetics* 31 (1): 106–10. https://doi.org/10.1038/ng875.

Shapiro, Irina M., Albert W. Cheng, Nicholas C. Flytzanis, Michele Balsamo, John S. Condeelis, Maja H. Oktay, Christopher B. Burge, and Frank B. Gertler. 2011. "An EMT–Driven Alternative Splicing Program Occurs in Human Breast Cancer and Modulates Cellular Phenotype." *PLOS Genetics* 7 (8): e1002218. https://doi.org/10.1371/journal.pgen.1002218.

Sood, Raman, Milton A. English, Christiane L. Belele, Hao Jin, Kevin Bishop, Rebecca Haskins, Mary Cathleen McKinney, et al. 2010. "Development of Multilineage Adult Hematopoiesis in the Zebrafish with a Runx1 Truncation Mutation." *Blood* 115 (14): 2806–9. https://doi.org/10.1182/blood-2009-08-236729.

Staneva, Ralitza, and Romain Levayer. 2023. "Chapter Five - Cell Polarity and Extrusion: How to Polarize Extrusion and Extrude Misspolarized Cells?" In *Current Topics in Developmental Biology*, edited by ULRICH Tepass, 154:131–67. Cell Polarity in Development and Disease. Academic Press. https://doi.org/10.1016/bs.ctdb.2023.02.010.

Strilić, Boris, Jan Eglinger, Michael Krieg, Martin Zeeb, Jennifer Axnick, Pavel Babál, Daniel J. Müller, and Eckhard Lammert. 2010. "Electrostatic Cell-Surface Repulsion Initiates Lumen Formation in Developing Blood Vessels." *Current Biology* 20 (22): 2003–9. https://doi.org/10.1016/j.cub.2010.09.061.

Strilić, Boris, Tomáš Kučera, Jan Eglinger, Michael R. Hughes, Kelly M. McNagny, Sachiko Tsukita, Elisabetta Dejana, Napoleone Ferrara, and Eckhard Lammert. 2009. "The Molecular Basis of Vascular Lumen Formation in the Developing Mouse Aorta." *Developmental Cell* 17 (4): 505–15. https://doi.org/10.1016/j.devcel.2009.08.011.

Swiers, Gemma, Claudia Baumann, John O'Rourke, Eleni Giannoulatou, Stephen Taylor, Anagha Joshi, Victoria Moignard, et al. 2013. "Early Dynamic Fate Changes in

Haemogenic Endothelium Characterized at the Single-Cell Level." *Nature Communications* 4 (1): 2924. https://doi.org/10.1038/ncomms3924.

Tian, Ye, Jin Xu, Shachuan Feng, Sicong He, Shizheng Zhao, Lu Zhu, Wan Jin, et al. 2017. "The First Wave of T Lymphopoiesis in Zebrafish Arises from Aorta Endothelium Independent of Hematopoietic Stem Cells." *Journal of Experimental Medicine* 214 (11): 3347–60. https://doi.org/10.1084/jem.20170488.

Weijts, Bart, Laurent Yvernogeau, and Catherine Robin. 2021. "Recent Advances in Developmental Hematopoiesis: Diving Deeper With New Technologies." *Frontiers in Immunology* 12. https://www.frontiersin.org/articles/10.3389/fimmu.2021.790379.

Wickham, Hadley. 2016. *Ggplot2: Elegant Graphics for Data Analysis*. Springer-Verlag New York. https://ggplot2.tidyverse.org.

Wickham. 2022. *Stringr: Simple, Consistent Wrappers for Common String Operations*. https://CRAN.R-project.org/package=stringr.

Wickham, Hadley, Romain François, Lionel Henry, Kirill Müller, and Davis Vaughan. 2023. *Dplyr: A Grammar of Data Manipulation*. https://CRAN.R-project.org/package=dplyr.

Wickham, Hadley, Jim Hester, and Jennifer Bryan. 2022. *Readr: Read Rectangular Text Data*. https://CRAN.R-project.org/package=readr.

Wilke, Claus O. 2020. *Cowplot: Streamlined Plot Theme and Plot Annotations for Ggplot2*. https://wilkelab.org/cowplot/.

Wu, Yinyu, and Karen K. Hirschi. 2021. "Regulation of Hemogenic Endothelial Cell Development and Function." *Annual Review of Physiology* 83 (February): 17–37. https://doi.org/10.1146/annurev-physiol-021119-034352.

Xia, Jun, Mengyao Liu, Caiying Zhu, Shicheng Liu, Lanlan Ai, Dongyuan Ma, Ping Zhu, Lu Wang, and Feng Liu. 2023. "Activation of Lineage Competence in Hemogenic Endothelium Precedes the Formation of Hematopoietic Stem Cell Heterogeneity." *Cell Research*, April, 1–16. https://doi.org/10.1038/s41422-023-00797-0.

Xiao, Nan. 2018. *Ggsci: Scientific Journal and Sci-Fi Themed Color Palettes for Ggplot2*. https://CRAN.R-project.org/package=ggsci.

Xie, Yihui, Joe Cheng, and Xianying Tan. 2022. *DT: A Wrapper of the JavaScript Library DataTables*. https://github.com/rstudio/DT.

Yoshimoto, Momoko, Encarnacion Montecino-Rodriguez, Michael J. Ferkowicz, Prashanth Porayette, W. Christopher Shelley, Simon J. Conway, Kenneth Dorshkind, and Mervin C. Yoder. 2011. "Embryonic Day 9 Yolk Sac and Intra-Embryonic Hemogenic Endothelium Independently Generate a B-1 and Marginal Zone Progenitor Lacking B-2 Potential." *Proceedings of the National Academy of Sciences* 108 (4): 1468–73. https://doi.org/10.1073/pnas.1015841108.

Yoshimoto, Momoko, Prashanth Porayette, Nicole L. Glosson, Simon J. Conway, Nadia Carlesso, Angelo A. Cardoso, Mark H. Kaplan, and Mervin C. Yoder. 2012. "Autonomous Murine T-Cell Progenitor Production in the Extra-Embryonic Yolk Sac before HSC Emergence." *Blood* 119 (24): 5706–14. https://doi.org/10.1182/blood-2011-12-397489.

Zhao, Shizheng, Shachuan Feng, Ye Tian, and Zilong Wen. 2022. "Hemogenic and Aortic Endothelium Arise from a Common Hemogenic Angioblast Precursor and Are Specified by the Etv2 Dosage." *Proceedings of the National Academy of Sciences* 119 (13): e2119051119. https://doi.org/10.1073/pnas.2119051119.

Zhu, Qin, Peng Gao, Joanna Tober, Laura Bennett, Changya Chen, Yasin Uzun, Yan Li, et al. 2020. "Developmental Trajectory of Prehematopoietic Stem Cell Formation from Endothelium." *Blood* 136 (7): 845–56. https://doi.org/10.1182/blood.2020004801.

Supplementary files

Supplementary file 1: Materials and Methods - Supplementary Table

Figure 1 – video 1. EHT pol+ cells at early timing. Z-stack (37 planes) corresponding to the time point t = 0 min whose plane 21 is shown ***Figure 1C***.

Figure 1 – video 2. EHT pol+ cells at late timing. Z-stack (37 planes) corresponding to the time point t = 80 min whose planes 16 (for eht cell 1) and 22 (for eht cell 2) are shown ***Figure 1 – figure supplement 1B.***

Figure 1 – video 3. Emergence of EHT pol- cells. Time-lapse sequence using a *Tg(Kdrl:Gal4;UAS:RFP;4xNR:eGFP-Podxl2)* embryo, obtained with spinning disk confocal microscopy (38 timing points, each acquired with 10 min intervals, starting at 55 hpf) and from which the images of the 2 emerging EHT pol- cells shown Figure 1D were extracted.

Figure 1

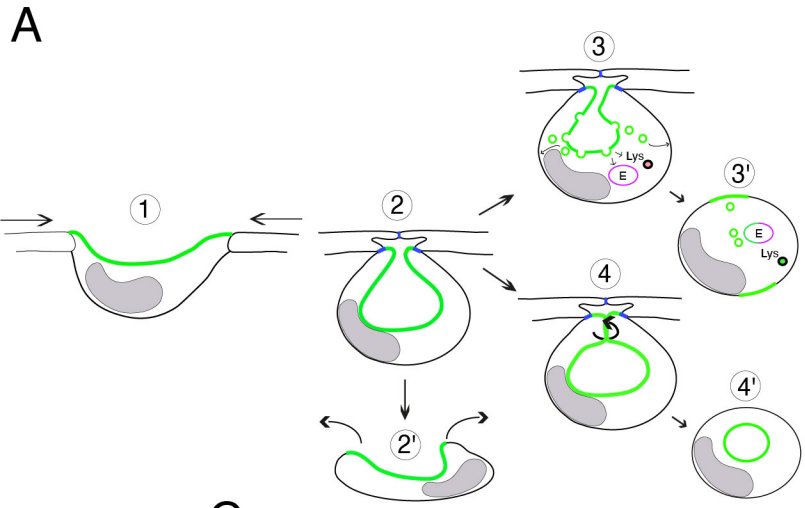
A
1
2
2'
3
3'
4
4'
Lys
E

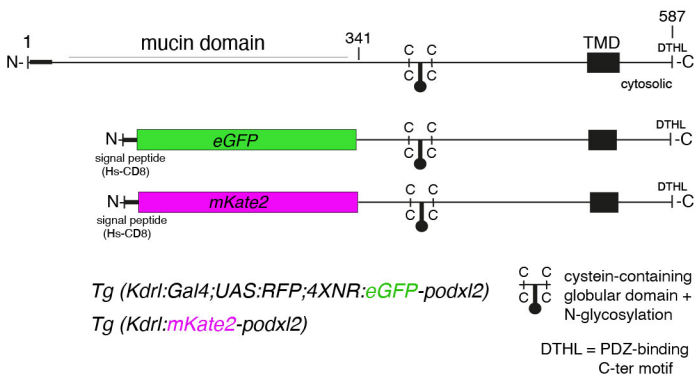
B
1
mucin domain
341
587
TMD
DTHL
N-
-C
cytosolic
eGFP
mKate2
signal peptide
(Hs-CD8)
Tg (Kdrl:Gal4;UAS:RFP;4XNR:eGFP-podxl2)
Tg (Kdrl:mKate2-podxl2)
cystein-containing
globular domain +
N-glycosylation
DTHL = PDZ-binding
C-ter motif

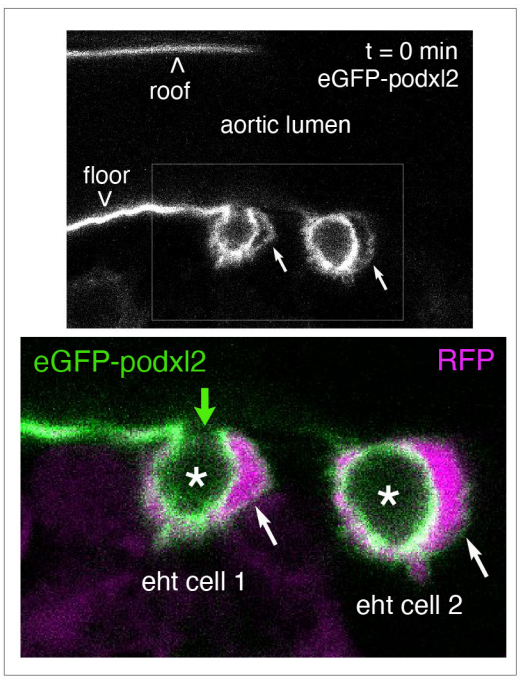
C
t = 0 min
eGFP-podxl2
roof
aortic lumen
floor
eGFP-podxl2
RFP
eht cell 1
eht cell 2

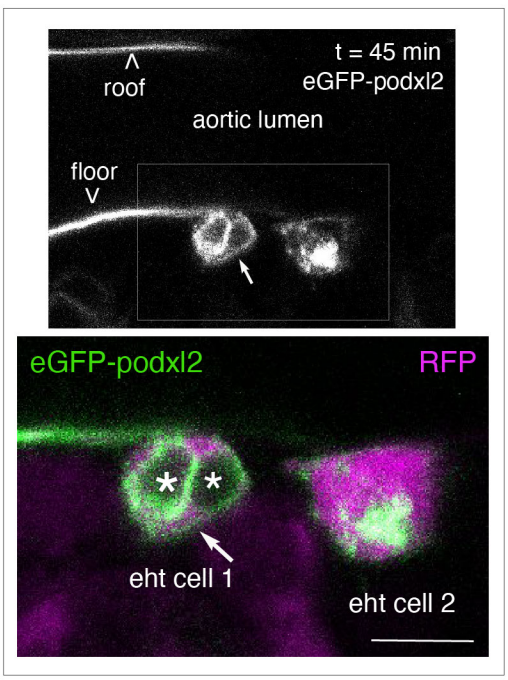
t = 45 min
eGFP-podxl2
roof
aortic lumen
floor
eGFP-podxl2
RFP
eht cell 1
eht cell 2

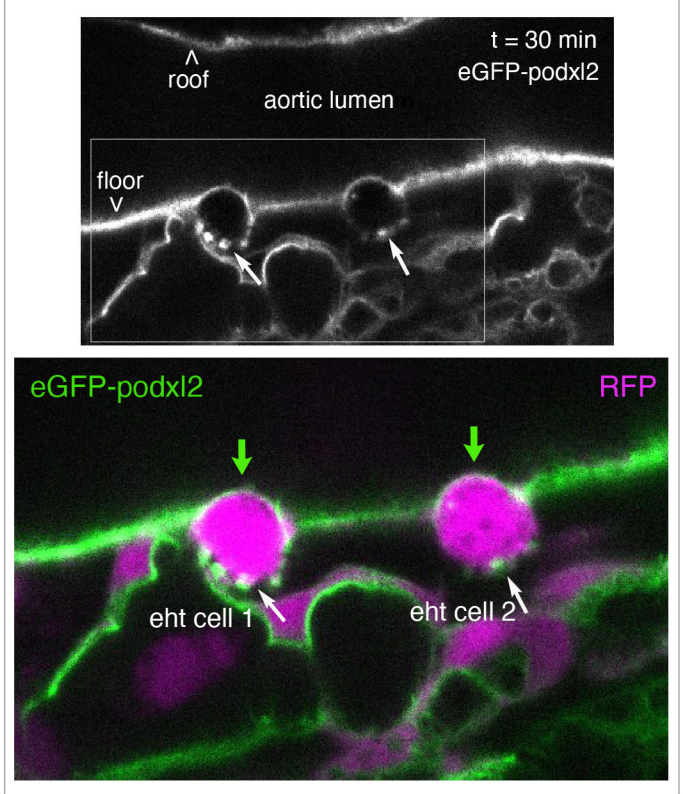
D
t = 30 min
eGFP-podxl2
roof
aortic lumen
floor
eGFP-podxl2
RFP
eht cell 1
eht cell 2

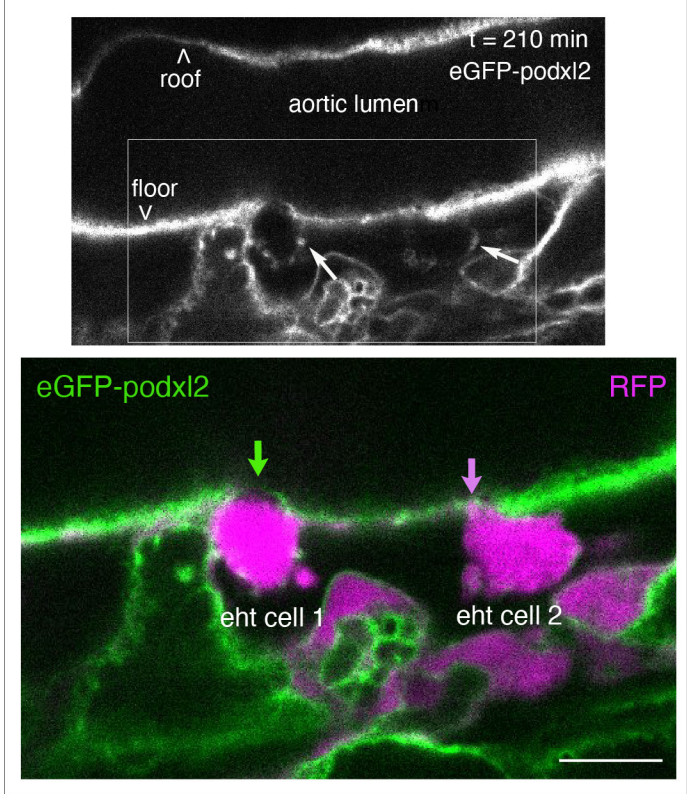
t = 210 min
eGFP-podxl2
roof
aortic lumen
floor
eGFP-podxl2
RFP
eht cell 1
eht cell 2

FIGURE 1 - figure supplement 1

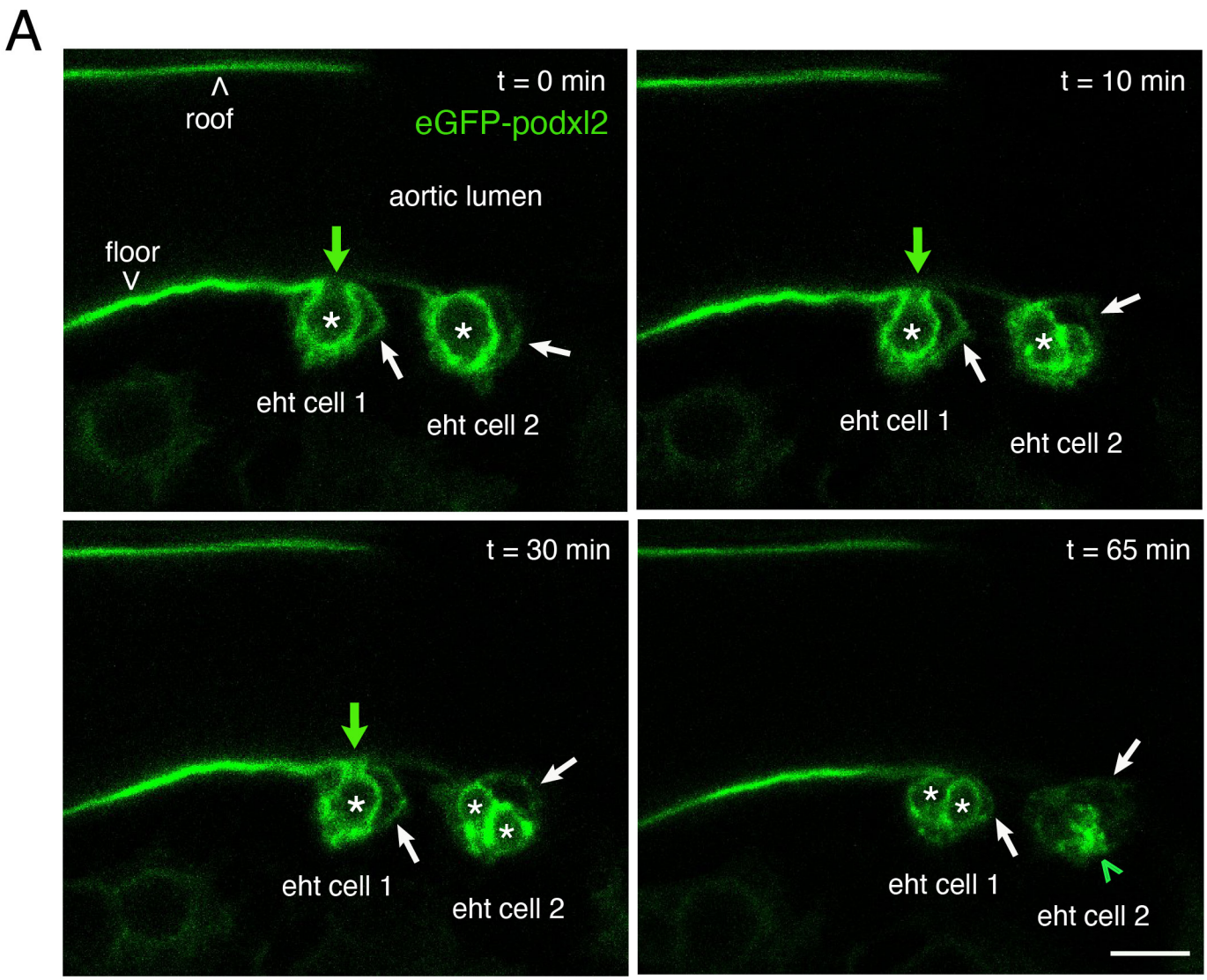

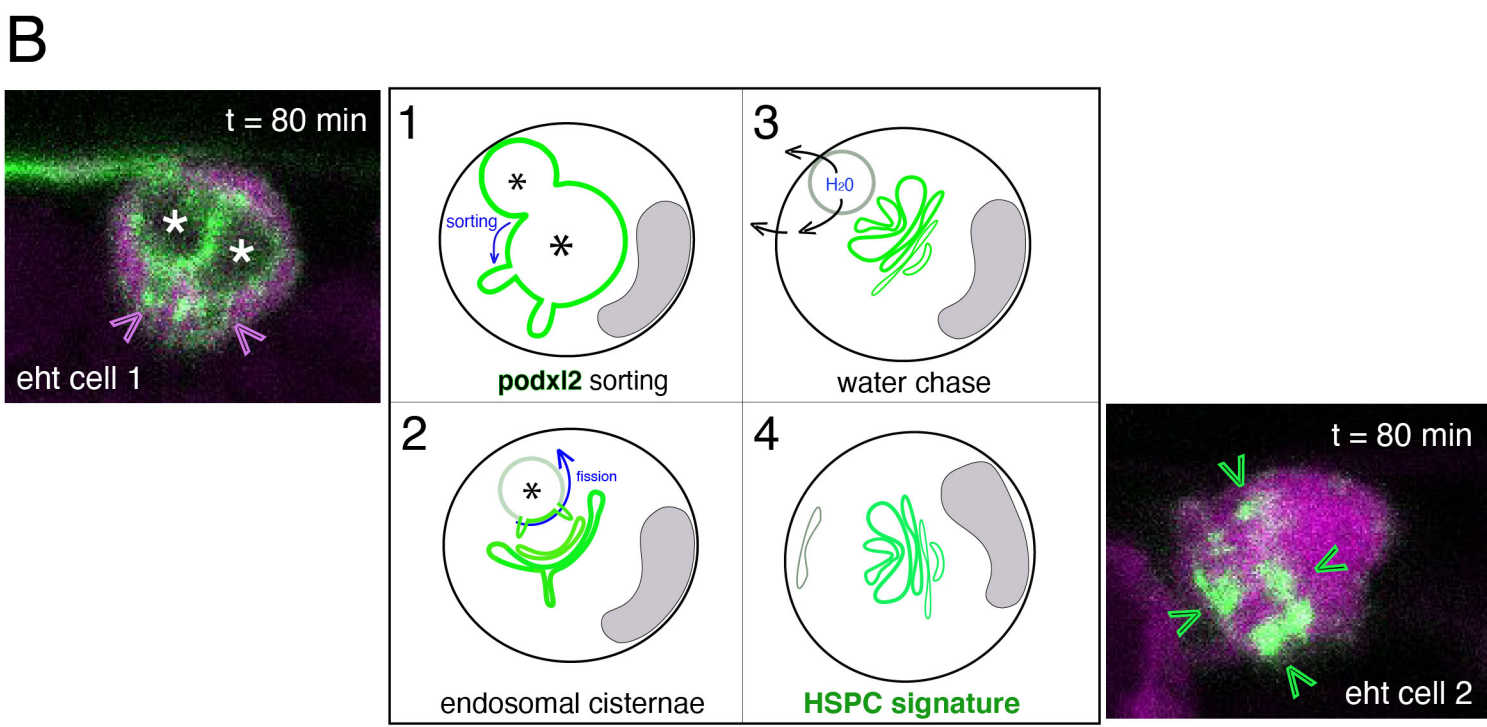

Figure 2

A

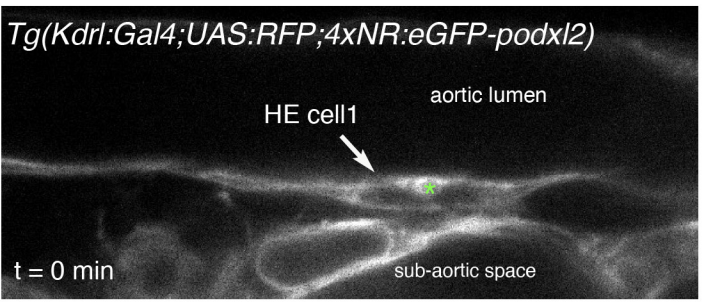
Tg(Kdrl:Gal4;UAS:RFP;4xNR:eGFP-podxl2)
HE cell1
aortic lumen
t = 0 min
sub-aortic space

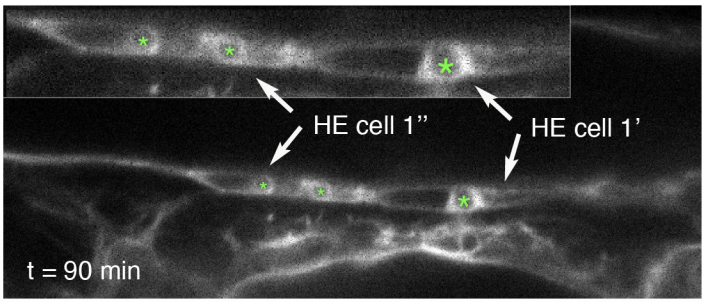
HE cell 1''
HE cell 1'
t = 90 min

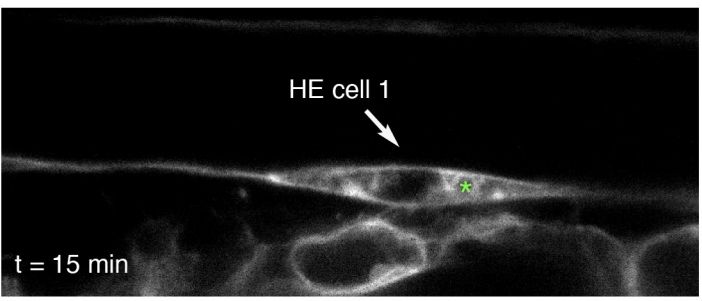
HE cell 1
t = 15 min

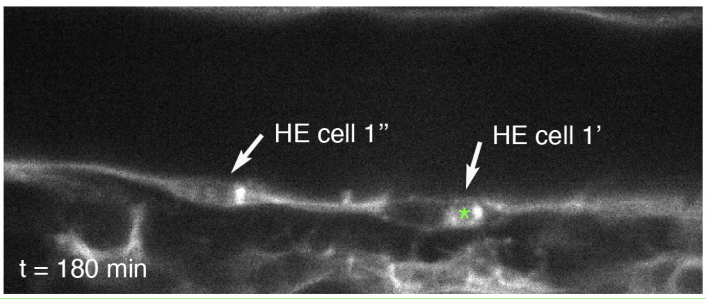
HE cell 1''
HE cell 1'
t = 180 min

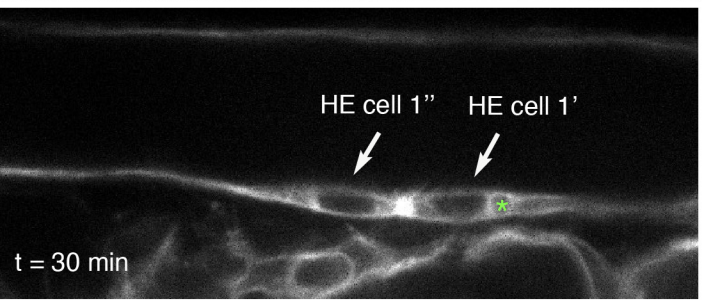
HE cell 1''
HE cell 1'
t = 30 min

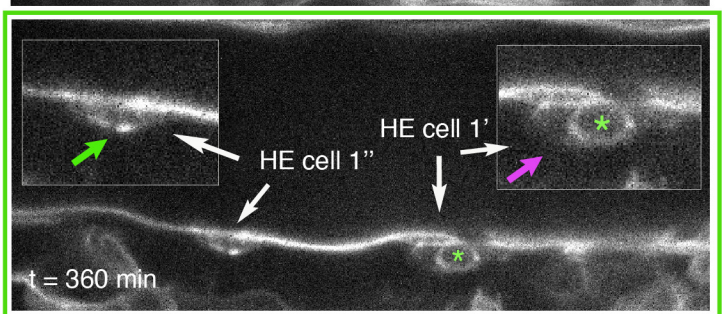
HE cell 1''
HE cell 1'
HE cell 1'
t = 360 min

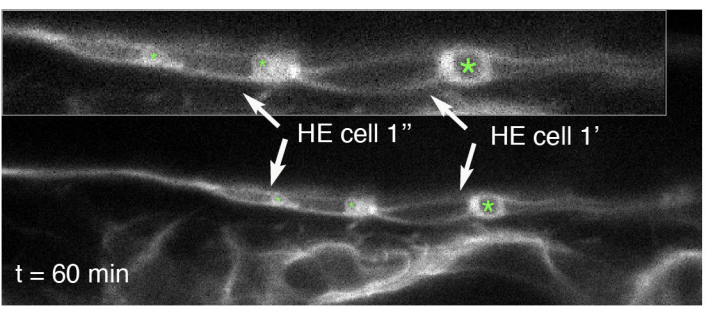
HE cell 1''
HE cell 1'
t = 60 min

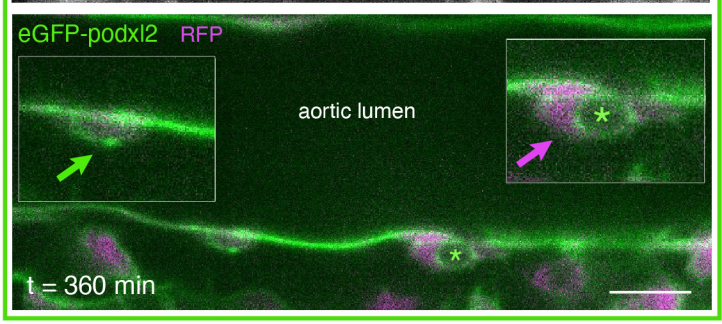
eGFP-podxl2
RFP
aortic lumen
t = 360 min

B

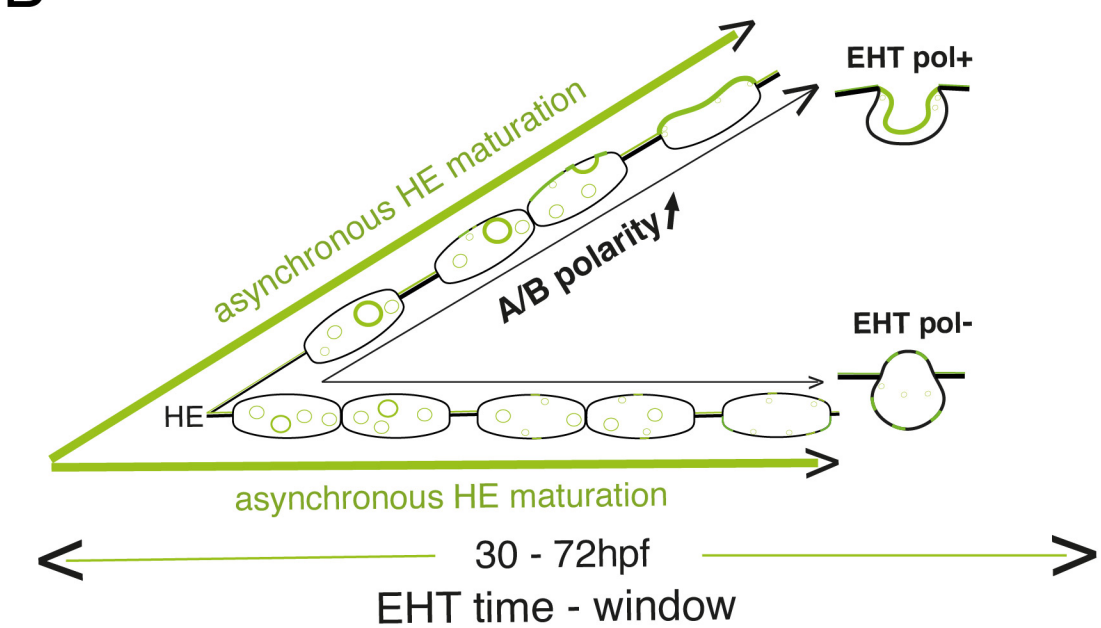
asynchronous HE maturation
EHT pol+
A/B polarity
EHT pol-
HE
asynchronous HE maturation
30 - 72hpf
EHT time - window

Figure 2
- figure supplement 1

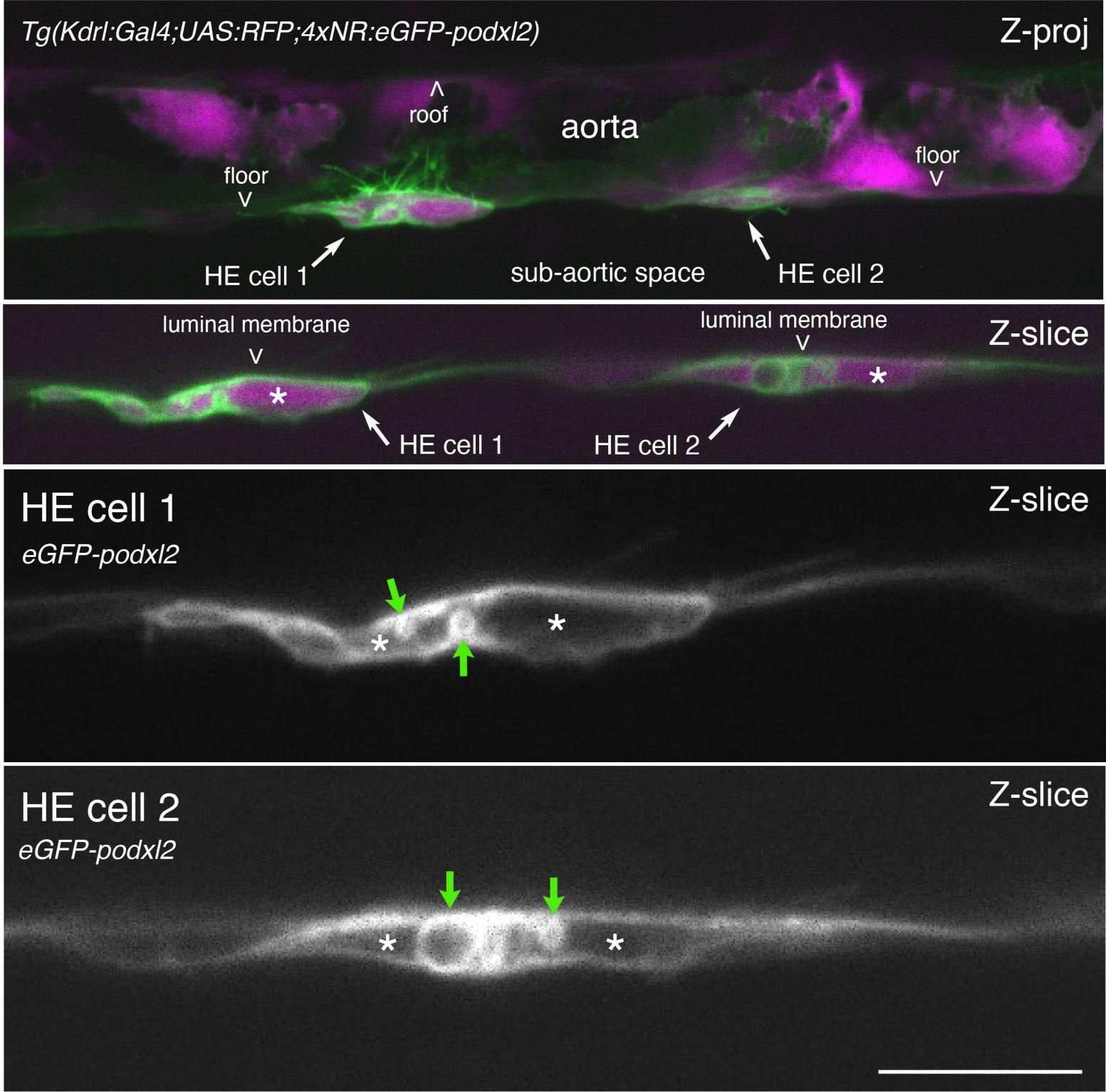

Figure 2 - figure supplement 2

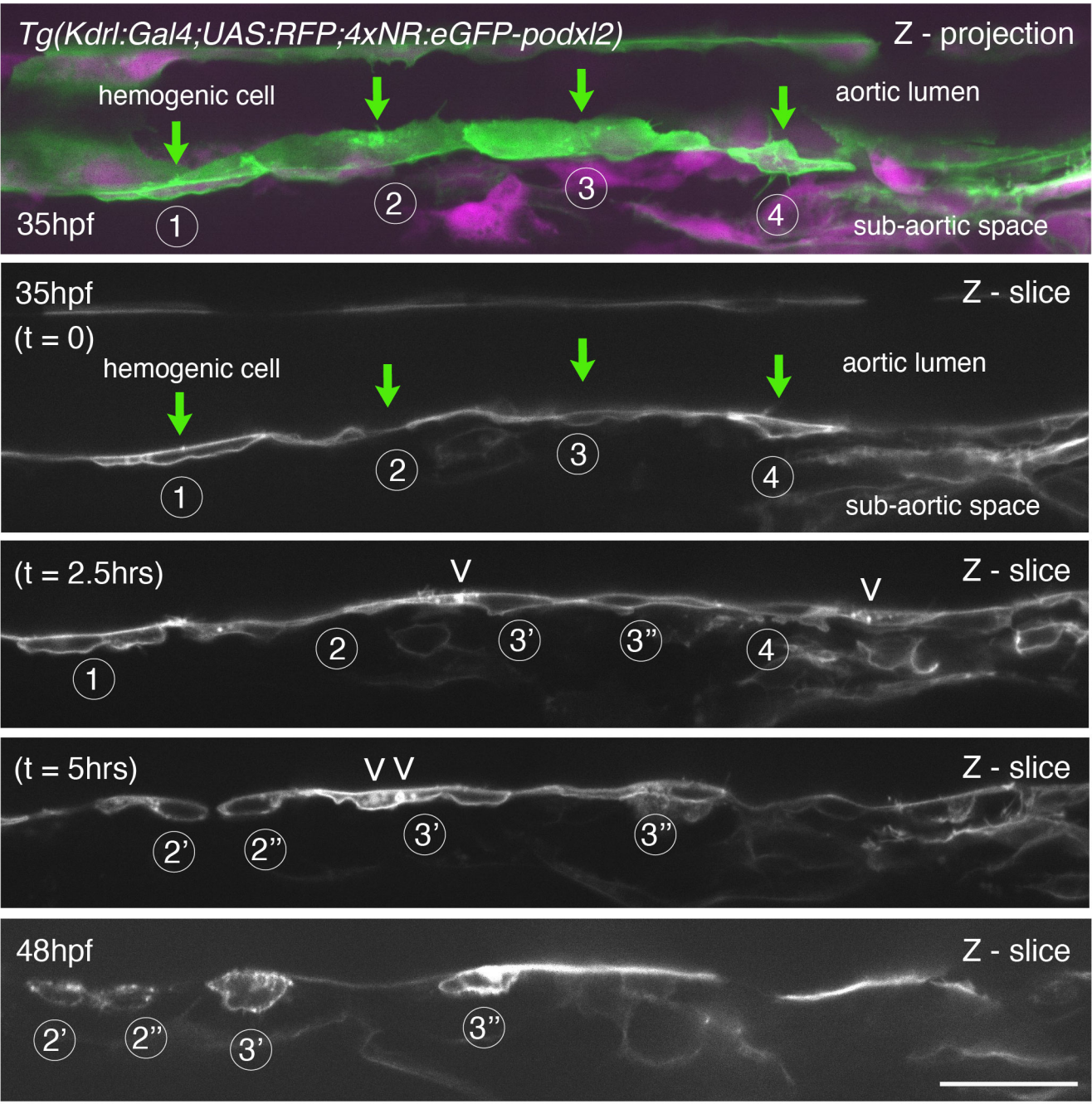

Figure 3

A

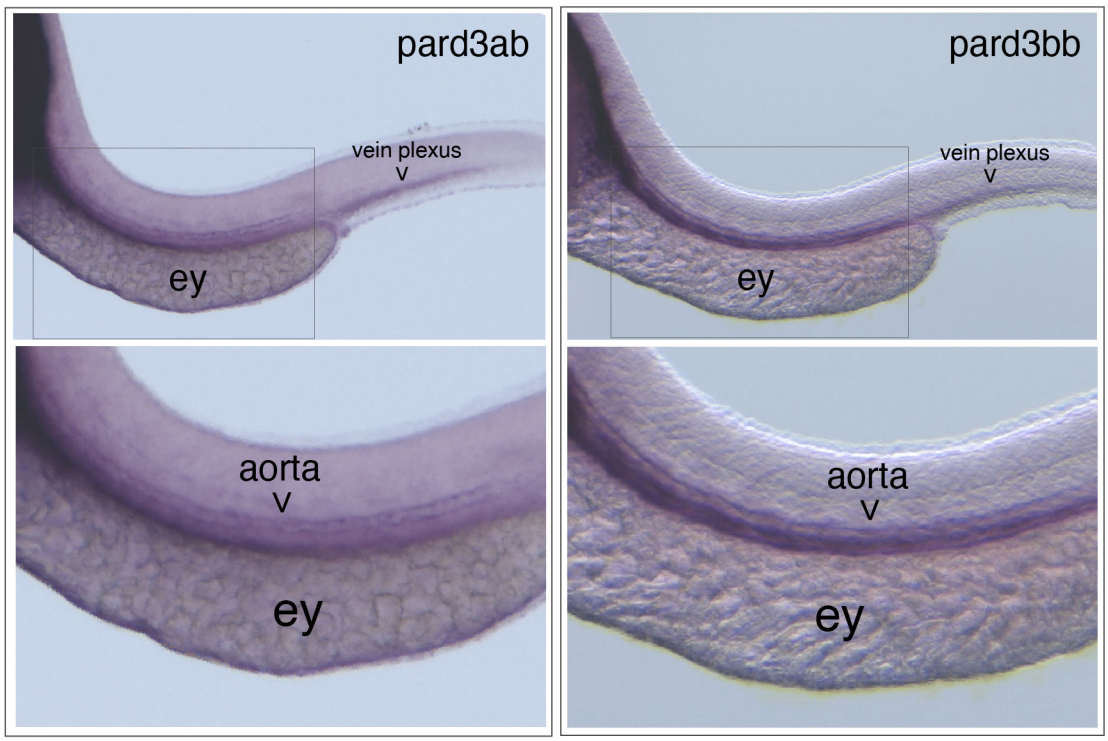

B

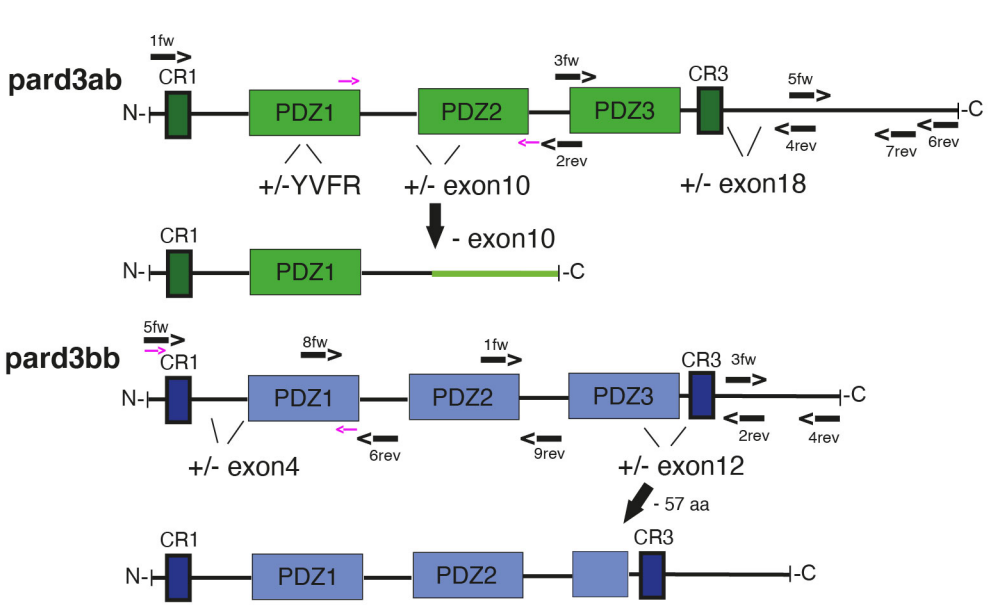

C

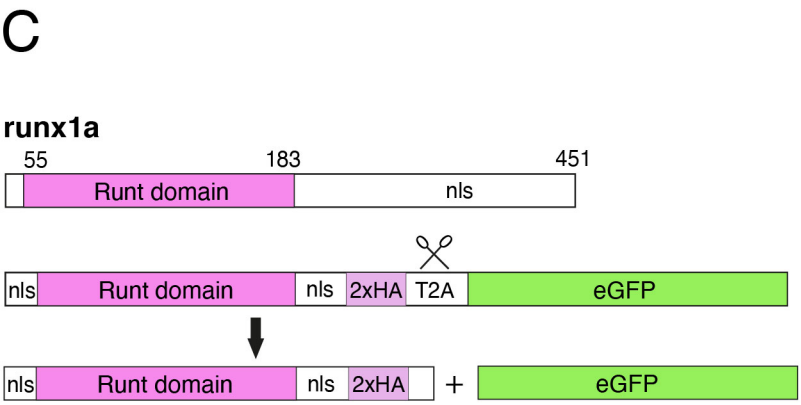

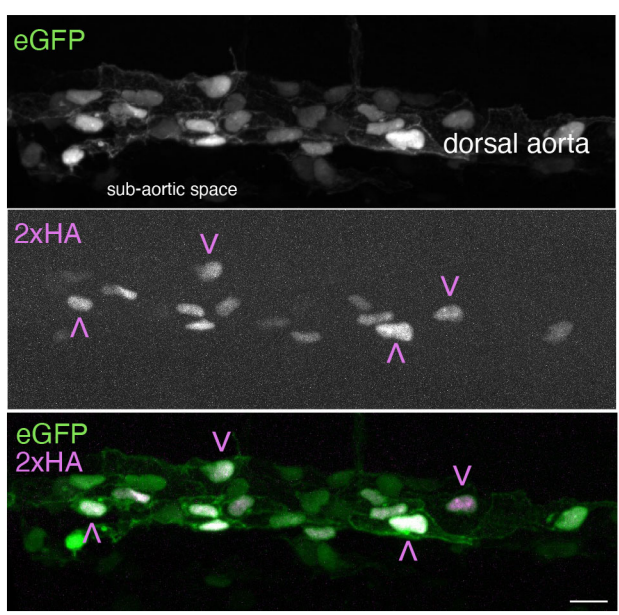

Bar = 25 μm

Figure 3 - figure supplement 1

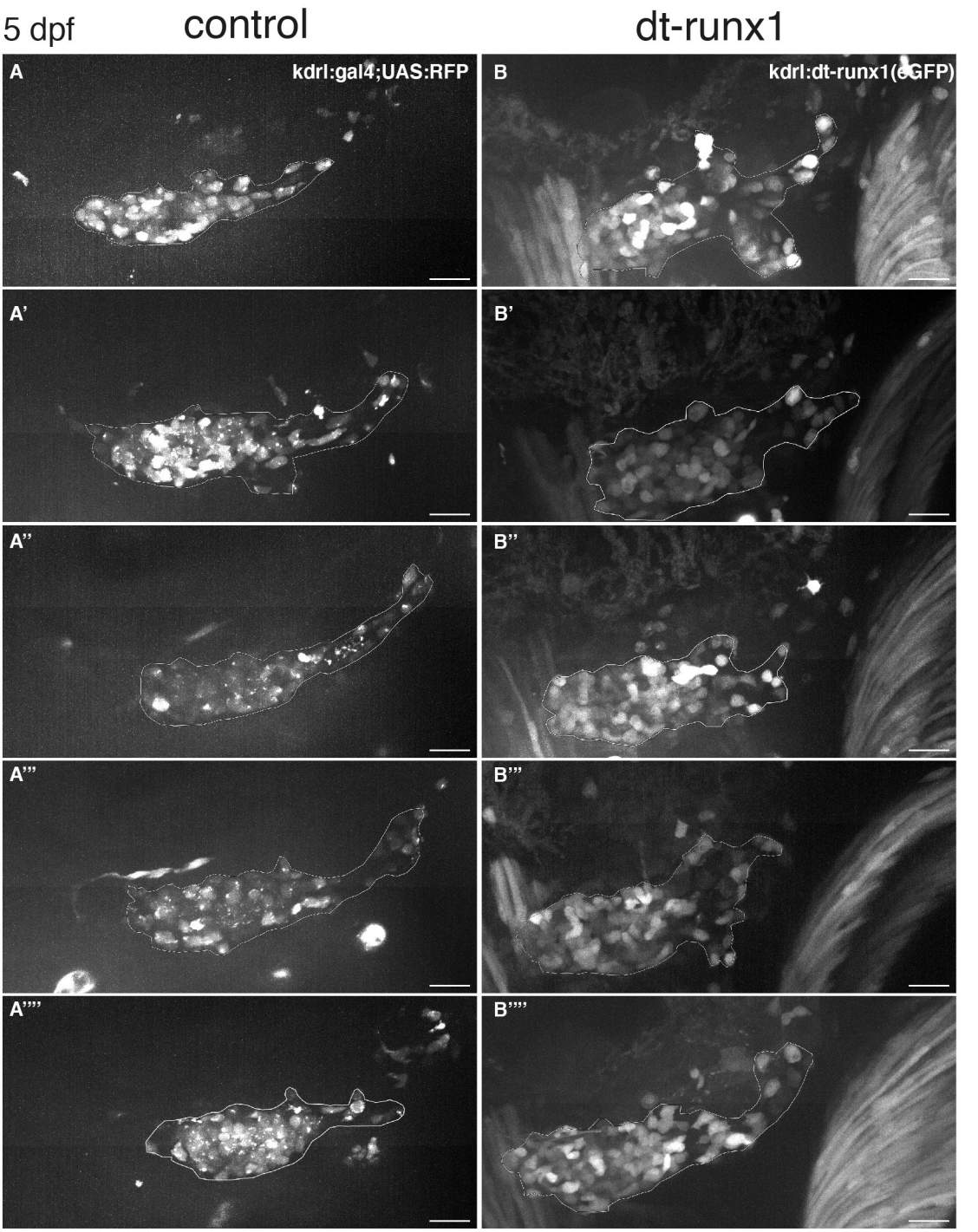

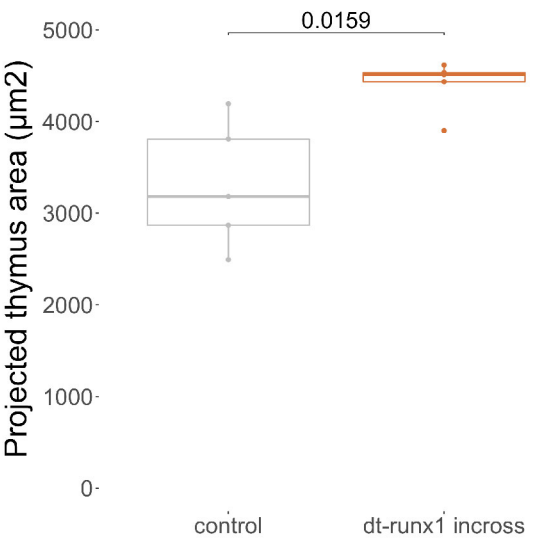

Figure 3 - figure supplement 2

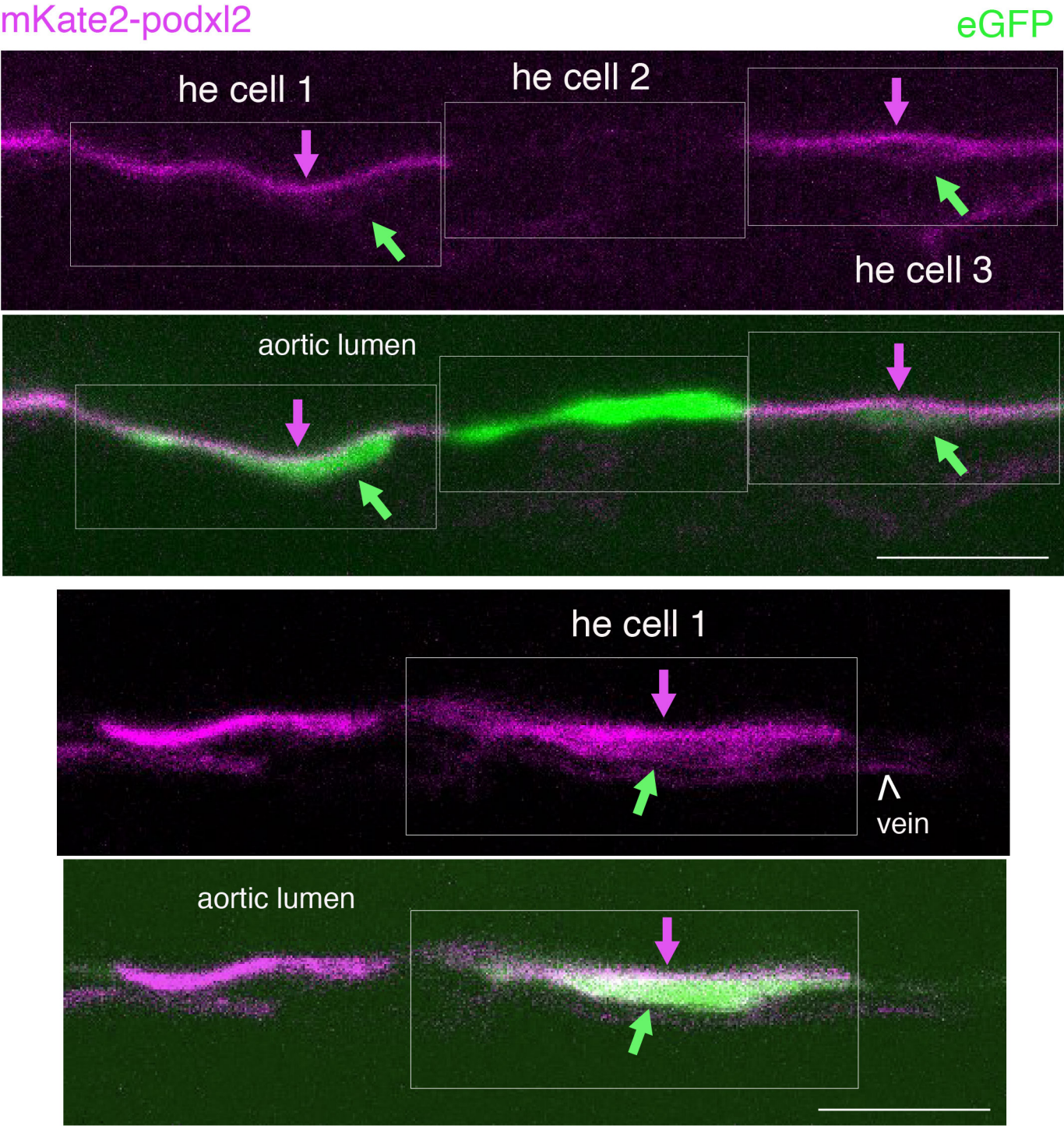

Figure 3 - figure supplement 3

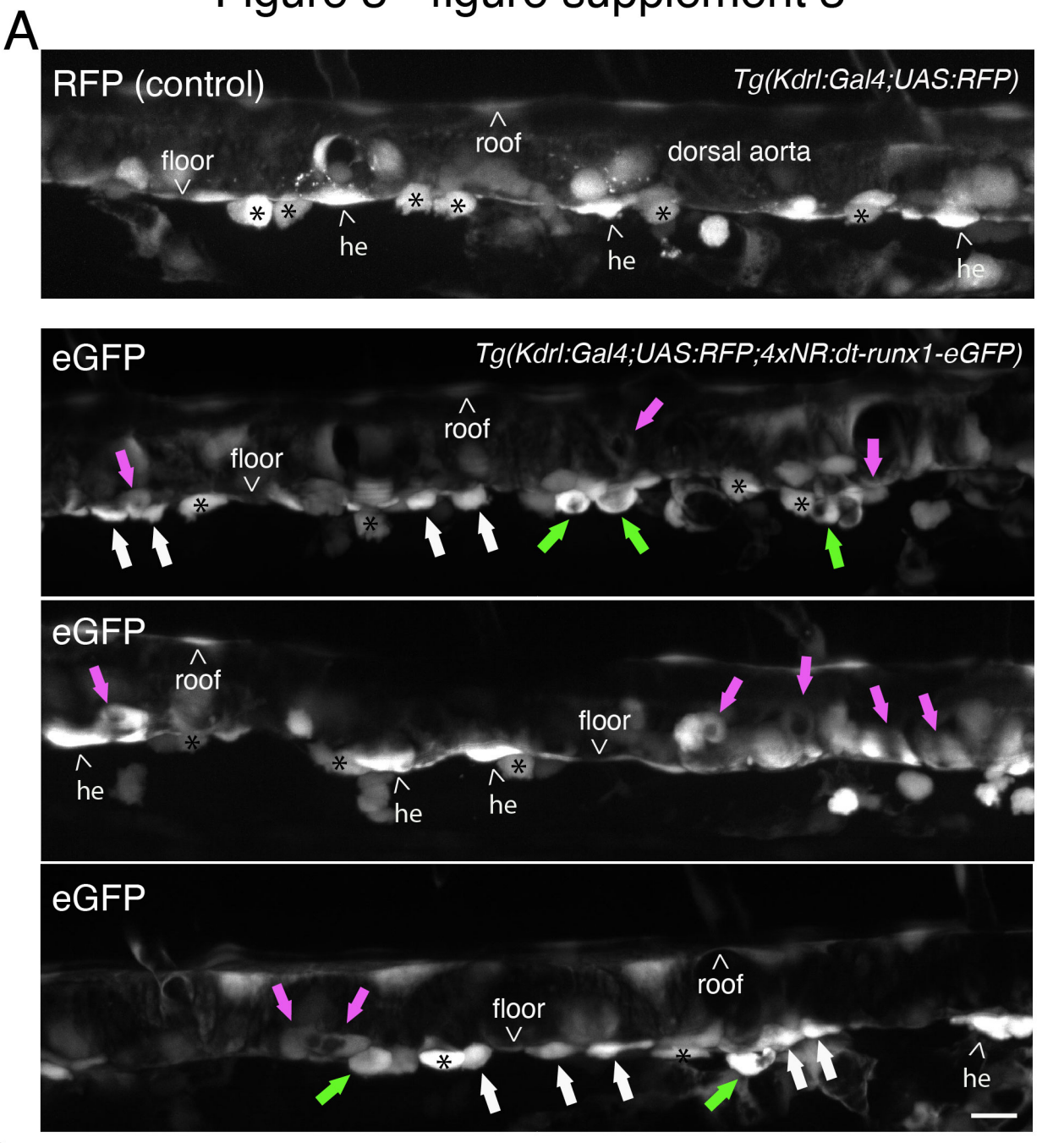

Figure 4

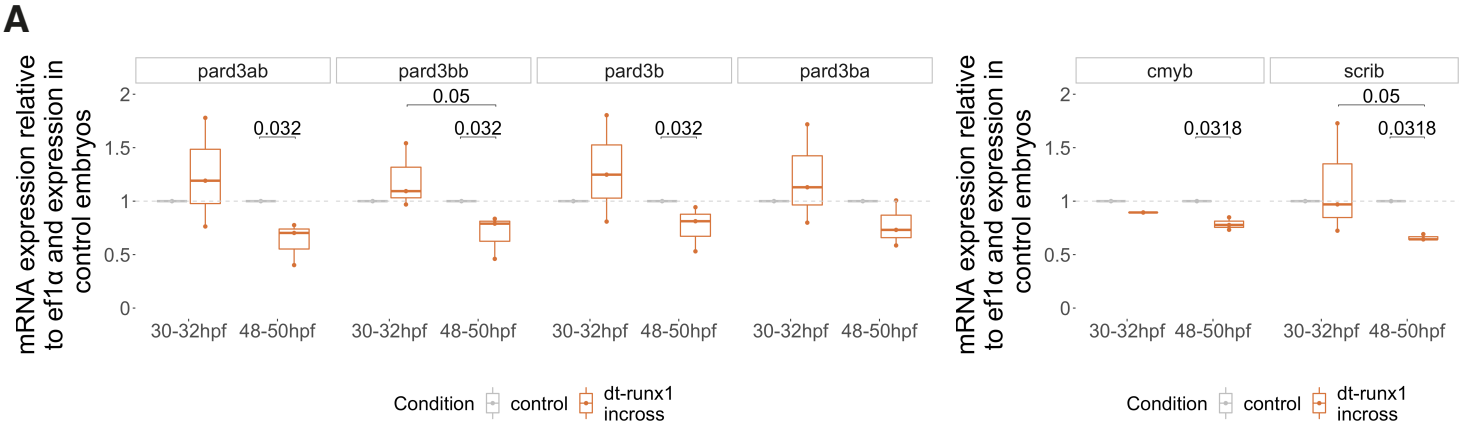

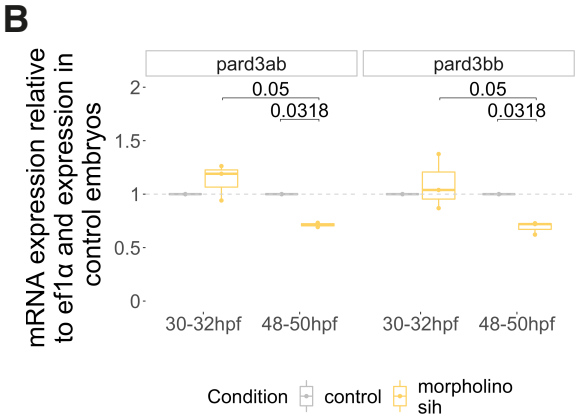

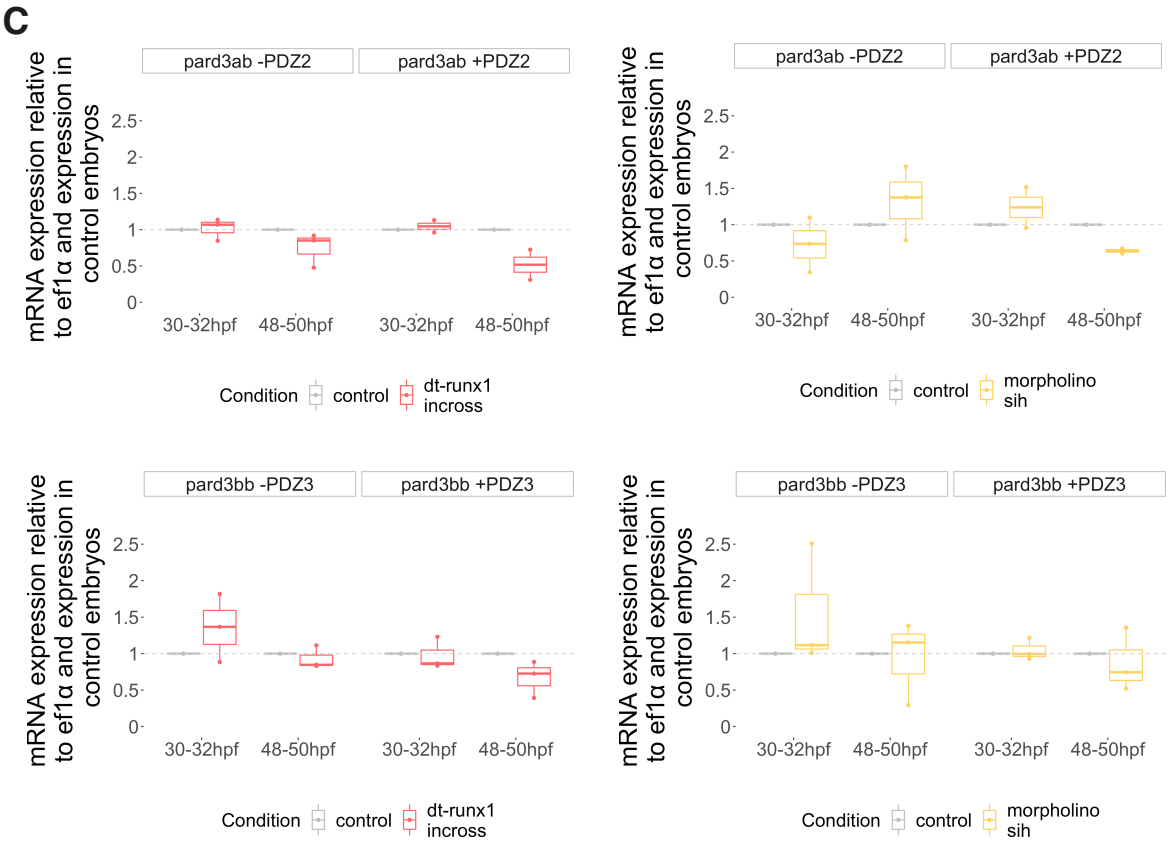

Figure 5

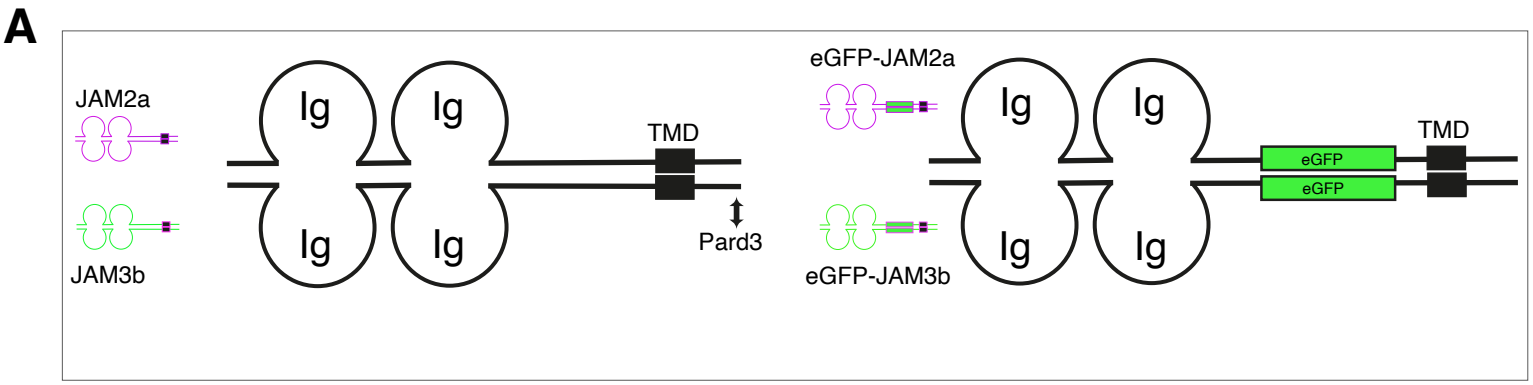

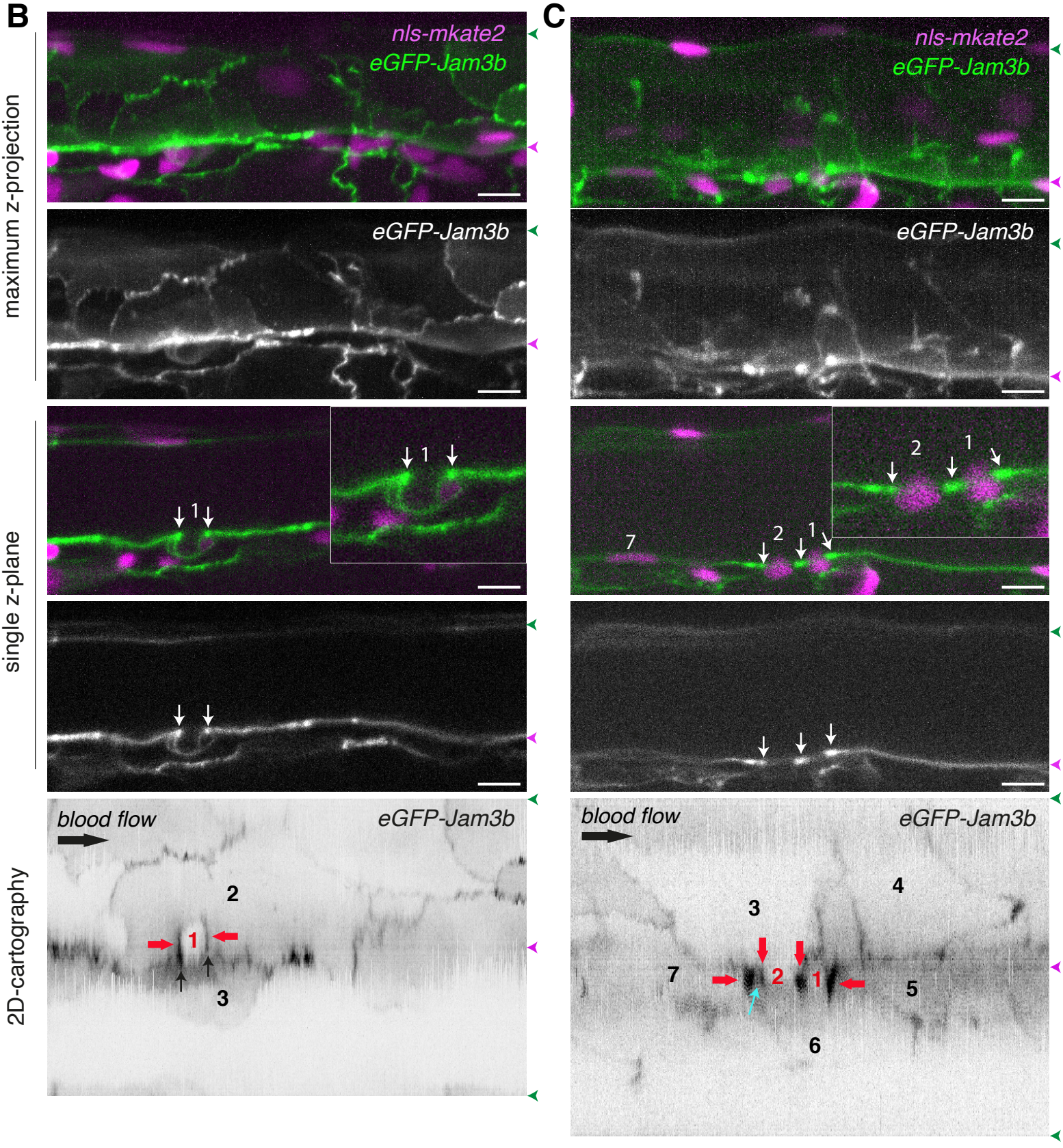

Figure 5 - figure supplement 1

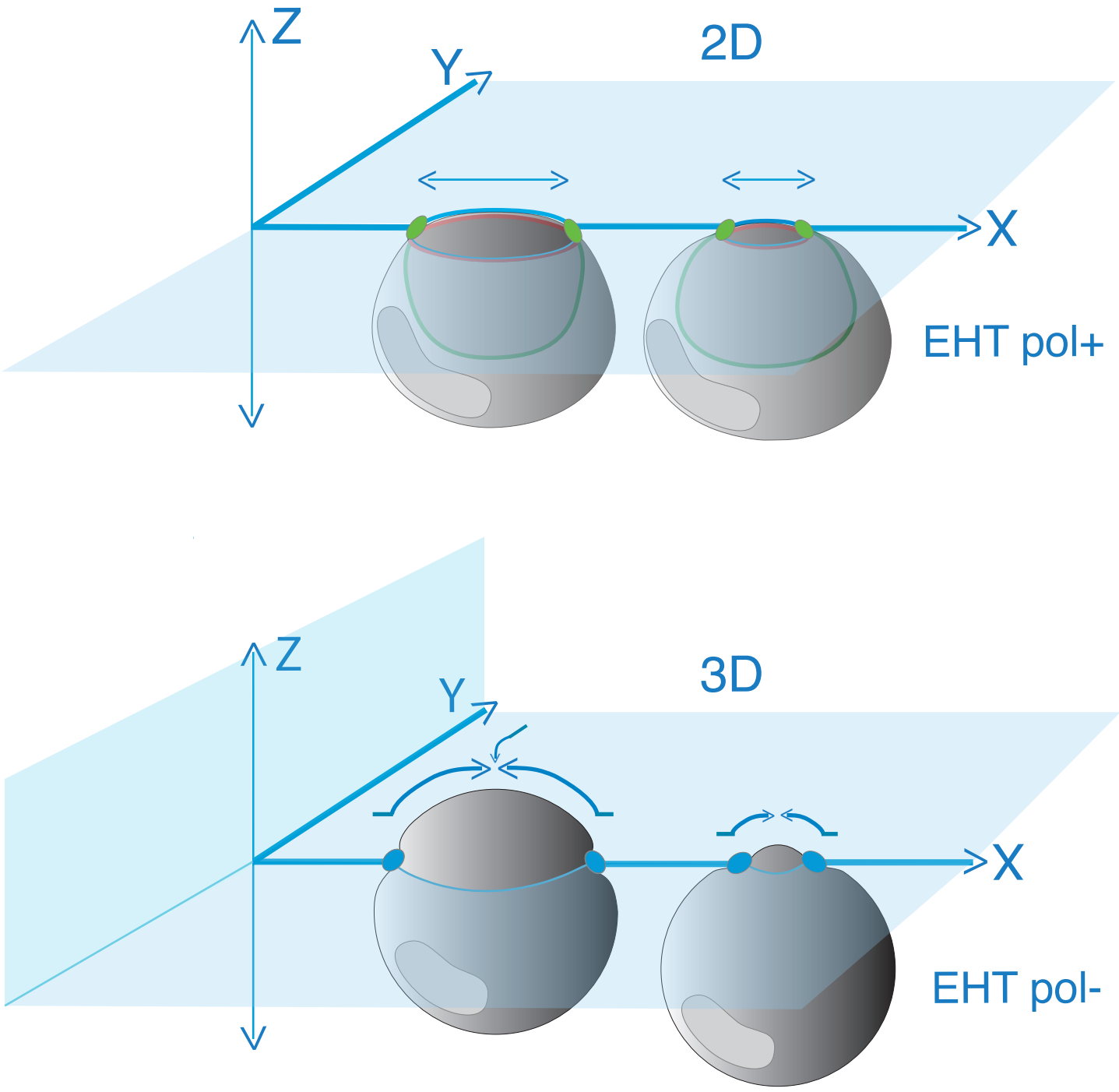

Figure 5 - figure supplement 2

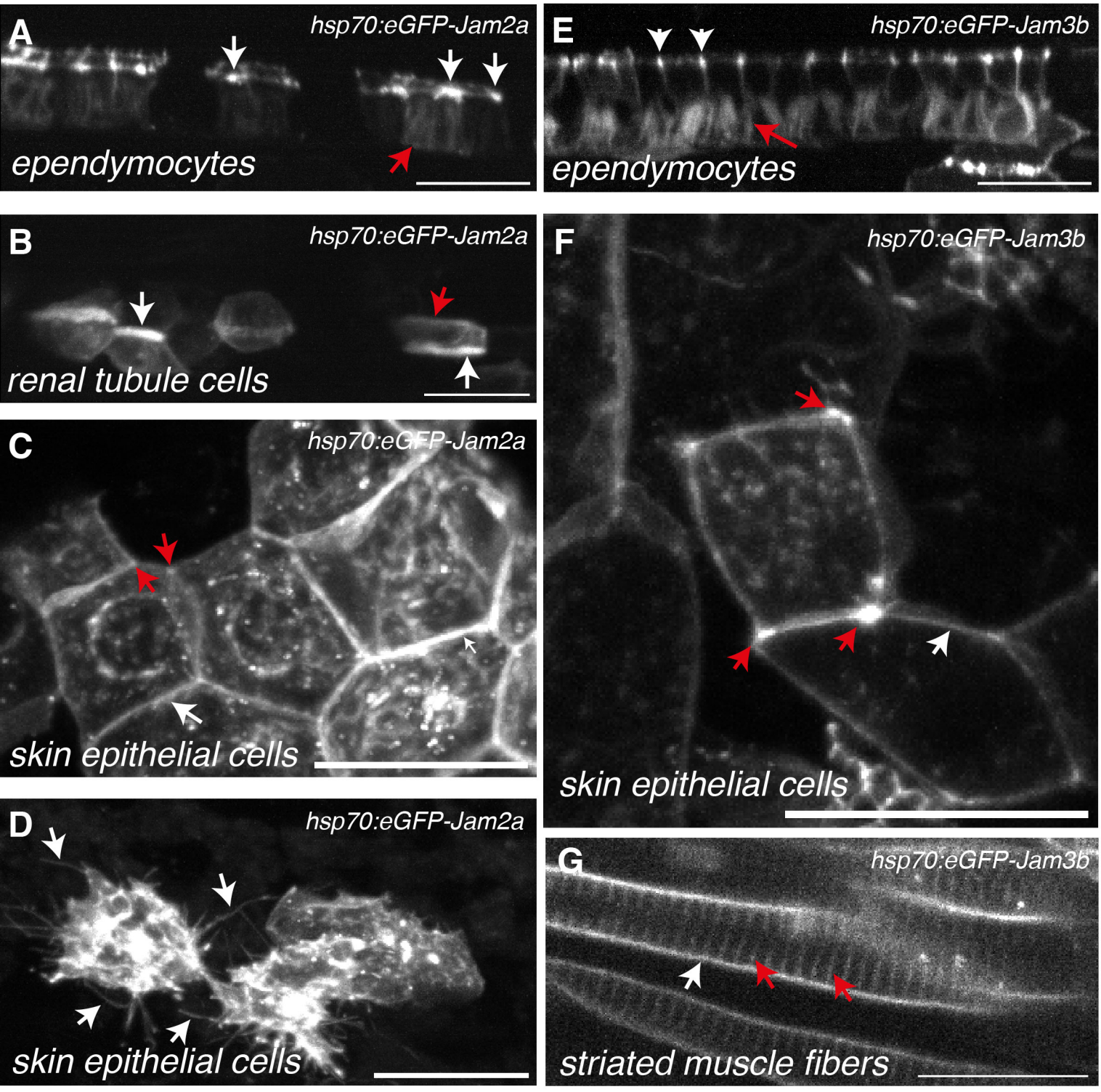

Figure 6

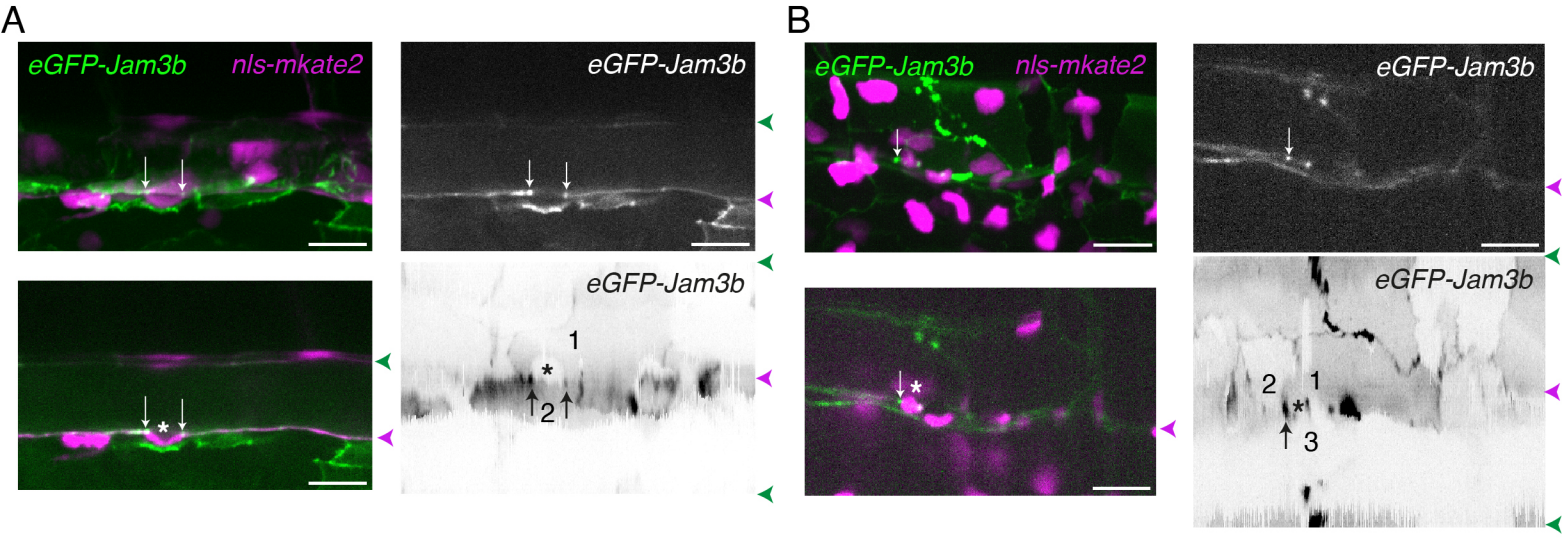
A
eGFP-Jam3b
nls-mkate2
eGFP-Jam3b
eGFP-Jam3b
1
2
B
eGFP-Jam3b
nls-mkate2
eGFP-Jam3b
eGFP-Jam3b
2
1
3

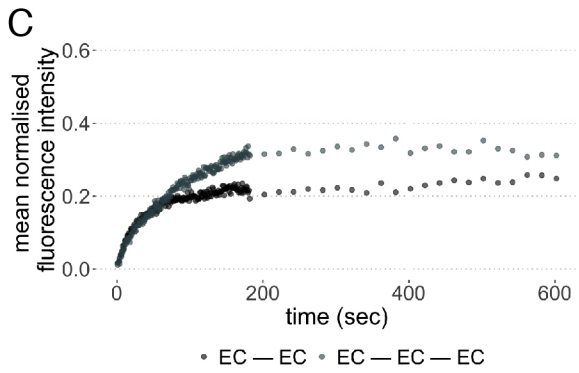
C
mean normalised fluorescence intensity
0.0
0.2
0.4
0.6
0
200
400
600
time (sec)
EC — EC
EC — EC — EC

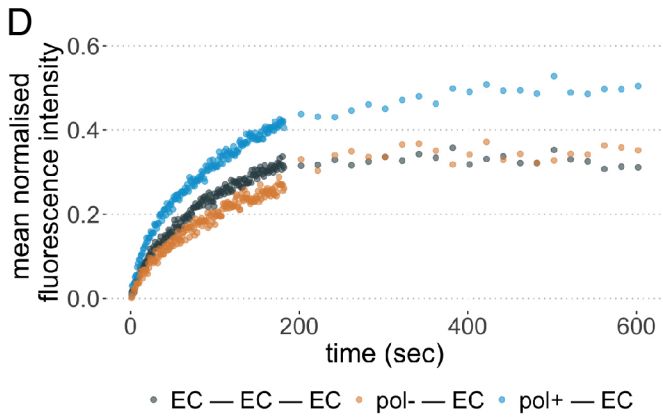
D
mean normalised fluorescence intensity
0.0
0.2
0.4
0.6
0
200
400
600
time (sec)
EC — EC — EC
pol- — EC
pol+ — EC

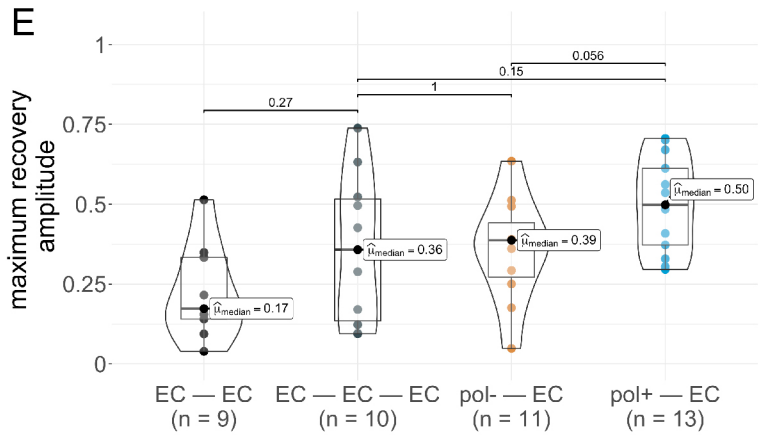
E
maximum recovery amplitude
0
0.25
0.5
0.75
1
0.27
1
0.15
0.056
$\hat{\mu}_{median}$ = 0.17
$\hat{\mu}_{median}$ = 0.36
$\hat{\mu}_{median}$ = 0.39
$\hat{\mu}_{median}$ = 0.50
EC — EC
(n = 9)
EC — EC — EC
(n = 10)
pol- — EC
(n = 11)
pol+ — EC
(n = 13)

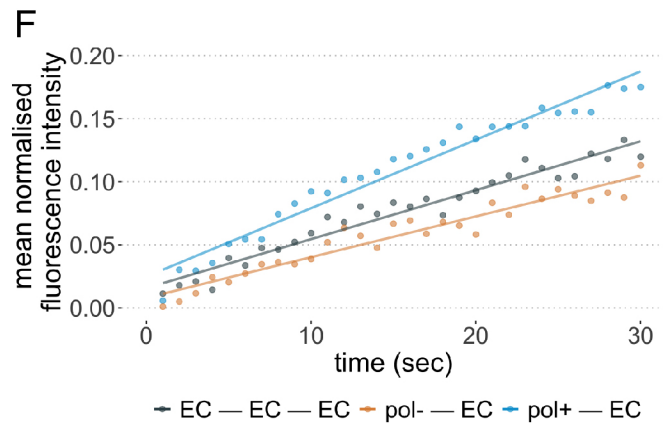
F
mean normalised fluorescence intensity
0.00
0.05
0.10
0.15
0.20
0
10
20
30
time (sec)
EC — EC — EC
pol- — EC
pol+ — EC

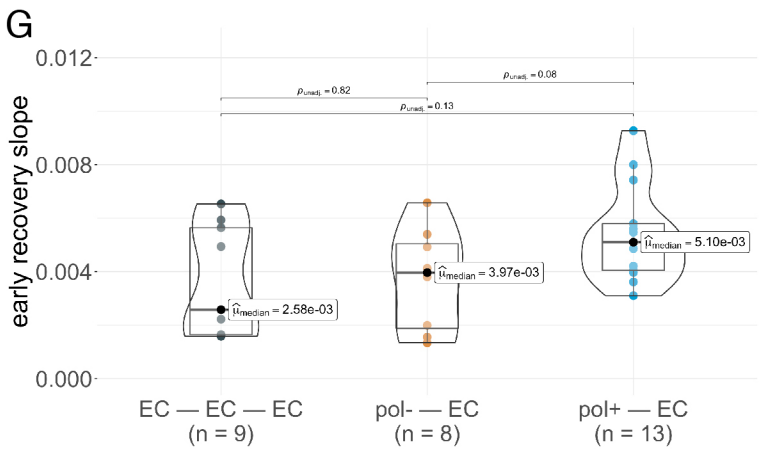
G
early recovery slope
0.000
0.004
0.008
0.012
$p_{unadj.}$ = 0.82
$p_{unadj.}$ = 0.13
$p_{unadj.}$ = 0.08
$\hat{\mu}_{median}$ = 2.58e-03
$\hat{\mu}_{median}$ = 3.97e-03
$\hat{\mu}_{median}$ = 5.10e-03
EC — EC — EC
(n = 9)
pol- — EC
(n = 8)
pol+ — EC
(n = 13)

Figure 6 - figure supplement 1

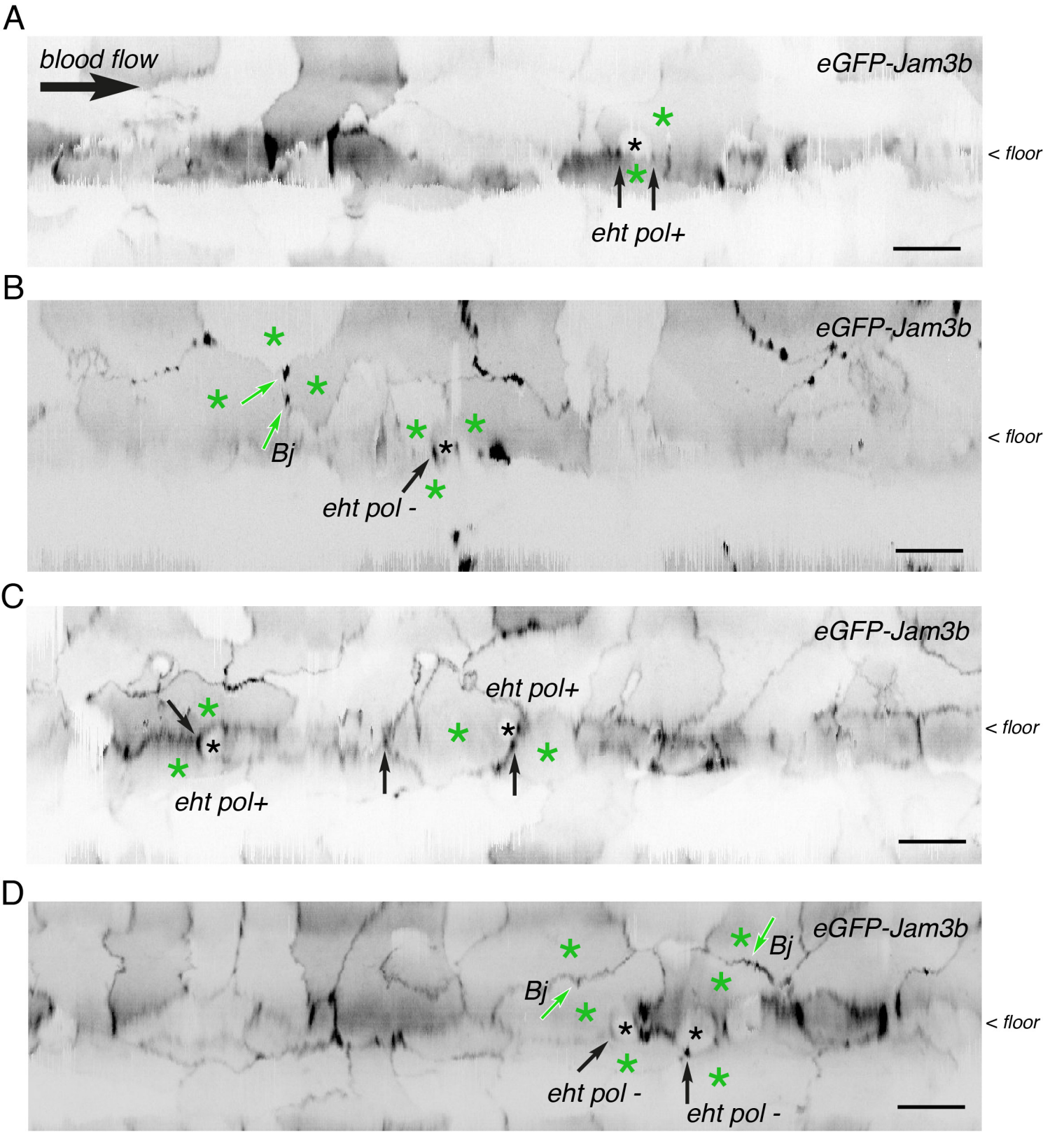

Figure 7

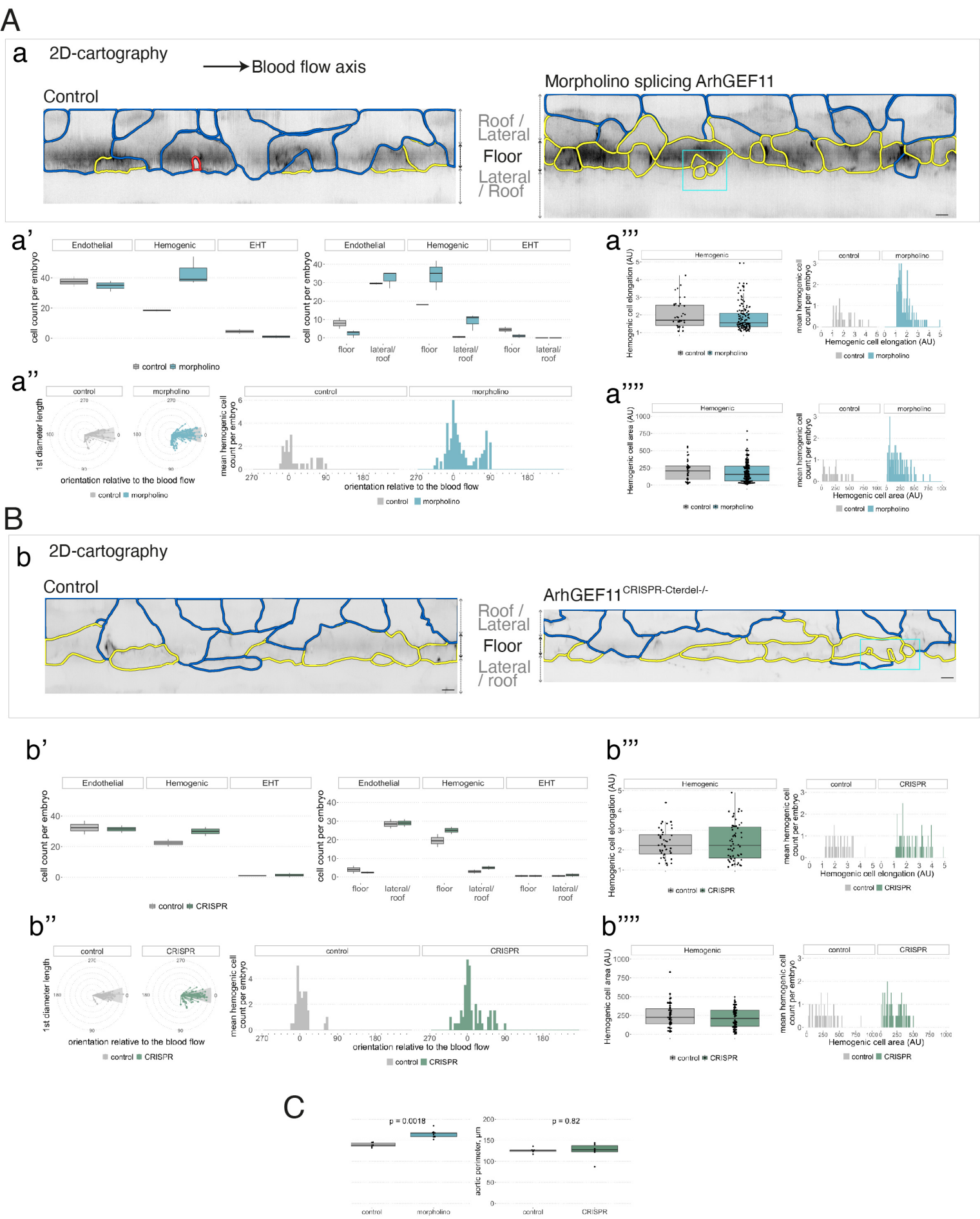
A
a
2D-cartography
Blood flow axis
Control
Morpholino splicing ArhGEF11
Roof / Lateral
Floor
Lateral / Roof
a'
Endothelial
Hemogenic
EHT
cell count per embryo
floor
lateral/ roof
control
morpholino
a''
1st diameter length
orientation relative to the blood flow
mean hemogenic cell count per embryo
a'''
Hemogenic cell elongation (AU)
Hemogenic cell elongation (AU)
a''''
Hemogenic cell area (AU)
Hemogenic cell area (AU)
B
b
2D-cartography
Control
ArhGEF11CRISPR-Cterdel-/-
Roof / Lateral
Floor
Lateral / roof
b'
CRISPR
b''
b'''
b''''
C
p = 0.0018
p = 0.82
aortic perimeter, µm

Figure 7 - figure supplement 1

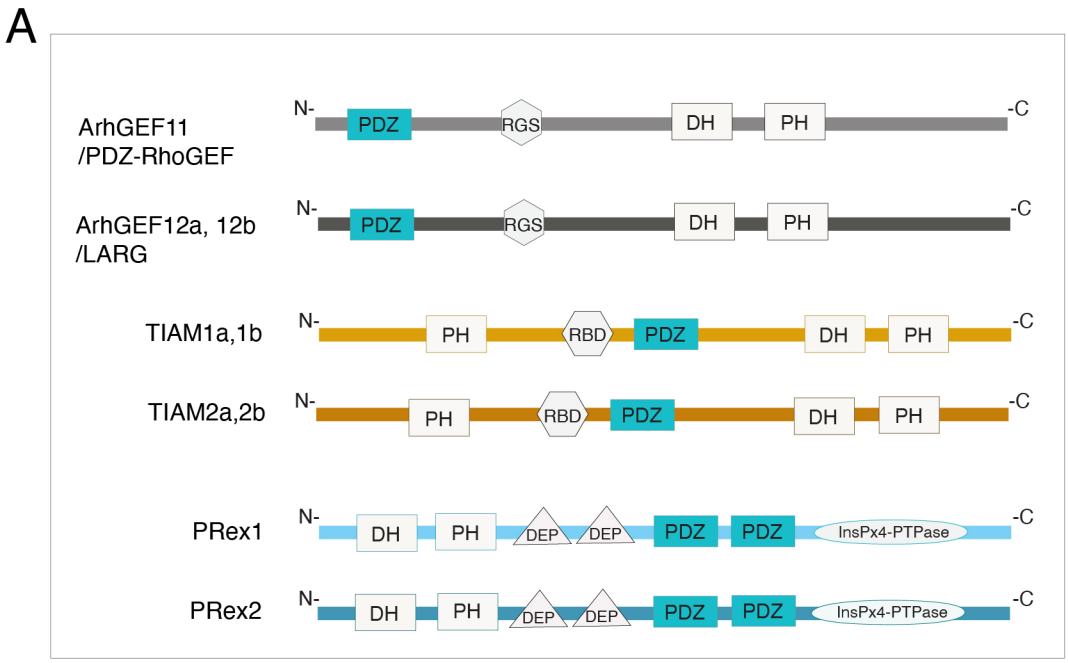

B

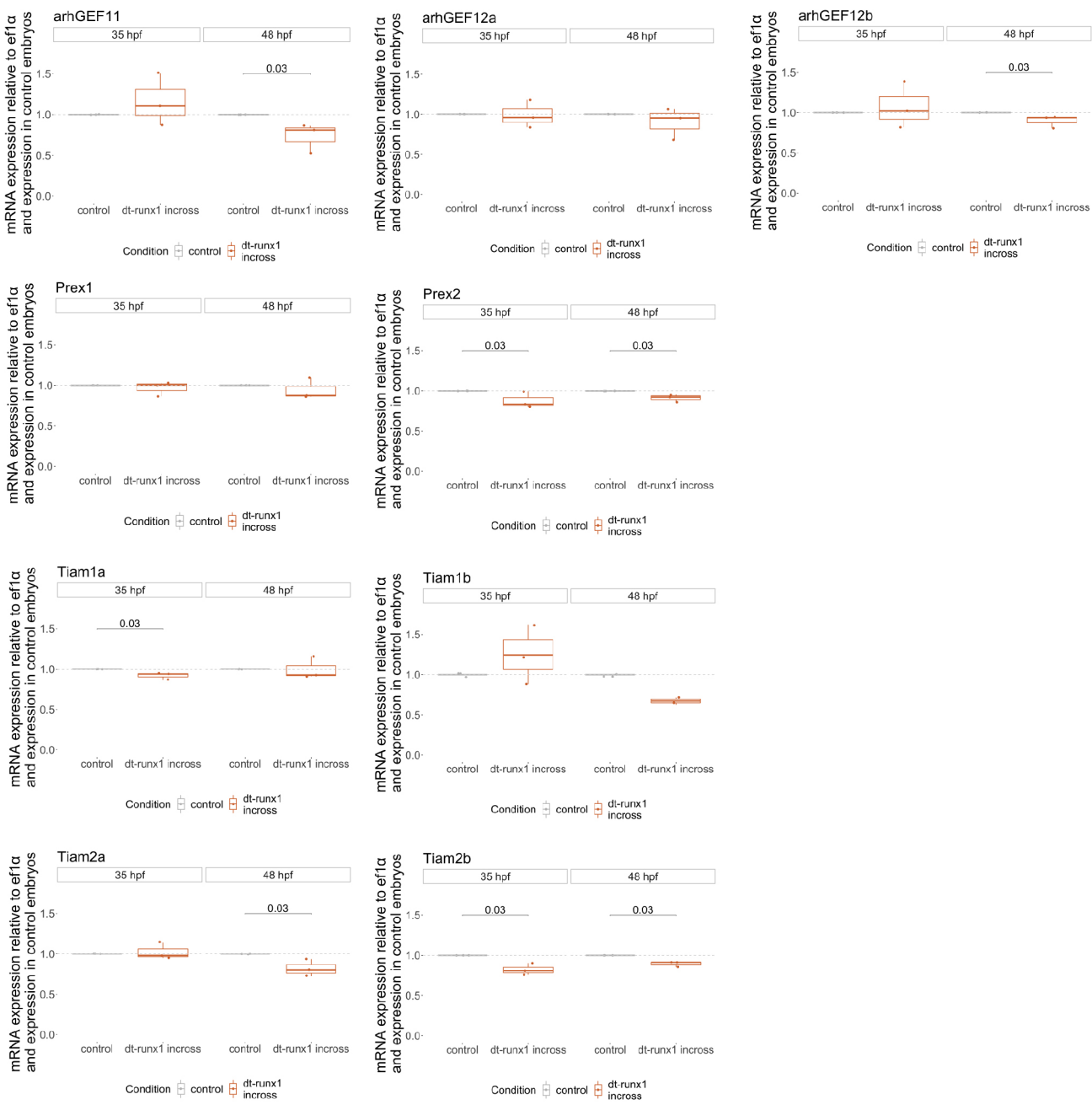

Figure 7 - figure supplement 2

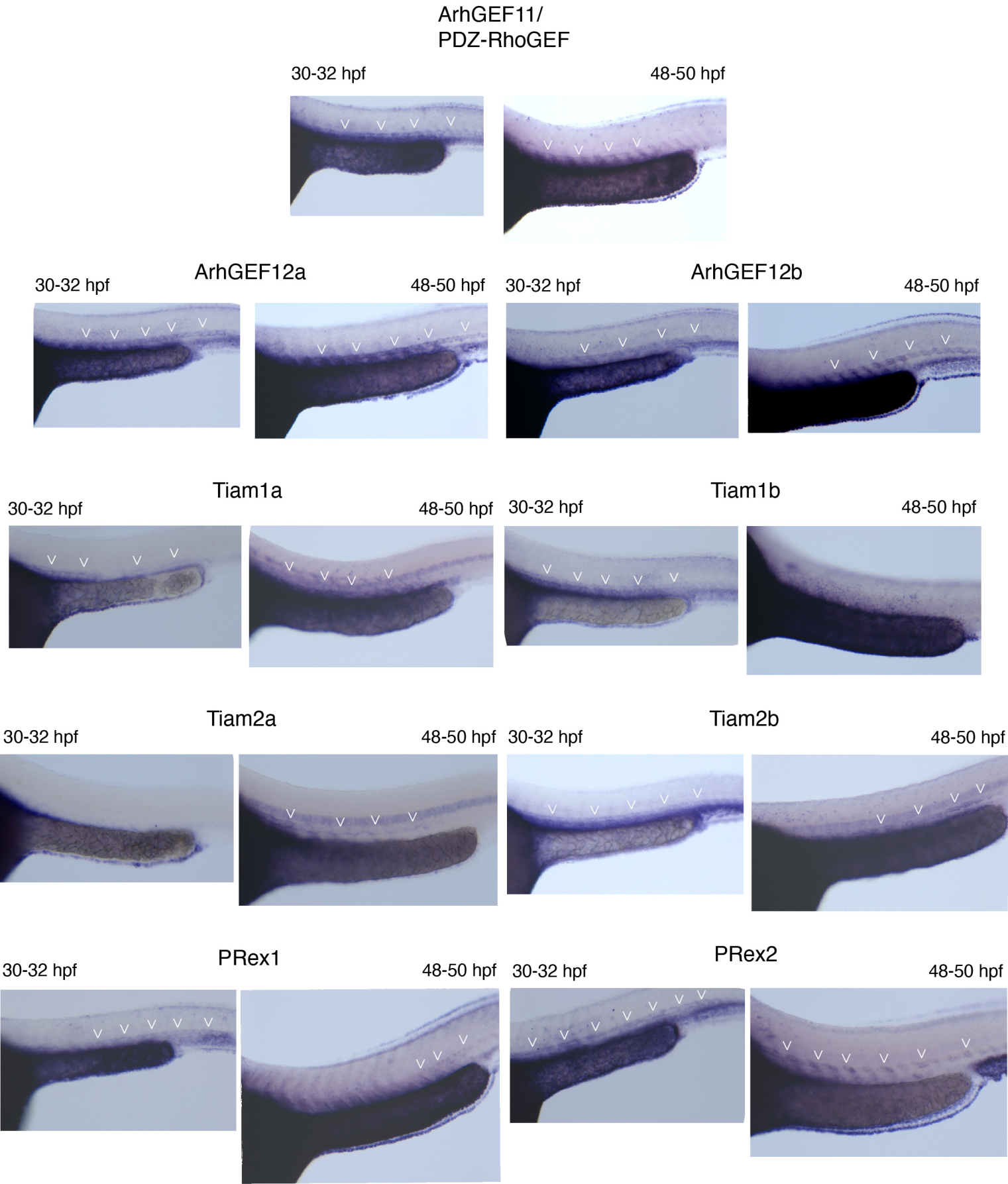

Figure 7 - figure supplement 3

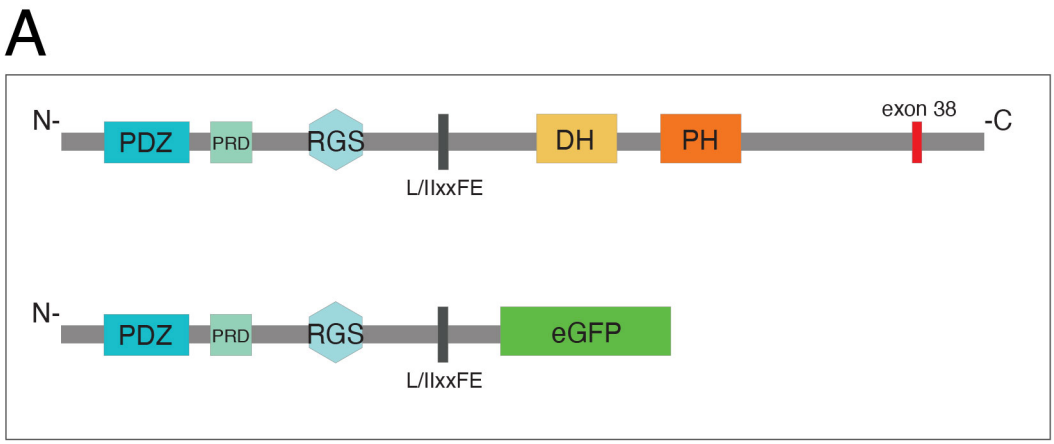

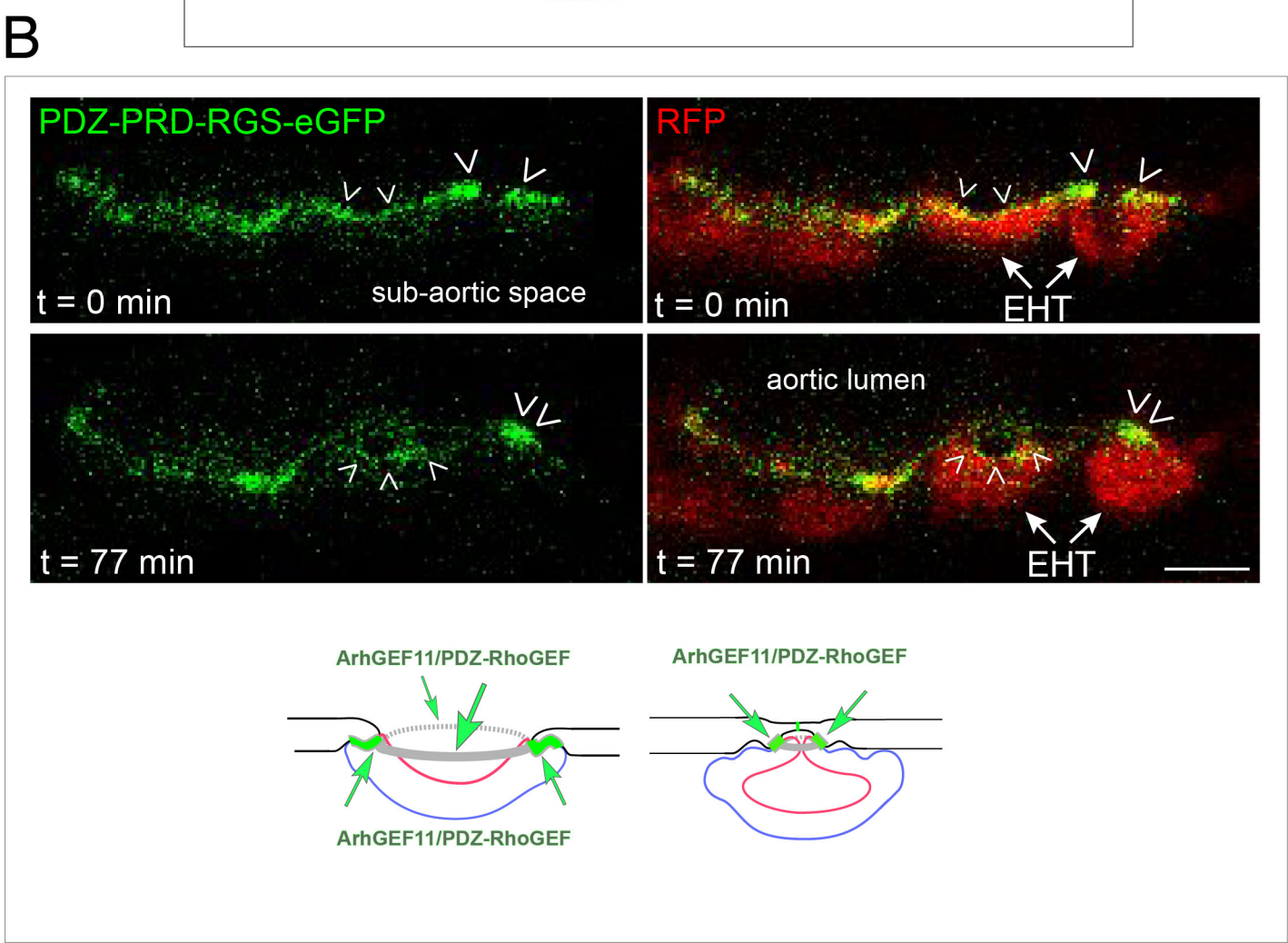

Figure 7–figure supplement 4

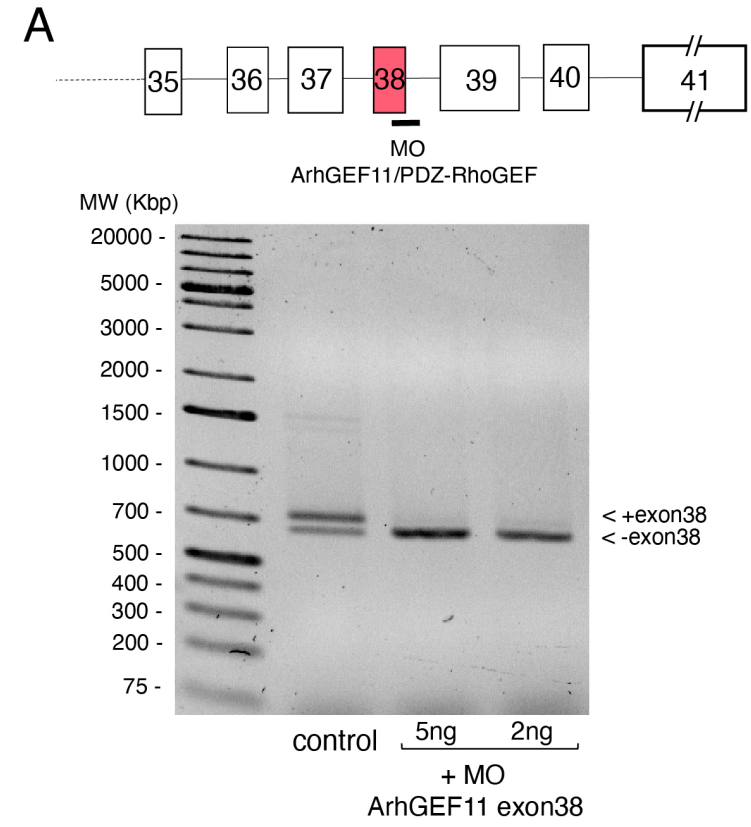

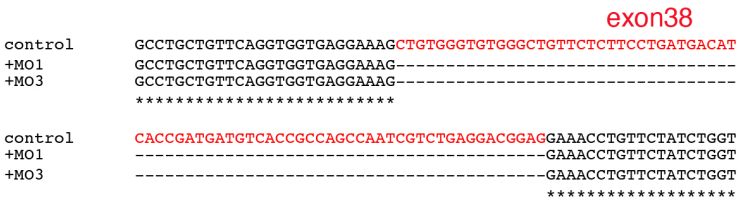

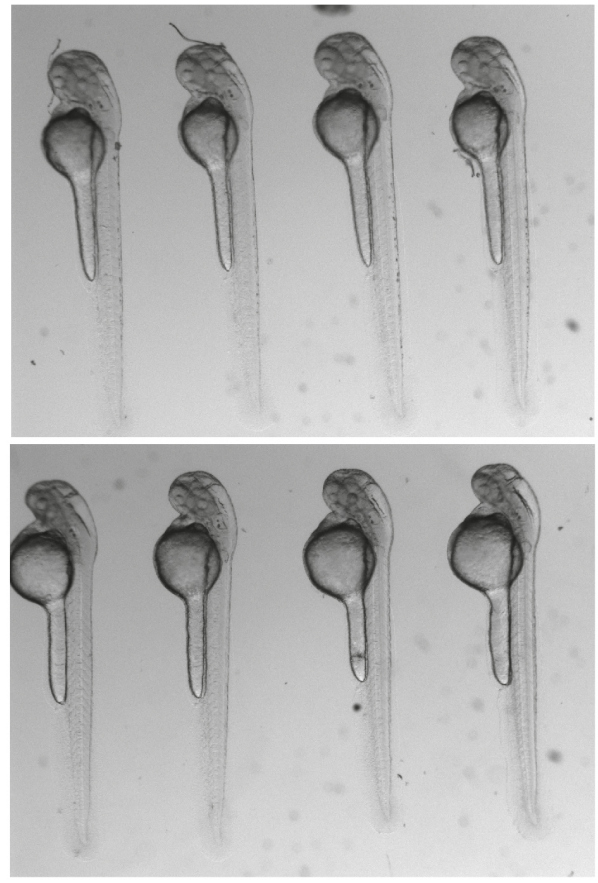

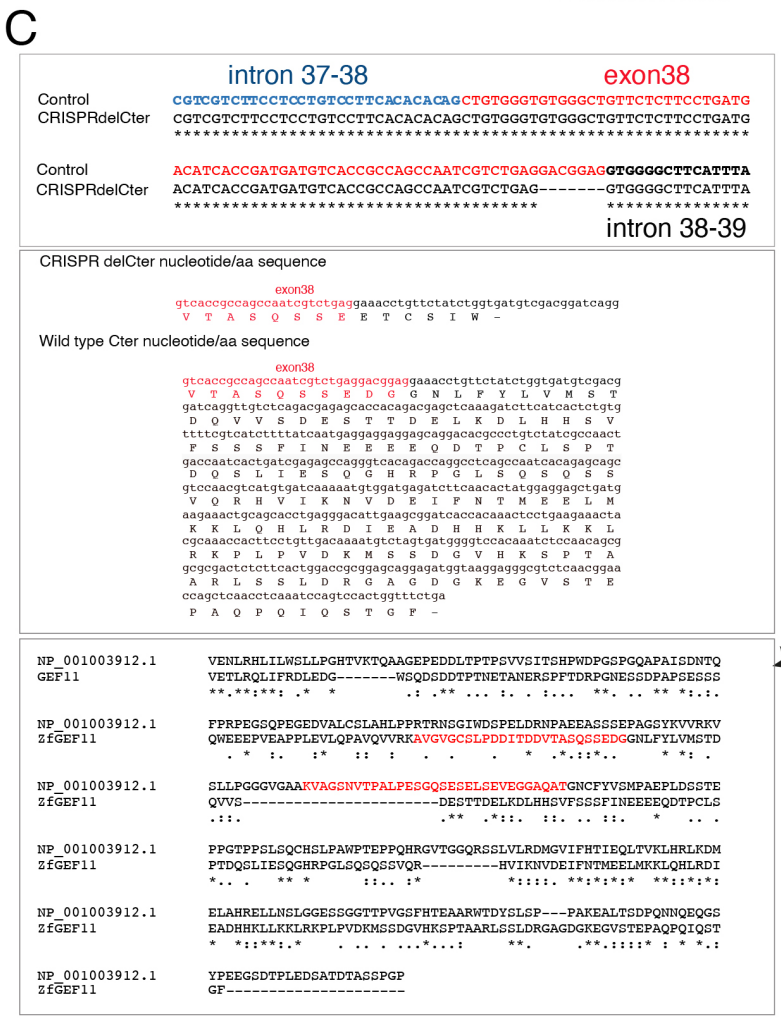

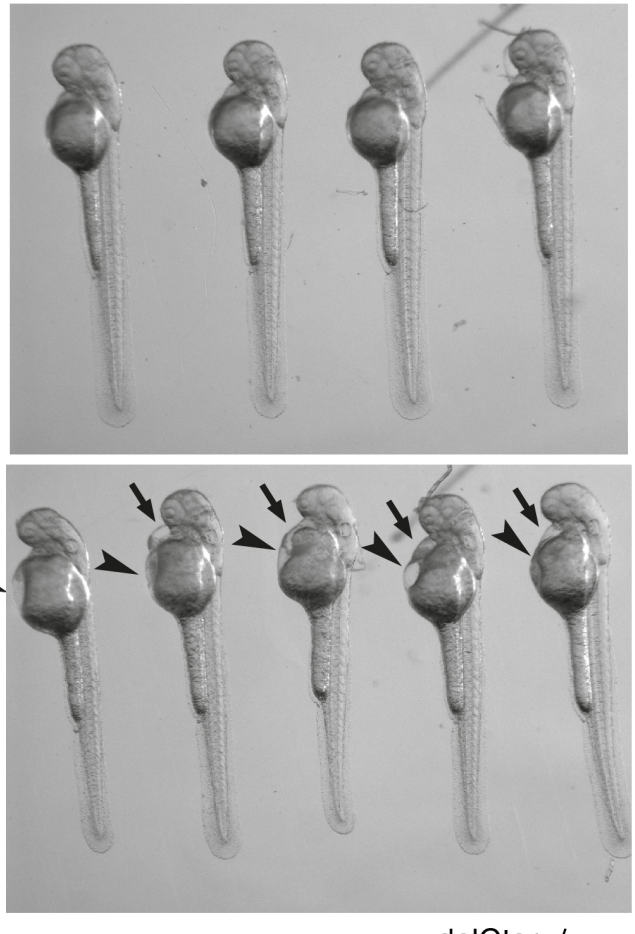

Figure 7 - supplemental 5

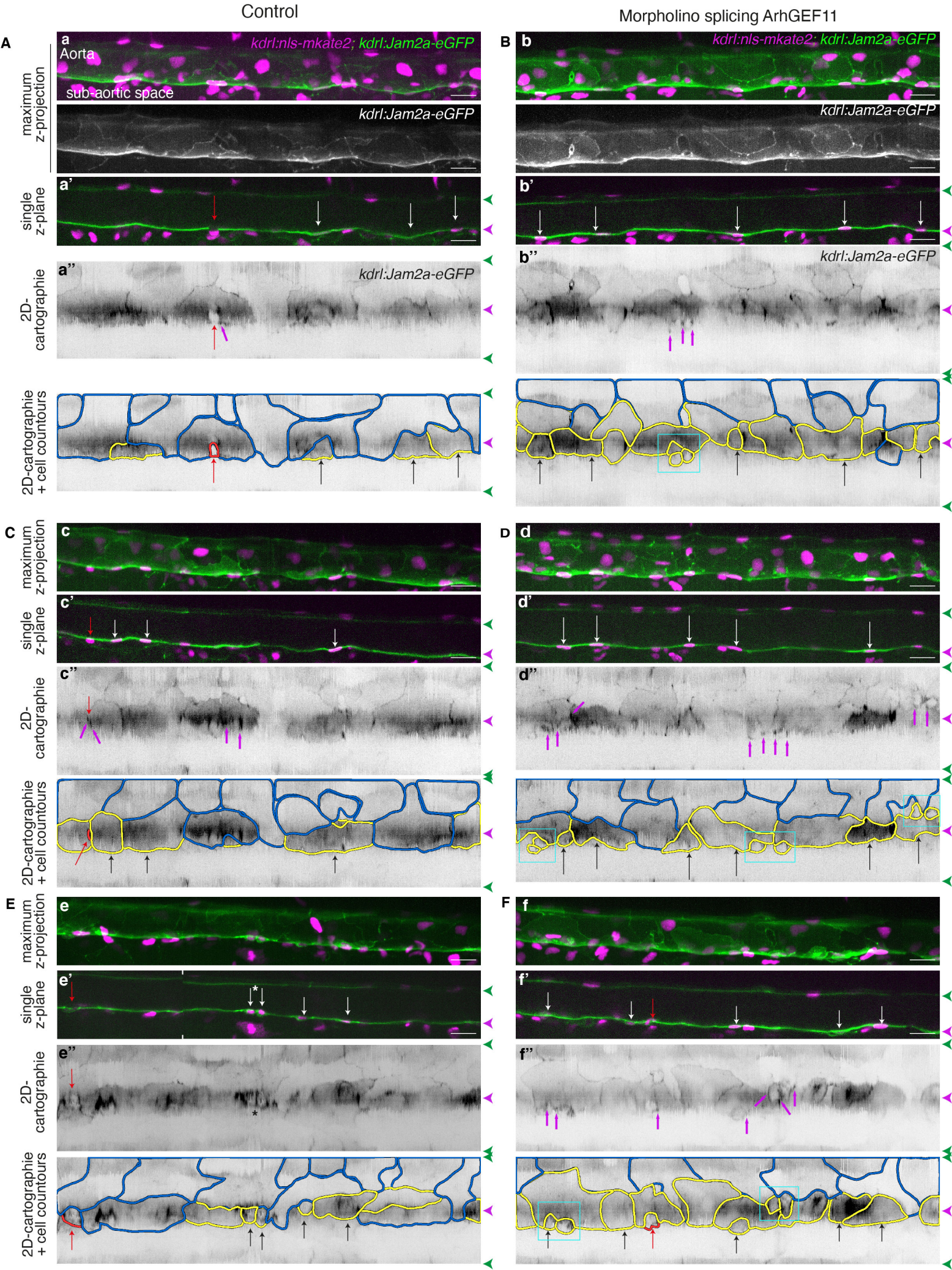

Figure 7 - supplement 6

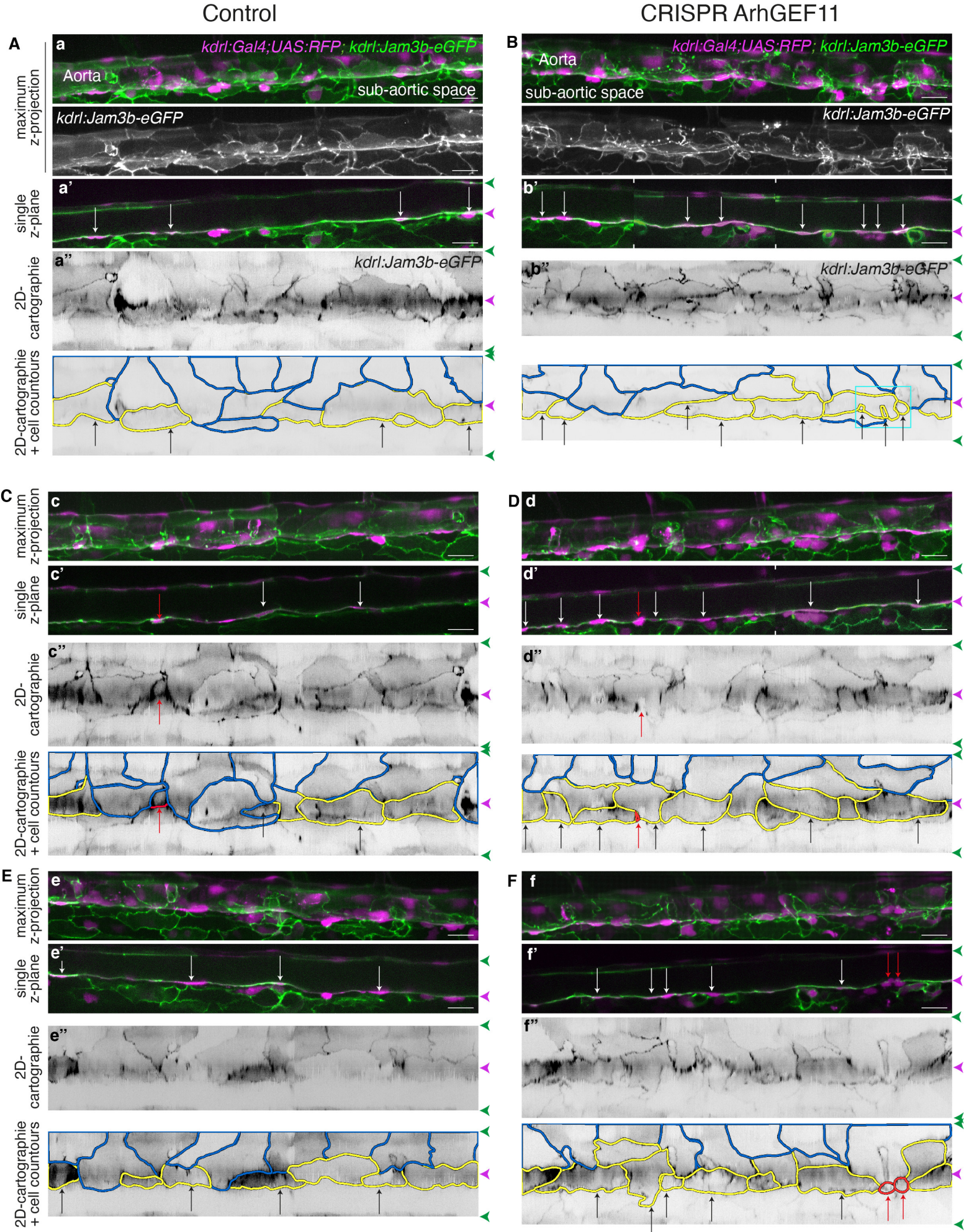

Figure 8